Felix Kramer

STUDY AND OPTIMIZATION OF THE TRANSVERSE BEAM PARAMETERS BEFORE INJECTION INTO THE STORAGE RING BESSY II

Master's Thesis

Humboldt University of Berlin

August, 2016

Humboldt Universität zu Berlin

Faculty of Mathematics and Natural Sciences

Department of Physics,
International Master of Science in Physics
on Accelerator Physics

STUDY AND OPTIMIZATION OF THE TRANSVERSE BEAM PARAMETERS BEFORE INJECTION INTO THE STORAGE RING BESSY II

Thesis by
Felix Armborst, formerly Kramer

Supervisors

Prof. Dr. Andreas Jankowiak . . . .

Dr. Peter Kuske . . . .

Candidate

B. Sc. Felix Armborst, formerly Kramer . . . .

Graduation Session, Wednesday, 31st of August, 2016
Academic Year 2015/2016

Abstract

At BESSY II a linear accelerator delivers electrons with 50 MeV to a synchrotron where they are boosted to 1.7 GeV in 33 ms and then injected into the storage ring. The injection into the ring is a critical step of the acceleration cycle and of great importance for implementing the top up mode. Lost electrons from a mismatched injection produce Bremsstrahlung and radionuclides. The former lead to short-term and the latter to long-term increased radiation doses which must be avoided. Therefore, it is important to optimize the beam parameters for a close to lossless injection.

For top up injection into the storage ring BESSY II, an average injection efficiency of 90% is required. Future BESSY II features will include shorter bunches in the storage ring (VSR) and a user transparent injection with a non linear kicker. These will raise the demands on the quality of the injected beam even further.

The beam is injected into the storage ring in the radial plane and off-axis. Thus larger radial beam emittance requires a bigger radial acceptance of the ring. The injected beam is provided by a synchrotron, from which the beam is extracted just before reaching equilibrium emittance. Adiabatic and radiation damping due to steady increase of longitudinal momentum in the cavity and random loss of momenta by synchrotron radiation decrease the emittance during particle acceleration. The quantum excitation increases the emittance by synchrotron radiation in dispersive sections and hence, usually takes place in the radial plane. Without transverse coupling this leads to a beam with relatively large radial and small axial emittance from the synchrotron. In case of sufficient axial acceptance in the ring, one can take advantage of the small axial emittance by transverse emittance exchange before injection.

Subject of this thesis is to study the development of the transverse electron beam emittance from the linear accelerator over the acceleration in the booster-synchrotron up to the injection into the storage ring. Furthermore, different possibilities of altering this development are evaluated. Especially emittance exchange processes between the small axial and large radial emittance are studied. This is possible with a set of static skew quadrupole magnets in the transfer line or with dynamic skew magnets in the booster that induce an emittance exchange just before extraction. Results of emittance measurements and an estimation of a possible exchange section in the transfer line are given.

Zusammenfassung

Am BESSY II liefert ein Linearbeschleuniger Elektronen mit 50 MeV an ein Synchrotron, wo diese in 33 ms auf 1.7 GeV beschleunigt und dann in den Speicherring injiziert werden. Die Injektion in den Speicherring ist ein kritischer Schritt des Beschleunigungszyklus und wichtig für den Top Up Modus. Verlorene Elektronen einer nicht angepassten Injektion erzeugen Bremsstrahlung und Radionuklide. Erstere führen kurzzeitig und letztere langfristig zu erhöhten Strahlungsdosen, welche vermieden werden sollen. Daher ist es wichtig, die Strahlparameter für eine verlustfreie Injektion zu optimieren. Für Top Up Injektion in den Speicherring BESSY II wird eine durchschnittliche Injektionseffizienz von mindestens 90% benötigt. Zukünftige BESSY II Merkmale sollen kurze Bunche im Speicherring (VSR) und eine für Nutzer transparente Injektion mit einem nichtlinearen Kicker beinhalten. Diese werden der Anforderung möglichst geringer radialer Emittanz des injizierten Strahls zusätzliches Gewicht verleihen.

Der Strahl wird horizontal versetzt in der radialen Ebene in den Speichering injiziert. Daher bedingt eine größere radiale Strahlemittanz eine größere Akzeptanz des Ringes. Der injizierte Strahl wird von einem Synchrotron geliefert. Er wird kurz vor erreichen der Gleichgewichtsemittanz aus diesem extrahiert. Adiabatische und Strahlungsdämpfung bedingt durch Zufällige Impulsverluste durch Synchrotronstrahlung und stetige Erhöhung des longitudinalen Impulses in der Kavität verringern die Emittanz über den Beschleunigungszyklus. Die Quantenanregung erhöht die Emittanz durch Synchrotronstrahlung in dispersiven Sektionen und findet dementsprechend hauptsächlich in der radialen Ebene statt. Ohne transversale Kopplung erhält man so einen Strahl mit relativ großer radialer und relativ kleiner axialer Emittanz vom Synchrotron. Im Falle ausreichender axialer Akzeptanz des Rings kann man die kleine axiale Emittanz durch transversalen Emittanzaustausch vor der Injektion ausnutzen.

Thema dieser Arbeit ist die Entwicklung der transversalen Strahlemittanz vom Linearbeschleuniger über die Beschleunigungsrampe im Boostersynchrotron bis zur Injektion in den Speicherring. Weiterhin werden verschiedene Möglichkeiten untersucht, diese Entwicklung zu beeinflussen. Insbesondere Emittanzaustauschprozesse zwischen der kleinen axialen und großen radialen Emittanz werden untersucht. Dies ist möglich mit einem Satz gedrehter Quadrupole in der Transferline oder mit dynamischen, gedrehten Quadrupolen im Booster, welche einen Austausch kurz vor Extraktion induzieren. Ergebnisse von Emittanzmessungen und eine Abschätzung einer möglichen Emittanzaustauschsektion für die Transferline werden vorgestellt.

Acknowledgements

I would like to thank the following people (in alphabetical order) very much for their spent time and effort in supporting me with many informative, fruitful and always thought-provoking discussions and hereby helping me complete my master's thesis. Assistance provided by the HZB machine group when making measurements and bringing the machine back to life afterwards was greatly appreciated.

- Aleksandr Matveenko
- Andreas Schälicke
- Atoosa Meseck
- Dennis Engel
- Dieter Faulbaum
- Falk Hoffmann
- Godehard Wüstefeld
- Jens Völker

- Markus Ries
- Martin Ruprecht
- Michael Abo-Bakr
- Paul Volz
- Paul Goslawski
- Rainer Görgen
- Terry Atkinson
- Thomas Birke

Special thanks go to my supervisors

- Andreas Jankowiak
- Peter Kuske

Last but not least I would like to acknowledge the support provided by my family during the preparation of my thesis.

Declaration

I hereby confirm that I have authored this master's thesis independently and without use of others than the indicated sources. All passages which are literally or in general matter taken out of publications or other sources are marked as such.

Berlin, Wednesday, 31st of August, 2016

. . . .
B. Sc. Felix Kramer

Dedication

To Alina and my family

List of Figures

List of Tables

List of Symbols

Symbol	Description
c	Speed of light
e	Elementary charge
f_s	Synchrotron frequency
g	Pole shoe gap
g_{ij}	Metric tensor
h	Harmonic number
$h_{\hat{\mu}_i}$	Scale factor
k	Quadrupole strength
k_{skew}	Skew quadrupole strength
q	Particle charge
$q_{x,y,s}$	Radial (x), axial (y) and longitudinal (s) quantum excitation
s	longitudinal coordinate along orbit
t	Time
$\vec{v}$	Velocity
x	Radial displacement
x'	Radial, angular deviation (dx/ds)
y	Axial displacement
y'	Axial, angular deviation (dy/ds)
l	Longitudinal displacement
$\vec{B}$	Magnetic flux density, binormal unit vector
$D_{x,y}$	Radial (x) and axial (y) dispersion functions
E	Particle energy
E_0	Particle rest energy (m_0c^2)
E_c	Critical energy of synchrotron radiation
$\vec{E}$	Electric field
$\vec{F}_{Lorentz}$	Lorentz force
$\mathcal{H}$	Curly H function
$\mathcal{I}$	Synchrotron integral
$J_{x,y,s}$	Radial (x), axial (y) and longitudinal (s) damping partition numbers
L	Circumference of the orbit
$\dot{N}_\gamma$	Number of emitted photons per time
P_γ	Radiated synchrotron radiation power
$Q_{x,y,s}$	Radial (x), axial (y) and longitudinal (s) tunes
R	Bending radius ($C/(2\pi)$)
T_{rev}	Revolution time
U	Energy loss per turn
α	Fine structure constant ($\sim 1/137$)

List of Symbols

α_p	Momentum compaction factor
$\alpha_{x,y,s}$	Radial (x), axial (y) and longitudinal (s) damping coefficients
β	Ratio of velocity to the speed of light c (v/c)
$\beta_{x,y}, \alpha_{x,y}, \gamma_{x,y}$	Radial (x) and axial (y) Twiss functions
γ	Relativistic Lorentz factor ($1/\sqrt{1-\beta^2}$)
γ_t	Transition energy ($1/\sqrt{\alpha_p}$)
δ	Single particle energy spread
$\delta_{i,j}$	Kronecker delta
$\epsilon_{x,y,s}$	Radial (x), axial (y) and longitudinal (s) emittances
$\epsilon_{x,y,s}^*$	Normalised radial (x), axial (y) and longitudinal (s) emittances ($\beta\gamma\epsilon_{x,y,s}$)
η	Phase slip factor
κ	Coupling coefficient
λ_c	Critical wavelength of synchrotron radiation
$\hat{\mu}_i$	Normalized unit vector
$\xi_{x,y}$	Radial (x) and axial (y) chromaticity
σ_δ	Ensemble energy spread
$\tau_{x,y,s}$	Radial (x), axial (y) and longitudinal (s) damping times
Σ	Beam matrix
Ψ	Betatron phase

List of Abbreviations

ACCPY	**ACC**elerator **PY**thon - Python module providing simulation and measurement tools for accelerator physics and a GUI for easy accessibility
BESSY	**B**erlin **E**lectron **S**torage Ring **S**ociety for **SY**nchrotron Radiation
BPM	**B**eam **Position** **M**onitor
CCD	**C**harge-**C**oupled **D**evice
CMOS	**C**omplementary **M**etal-**O**xide-**S**emiconductor
DBA	**D**ouble **B**end **A**chromat
DLSR	**D**iffraction-**L**imited **S**torage **R**ing
EOM	**E**quations **O**f **M**otion
ELEGANT	**ELE**ctron **G**eneration **AN**d **T**racking
EPICS	**E**xperimental **P**hysics and **I**ndustrial **C**ontrol **S**ystem
FFT	**F**ast **F**ourier **T**ransformation
GUI	**G**raphical **U**ser **I**nterface
HOM	**H**igher **O**rder **M**ode
HZB	**H**elmholtz-**Z**entrum **B**erlin für Materialien und Energie GmbH
IPCE	**I**ncident **P**hoton to **C**onverted **E**lectron
LINAC	**LIN**ear **AC**celerator
LPM	**L**ong **P**ulse **M**ode
MAD	**M**ethodical **A**ccelerator **D**esign
MBA	**M**ulti **B**end **A**chromat
ROI	**R**egion **O**f **I**nterest
SPM	**S**hort **P**ulse **M**ode
TNB	**T**angent, **N**ormal and **B**inormal vectors
VSR	**V**ariable pulse length **S**torage **R**ing

Contents

Contents

1. Introduction

Particle accelerators have become sophisticated research tools of our time for exploring the micro cosmos that determines the physics of the macro cosmos mankind lives in and thrives to understand. They represent good opportunities of finding answers to still open questions despite the efforts of many generations of great scientists who have brought to light many physical laws that still only determine the macro cosmos to a certain extent. Whether considering colliders - which enlighten the understanding of the subatomic world or light sources like BESSY II, that can be used to examine the atomic structure of crystals or the dynamics of functional materials - potentially identifying the cornerstone of next generation solar cells, energy storage devices, information technology or proteins capable of healing an up to today incurable disease.

In Berlin-Adlershof, the Helmholtz-Zentrum Berlin für Materialien und Energie GmbH (HZB) operates the synchrotron light source BESSY II, Germany's top third generation synchrotron radiation source today. Since the commissioning in 1998, many upgrades have been successfully installed and many are still to come. The introduction of top up mode in fall 2012 has made the efficiency of the injection process into the storage ring a critical parameter due to radiation protection reglementations. It has to stay over $90\,\%$ in average of the last 4 hours and may not fall below $60\,\%$ in a single shot. The target is to limit the number of lost electrons in sum and in one shot to avoid high long- and short-term dose rates. Up to now, this has been a challenging problem that has been kept under control by optimizing parameters of injection and extraction devices, the synchrotron ramp, the transfer line optics and the storage ring. The optics of the synchrotron itself was optimized in April 2007 to minimize the emittance. This was achieved by increasing the quadrupole strengths - a path that is quickly limited by the dynamic aperture: Raising the quadrupole strengths increases the natural chromaticity making higher sextupole strengths necessary in order to compensate the chromaticity to small values. The small dynamic aperture as a result of the higher sextupole strengths strongly limits this strategy that has already been maxed out for the momentary quadrupole configuration in April 2007.

The storage ring has a rms bunch length in standard mode of $15\,\mathrm{ps}$ and $3\,\mathrm{ps}$ in low alpha mode. It has proved to be especially difficult to achieve the desired injection efficiencies with short bunches in the storage ring. Hence, the low alpha mode does not yet meet the requirements for top up mode. BESSY-VSR is the next major BESSY II upgrade enabling simultaneous variable bunch lengths in the storage ring by using two superconducting cavities with different frequencies and using the resulting beat wave for acceleration. This means, there will be simultaneous availability of short $(1.7\,\mathrm{ps})$ and long $(15\,\mathrm{ps})$ bunches in the storage ring and the BESSY-VSR low alpha mode will provide even shorter short $(0.3\,\mathrm{ps})$ and shorter long $(3\,\mathrm{ps})$ bunches.

In this work, the development of the transverse emittance during the acceleration process in the synchrotron before injection into the storage ring and possible ways of altering this development to achieve a smaller radial emittance at injection time are studied. Quadrupole scans are utilized to

measure the transverse emittance and beam parameters before (injection line) and after (transfer line) the synchrotron and the parasitic method of dipole synchrotron radiation imaging in the synchrotron is used to measure the transverse emittance over the ramp. Python code with a user-friendly graphical user interface (GUI) is developed under the name **ACC**elerator **PY**thon (ACCPY)[1,2,3,4,5,6]. It is used to simulate the linear beam optics, the synchrotron ramp and the quadrupole scans and to measure and analyse data. The code is available for testing and contributing under the GNU GENERAL PUBLIC LICENSE Version 3 at https://github.com/kramerfelix/accpy. Results from measurements and simulations are evaluated and critically discussed. Occurring problems with the used methods and possible improvements are presented.

The aim of optimizing the beam parameters for a higher injection efficiency into the storage ring is followed by taking a look at different possibilities to reduce the radial emittance for the injection. The possibility of transverse emittance exchange in the transfer line with a set of skew quadrupoles is theoretically derived and simulation results of the proposed setup are presented.

2. Theory

This chapter introduces the fundamental physics and methods - required for understanding and describing particle accelerators. Formulae behind simulations available in ACCPY as well as methods and formulae behind measurements are derived and presented.

2.1. Movement of charged particles in magnetic fields

In this section the coordinate system mostly used in accelerator physics is introduced and the equations of motion (EOM) for charged particles in magnetic fields are derived and solved for the linear case - introducing the matrix method.

2.1.1. Frenet-Serret Formulas
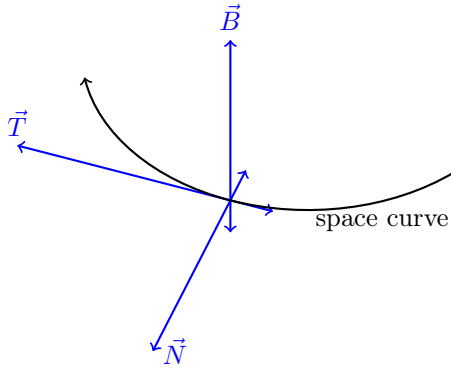
Figure 2.1.: The Vectors $\vec{T}$, $\vec{N}$ and $\vec{B}$ of the Frenet–Serret frame of reference on a space curve[7]

Every point of an arbitrary space curve s with curvature $\kappa(s)$ and torsion $\tau(s)$ is well described by the Frenet-Serret formulas. The same accounts for the arbitrary trajectory of a particle moving along a continuous, differentiable curve in three-dimensional Euclidean space. The Frenet-Serret formulas describe the derivatives of the so called tangent (Equation 2.1), normal (Equation 2.2) and binormal (Equation 2.3) unit vectors[8].

$$\vec{T}(s) = \frac{d\vec{r}(s)}{d\vec{s}} = \vec{r'}(s) \tag{2.1}$$

$$\vec{N}(s) = \frac{\vec{T'}(s)}{|\vec{T'}(s)|} = \frac{1}{|\vec{r''}(s)|}\vec{r''}(s) = R(s) \cdot \vec{r''}(s) \tag{2.2}$$

$$\vec{B}(s) = \vec{T}(s) \times \vec{N}(s) \tag{2.3}$$

Together these form an orthogonal basis - the so called TNB frame or moving trihedron that accompanies the particle along its trajectory. The curvature $\kappa(s) = \frac{1}{R(s)}$ and torsion $\tau(s) = -\vec{B'}(s)\frac{\vec{N}(s)}{|\vec{N}(s)|^2}$ or direction change of the binormal vector together completely describe the change of the moving trihedron[8]:

$$\vec{T'}(s) = |r''(s)|\vec{N}(s) = \kappa(s)\vec{N}(s) \tag{2.4}$$

$$\vec{N'}(s) = -\kappa(s)\vec{T}(s) + \tau(s)\vec{B}(s) \tag{2.5}$$

$$\vec{B'}(s) = -\tau(s)\vec{N}(s) \tag{2.6}$$

$$\begin{pmatrix} \vec{T'} \\ \vec{N'} \\ \vec{B'} \end{pmatrix} = \begin{pmatrix} 0 & \kappa & 0 \\ -\kappa & 0 & \tau \\ 0 & -\tau & 0 \end{pmatrix} \begin{pmatrix} \vec{T} \\ \vec{N} \\ \vec{B} \end{pmatrix} \tag{2.7}$$

2.1.2. Coordinates
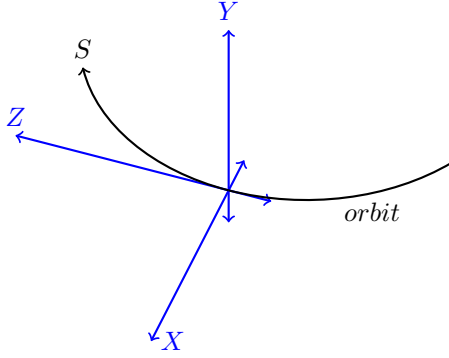
Figure 2.2.: Cartesian frame of reference moving along the orbit [7]

In accelerator physics the usual coordinate system corresponds to the torsion free Frenet-Serret formulae. The normalized, covariant unit vectors in orthogonal coordinates are given by

$$\hat{\mu}_i = \frac{1}{\left|\frac{\partial \vec{r}}{\partial q_i}\right|}\frac{\partial \vec{r}}{\partial q_i} = \frac{1}{h_i}\frac{\partial \vec{r}}{\partial q_i} \tag{2.8}$$

with the scale factors $h_i = \left|\frac{\partial \vec{r}}{\partial q_i}\right|$. They determine the metric tensor $g_{ij} = \frac{\partial \vec{r}}{\partial q_i}\frac{\partial \vec{r}}{\partial q_j} = \delta_{i,j}h_i^2$ and give the total differential change or general line element

$$d\vec{r} = \sum_i \frac{\partial \vec{r}}{\partial q_i}dq_i = \sum_i h_i\hat{\mu}_i dq_i. \tag{2.9}$$

When describing particles in accelerators it is useful switching to the moving along, Cartesian coordinate system $K(x, y, z)$ (Figure 2.2) with $g_{ij} = \delta_{i,j}$ and the line element

$$d\vec{r} = \hat{\mu}_x dx + \hat{\mu}_y dy + \hat{\mu}_z dz. \tag{2.10}$$

Its center propagates along the ideal particle trajectory $\vec{r}_0(s)$ known as the orbit - a usually planar $(\tau(s) = 0 , \vec{B}(s) = const. = \hat{\mu}_y)$ space curve. Its speed corresponds to that of the ideal particle. The momentary position of any particle can be given as an offset from the ideal particle in the x-y-plane - the normal plane to the orbit.

$$\vec{r}(s) = \vec{r}_0(s) + x(s)\hat{\mu}_x(s) + y(s)\hat{\mu}_y(s) \tag{2.11}$$

The covariant tangent unit vectors $\hat{\mu}_i(s)$ of the moving along, Cartesian coordinate system K depend on the position of K on the orbit. Therefore it is preferable to find a general formalism in analogy to the Frenet–Serret apparatus. In accelerators the torsion is usually zero and the bending radius at least piecewise constant. With these assumptions the metric of a curvilinear coordinate system $K'(x, y, s)$ corresponding to (Equation 2.11) with the line element

$$d\vec{r} = h_x\hat{\mu}_x dx + h_y\hat{\mu}_y dy + h_s\hat{\mu}_s ds \tag{2.12}$$

can be derived [9].

For deriving the special metric of the curvilinear coordinate system the propagation along the torsion free orbit is described as rotation around $\hat{\mu}_y$ so $ds = Rd\phi$ with the orbit radius R so

$$\hat{\mu}_x = \hat{\mu}_{x'}\cos(\phi) + \hat{\mu}_{s'}\sin(\phi) \tag{2.13}$$

$$\hat{\mu}_y = const \tag{2.14}$$

$$\hat{\mu}_s = \hat{\mu}_{s'}\cos(\phi) - \hat{\mu}_{x'}\sin(\phi). \tag{2.15}$$
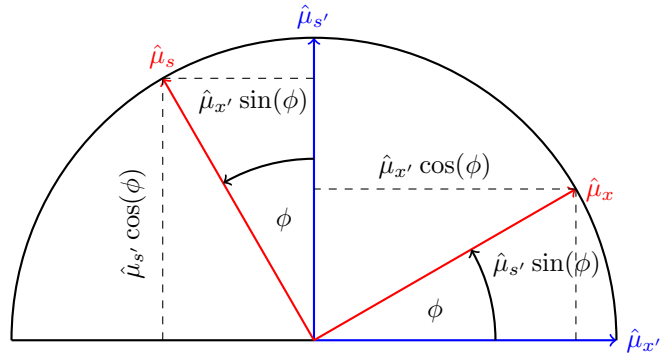
Figure 2.3.: Propagation along the orbit as rotation around $\hat{\mu}_y$ [7,10]

Revealing the dependence between the normal and tangent unit vectors:

$$\hat{\mu}_x = -\frac{\partial \hat{\mu}_s}{\partial \phi} \tag{2.16}$$

$$\hat{\mu}_s = \frac{\partial \hat{\mu}_x}{\partial \phi} \tag{2.17}$$

With these relations and some calculus:

$$\frac{d\phi}{dt} = \frac{\dot{s}}{R} \tag{2.18}$$

$$\Rightarrow \frac{d}{dt} = \frac{d\phi}{dt}\frac{d}{d\phi} = \frac{\dot{s}}{R}\frac{d}{d\phi} \tag{2.19}$$

$$\Rightarrow \frac{d}{dt} = \frac{ds}{dt}\frac{d}{ds} = \dot{s}\frac{d}{ds} \tag{2.20}$$

$$\Rightarrow \frac{d}{d\phi} = \frac{ds}{d\phi}\frac{d}{ds} = R\frac{d}{ds} \tag{2.21}$$

the derivatives of the unit vectors can be expressed as

$$\dot{\hat{\mu}}_x = \frac{\dot{s}}{R}\frac{d\hat{\mu}_x}{d\phi} = \frac{\dot{s}}{R}\hat{\mu}_s \tag{2.22}$$

$$\dot{\hat{\mu}}_y = 0 \tag{2.23}$$

$$\dot{\hat{\mu}}_s = \frac{\dot{s}}{R}\frac{d\hat{\mu}_s}{d\phi} = -\frac{\dot{s}}{R}\hat{\mu}_x \tag{2.24}$$

With the particle position vector (Equation 2.12) (the dependence on s will be left away further on) and some more calculus:

$$\frac{d}{du} = \frac{ds}{du}\frac{d}{ds} = \frac{1}{u'\dot{s}}\frac{d}{dt} = \frac{1}{u'}\frac{d}{ds} \qquad \text{with} \qquad u = x, y \tag{2.25}$$

the scale factors $h_{\hat{\mu}_i}$ can now be derived:

$$\hat{\mu}_i \cdot \hat{\mu}_j = \delta_{ij} \tag{2.26}$$

$$h_{\hat{\mu}_x} = \frac{\partial \vec{r}}{\partial x}\hat{\mu}_x = \left(\frac{1}{x'}\frac{\partial \vec{r}_0}{\partial s} + \frac{1}{x'}x'\hat{\mu}_x + x\frac{1}{x'\dot{s}}\dot{\hat{\mu}}_x + \frac{1}{x'}y'\hat{\mu}_y + y\frac{1}{x'\dot{s}}\dot{\hat{\mu}}_y\right)\hat{\mu}_x \tag{2.27}$$

$$= \left(\frac{1}{x'}\hat{\mu}_s + \hat{\mu}_x + \frac{x}{x'\dot{s}}\frac{\dot{s}}{R}\hat{\mu}_s + \frac{y'}{x'}\hat{\mu}_y + \frac{y}{x'\dot{s}}0\right)\hat{\mu}_x = 1 \tag{2.28}$$

$$h_{\hat{\mu}_y} = \frac{\partial \vec{r}}{\partial y}\hat{\mu}_y = \left(\frac{1}{y'}\hat{\mu}_s + \frac{x'}{y'}\hat{\mu}_x + \frac{x}{y'R}\hat{\mu}_s + \hat{\mu}_y + y\frac{1}{y'\dot{s}}\dot{\hat{\mu}}_y\right)\hat{\mu}_y = 1 \tag{2.29}$$

$$h_{\hat{\mu}_s} = \frac{\partial \vec{r}}{\partial s}\hat{\mu}_s = \left(\hat{\mu}_s + x'\hat{\mu}_x + x\frac{1}{\dot{s}}\frac{\dot{s}}{R}\hat{\mu}_s + y'\hat{\mu}_y + y\frac{1}{\dot{s}}\dot{\hat{\mu}}_y\right)\hat{\mu}_s = 1 + \frac{x}{R} \tag{2.30}$$

Giving the line element of the particles curvilinear coordinate system [9]:

$$\boxed{d\vec{r} = \hat{\mu}_x dx + \hat{\mu}_y dy + \left(1 + \frac{x}{R}\right)\hat{\mu}_s ds} \tag{2.31}$$

When changing from a curved orbit in a dipole to a straight orbit in a drift section the coordinates continuously transform to a Cartesian coordinate system.

The position and its derivatives (velocity and acceleration) can be expressed in $K'(x, y, s)$ using the derived metric:

Position

$$\vec{r} = \vec{r}_0 + x\hat{\mu}_x + y\hat{\mu}_y \qquad (2.32)$$

Velocity

$$\dot{\vec{r}} = \dot{\vec{r}}_0 + \dot{x}\hat{\mu}_x + x\dot{\hat{\mu}}_x + \dot{y}\hat{\mu}_y + y\dot{\hat{\mu}}_y = \dot{s}\hat{\mu}_s + \dot{x}\hat{\mu}_x + \frac{x\dot{s}}{R}\hat{\mu}_s + \dot{y}\hat{\mu}_y + 0 \qquad (2.33)$$

$$\dot{\vec{r}} = \left(1 + \frac{x}{R}\right)\dot{s}\hat{\mu}_s + \dot{s}x'\hat{\mu}_x + \dot{s}y'\hat{\mu}_y \qquad (2.34)$$

Acceleration

$$\ddot{\vec{r}} = \frac{\dot{x}}{R}\dot{s}\hat{\mu}_s + \left(1 + \frac{x}{R}\right)\left(\ddot{s}\hat{\mu}_s + \dot{s}\dot{\hat{\mu}}_s\right) + \ddot{x}\hat{\mu}_x + \dot{x}\dot{\hat{\mu}}_x + \ddot{y}\hat{\mu}_y + \dot{y}\dot{\hat{\mu}}_y \qquad (2.35)$$

$$= \frac{\dot{x}}{R}\dot{s}\hat{\mu}_s + \left(1 + \frac{x}{R}\right)\left(\ddot{s}\hat{\mu}_s - \dot{s}\frac{\dot{s}}{R}\hat{\mu}_x\right) + \ddot{x}\hat{\mu}_x + \dot{x}\frac{\dot{s}}{R}\hat{\mu}_s + \ddot{y}\hat{\mu}_y + \dot{y}0 \qquad (2.36)$$

$$= \left(\frac{2\dot{x}\dot{s}}{R} + \left(1 + \frac{x}{R}\right)\ddot{s}\right)\hat{\mu}_s + \left(\ddot{x} - \left(1 + \frac{x}{R}\right)\frac{\dot{s}^2}{R}\right)\hat{\mu}_x + \ddot{y}\hat{\mu}_y \qquad (2.37)$$

$$\ddot{\vec{r}} = \left(\frac{2x'\dot{s}^2}{R} + \left(1 + \frac{x}{R}\right)\ddot{s}\right)\hat{\mu}_s + \left(x''\dot{s}^2 + x'\ddot{s} - \left(1 + \frac{x}{R}\right)\frac{\dot{s}^2}{R}\right)\hat{\mu}_x + \left(y''\dot{s}^2 + y'\ddot{s}\right)\hat{\mu}_y \qquad (2.38)$$

2.1.3. Movement of charged particles in electromagnetic fields

Electric and magnetic fields can be used to deflect and focus charged particles on the orbit. They induce the general Lorentz force [10]

$$\vec{F}_{Lorentz}^* = q \cdot (\vec{E} + \vec{v} \times \vec{B}) = q \cdot (\vec{E} + \dot{\vec{r}} \times \vec{B}) \qquad (2.39)$$

At relativistic speeds the comparison of $\vec{F}_{el}$ and $\vec{F}_{mag}$ shows:

$$E = c \cdot B. \qquad (2.40)$$

Meaning that the force of a $B = 1T$ magnet field on a relativistic particle corresponds to that of an electric field of $E = 3 \cdot 10^8 \frac{V}{m}$ making electric fields technically uninteresting for focussing and deflecting relativistic, charged particles.

Therefore the Lorentz force (Equation 2.39) can be reduced to the magnetic Lorentz force

$$\vec{F}_{Lorentz} = q \cdot \dot{\vec{r}} \times \vec{B} \qquad (2.41)$$

For stable movement on the orbit the Lorentz force must be in equilibrium with the centrifugal force corresponding to the curvature of the orbit.

$$\vec{F}_{Lorentz} = q\left(\dot{\vec{r}} \times \vec{B}\right) \overset{!}{=} \gamma m_0 \ddot{\vec{r}} \qquad (2.42)$$

Giving the acceleration of the particle:

$$\ddot{\vec{r}} = \frac{q}{\gamma m_0}\left(\dot{\vec{r}} \times \vec{B}\right) \qquad \text{with} \qquad \vec{B} = \begin{pmatrix} B_x \\ B_y \\ 0 \end{pmatrix}, \dot{\vec{r}} = \dot{s}\begin{pmatrix} x' \\ y' \\ \left(1 + \frac{x}{R}\right) \end{pmatrix}. \tag{2.43}$$

By equating to the general acceleration of the particle (Equation 2.38) we obtain the general (with respect to the assumptions already made) equations of motion for charged particles in magnetic fields:

$$\frac{q\dot{s}}{\gamma m_0}\begin{pmatrix} -\left(1 + \frac{x}{R}\right)B_y \\ \left(1 + \frac{x}{R}\right)B_x \\ x'B_y - y'B_x \end{pmatrix} = \begin{pmatrix} x''\dot{s}^2 + x'\ddot{s} - \left(1 + \frac{x}{R}\right)\frac{\dot{s}^2}{R} \\ y''\dot{s}^2 + y'\ddot{s} \\ \frac{2x'\dot{s}^2}{R} + \left(1 + \frac{x}{R}\right)\ddot{s} \end{pmatrix} \tag{2.44}$$

With $\vec{E} = 0$ the Lorentz force $\vec{F}_{Lorentz}$ is alway perpendicular to $\hat{\mu}_s$ meaning that $\ddot{s} = 0$ and simplifying the equations of motion.

$$\rightarrow \frac{q}{\gamma m_0 \dot{s}}\begin{pmatrix} -\left(1 + \frac{x}{R}\right)B_y \\ \left(1 + \frac{x}{R}\right)B_x \\ x'B_y - y'B_x \end{pmatrix} = \begin{pmatrix} x'' - \left(1 + \frac{x}{R}\right)\frac{1}{R} \\ y'' \\ 2\frac{x'}{R} \end{pmatrix} \tag{2.45}$$

The relation of the speed v of an actual particle on its individual trajectory to $\dot{s}$ of the ideal particle on the orbit (Figure 2.4) yields:

$$\frac{\dot{s}}{R} = \frac{v}{x + R} \tag{2.46}$$

$$\rightarrow v = \dot{s}\left(1 + \frac{x}{R}\right) \tag{2.47}$$

So the equations of motion can be expressed as

$$\boxed{\frac{q}{p}\begin{pmatrix} -\left(1 + \frac{x}{R}\right)^2 B_y \\ \left(1 + \frac{x}{R}\right)^2 B_x \\ \left(1 + \frac{x}{R}\right)(x'B_y - y'B_x) \end{pmatrix} = \begin{pmatrix} x'' - \left(1 + \frac{x}{R}\right)\frac{1}{R} \\ y'' \\ 2\frac{x'}{R} \end{pmatrix}}$$

$$\tag{2.48}$$
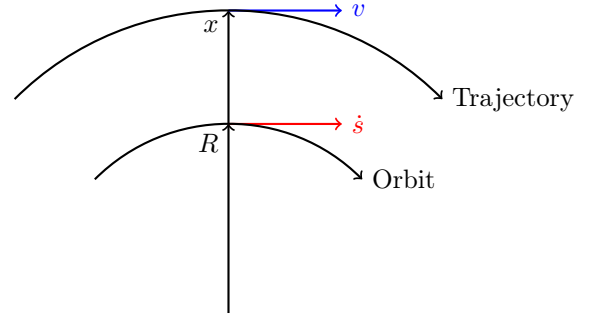
Figure 2.4.: Relation of particles speed on the orbit $\dot{s}$ and an arbitrary trajectory v [7]

The solution of these is discussed in section 2.1.5.

2.1.4. The magnetic field near the orbit

The magnetic field on the orbit be only composed of transverse fields so $\vec{B} = (B_x, B_y, 0)$. As only the magnetic field in direct proximity of the orbit is relevant for the particle movement of interest it is obvious to simplify the magnetic fields by using a series expansion at the orbit $x_0 = y_0 = 0^{[10]}$.

$$B_y(x) = B_{y,0} + \frac{dB_y}{dx}x + \frac{1}{2!}\frac{d^2B_y}{dx^2}x^2 + \frac{1}{3!}\frac{d^3B_y}{dx^3}x^3 + ... \tag{2.49}$$

Multiplication with $\frac{q}{p}$ yields

$$\frac{q}{p}B_y(x) = \frac{q}{p}B_{y,0} \qquad +\frac{q}{p}\frac{dB_y}{dx}x \qquad +\frac{q}{p}\frac{1}{2!}\frac{d^2B_y}{dx^2}x^2 \qquad +\frac{q}{p}\frac{1}{3!}\frac{d^3B_y}{dx^3}x^3 \qquad +... \tag{2.50}$$

$$= \frac{1}{R} \qquad +kx \qquad +\frac{1}{2!}mx^2 \qquad +\frac{1}{3!}ox^3 \qquad +... \tag{2.51}$$

Each term of the series expansion resembles one magnet type. An overview of the individual types and their purpose can be found below (Table 2.1). For particles inside the vacuum chamber the current density can be neglected and outside of cavities the electric field is zero so the Maxwell-Ampère equation tells us:

$$\vec{\nabla} \times \vec{B} = \mu_0\left(\vec{J} + \epsilon_0\frac{\partial\vec{E}}{\partial t}\right) \overset{!}{=} 0 \qquad \text{with } \vec{E} = \vec{J} = 0 \tag{2.52}$$

yielding the correlation between the transverse magnetic fields:

$$\frac{\partial B_x}{\partial y} = \frac{\partial B_y}{\partial x} \tag{2.53}$$

and telling us that the magnetic field approximation (Equation 2.50) also holds when x and y are exchanged and in direct consequence it must be impossible to have radial and axial focussing magnetic field. This work only considers plane accelerators so $R \to \infty$ in the axial plane.

$$B_x(y) = \frac{dB_y}{dx}y + \frac{1}{2!}\frac{d^2B_y}{dx^2}y^2 + \frac{1}{3!}\frac{d^3B_y}{dx^3}y^3 + ... \tag{2.54}$$

Magnet	Purpose	Definition
Dipole	Deflection of the particles	$B = \frac{p}{e}\frac{1}{R}$
Quadrupol	Linear transverse focussing	$\frac{dB}{dx} = \frac{p}{e}k$
Sextupol		$\frac{d^2B}{dx^2} = \frac{p}{e}m$
Octupole	Nonlinear transverse focussing	$\frac{d^3B}{dx^3} = \frac{p}{e}o$
N-pole		$\frac{d^NB}{dx^N} = \frac{p}{e}...$

Table 2.1.: Types of magnets for accelerators

Linear beam optics refers to the first two types of magnets with magnetic fields either constant or as a linear function of the perpendicular distance from the orbit. Higher order multipoles are intrinsically included as field errors in real magnets (-edges) and are also specifically used to compensate chromatic aberration from the quadrupoles whos focussing strength also linearly depends on the momentum. and other errors induced by the linear optics.

2.1.5. Linear, transverse EOM

When considering highly relativistic particles the influence of the magnetic fields on the longitudinal speed is negligible[10]. Therefore only the transverse EOM (Equation 2.48) for charged particles in accelerator coordinates are considered. For off-momentum particles ($p = p_0 + \Delta p$) with $\Delta p \ll p_0$ (at BESSY II $< 4‰$) the linear approximation of the Taylor series $\frac{1}{1+x} = 1 - x + ...$ gives[9]

$$\frac{1}{p} = \frac{1}{p_0 + \Delta p} = \frac{1}{p_0}\left(\frac{1}{1 + \frac{\Delta p}{p_0}}\right) \approx \frac{1}{p_0}\left(1 - \frac{\Delta p}{p_0}\right) = \frac{1 - \delta}{p_0} \tag{2.55}$$

with the relative momentum offset δ. Taking note of the convention to give focussing quadrupole strengths k a negative sign the linear parts of the magnetic field series (Equations 2.50, 2.54) are:

$$\frac{q}{p_0}B_y(x) = \frac{1}{R} - kx \tag{2.56}$$

$$\frac{q}{p_0}B_x(y) = -ky \tag{2.57}$$

and can be inserted into the transverse, linear EOM (Equation 2.48) with notation $p_0 = p$ giving

$$(1 - \delta)\begin{pmatrix} -\left(1 + \frac{x}{R}\right)^2\left(\frac{1}{R} - kx\right) \\ -\left(1 + \frac{x}{R}\right)^2 k_y \end{pmatrix} = \begin{pmatrix} x'' - \left(1 + \frac{x}{R}\right)\frac{1}{R} \\ y'' \end{pmatrix}. \tag{2.58}$$

Multiplying these out and neglecting higher powers and products of x, y and δ (all $\ll 1$) the linear EOM for charged particles in magnetic fields are obtained:

$$\boxed{\begin{pmatrix} x''(s) + \left(\frac{1}{R^2(s)} - k(s)\right)x(s) \\ y''(s) + k(s)y(s) \end{pmatrix} = \begin{pmatrix} \frac{\delta}{R(s)} \\ 0 \end{pmatrix}.} \tag{2.59}$$

2.1.6. Solutions to the linear, transverse EOM

The solutions to the transverse, linear EOM (Equation 2.59) for ideal particles ($\delta = 0$) are best found with a hard edge model. Assuming constant fields in the magnets and discrete transition between different accelerator elements the EOM can be separately solved for each linear element with respect to the initial conditions[9]

$$\vec{x}(0) = \begin{pmatrix} x(0) \\ x'(0) \\ y(0) \\ y'(0) \\ l(0) \\ \delta(0) \end{pmatrix} = \begin{pmatrix} x_0 \\ x_0' \\ y_0 \\ y_0' \\ l_0 \\ \delta_0 \end{pmatrix} = \begin{pmatrix} \text{radial spacial offset} \\ \text{radial directional offset} \\ \text{axial spacial offset} \\ \text{axial directional offset} \\ \text{longitudinal spacial offset} \\ \text{longitudinal energy offset} \end{pmatrix}. \tag{2.60}$$

<u>Drift</u>
With $R \to \infty$ and $k(s) = 0$ the EOM simplify to

$$x''(s) = 0 \tag{2.61}$$

$$y''(s) = 0. \tag{2.62}$$

Which can be easily solved to

$$u(s) = As + B \tag{2.63}$$

$$u'(s) = A \tag{2.64}$$

with $u = x, y$. The constants of integration can be retrieved from the initial conditions (Equation 2.60) revealing

$$\boxed{\begin{aligned} u(s) &= u_0's + u_0 \\ u'(s) &= u_0' \end{aligned}} \tag{2.65}$$

Quadrupole

With $R \to \infty$ and $k(s) = const$ for each quadrupole and $k < 0$ in the focussing plane the EOM for a radial focussing quadrupole give:

$$x''(s) + kx(s) = 0 \tag{2.66}$$

$$y''(s) - ky(s) = 0. \tag{2.67}$$

These EOM resemble second-order ordinary linear homogeneous differential equations with constant coefficients. With $\omega = \pm\sqrt{k}$ the simple harmonic oscillator ($u'' = \mp\omega^2 u$) can be recognized. The linear independent characteristic solutions can be analytically derived and are well known. With $\Omega = \sqrt{k}s$ they can be written as

$$x(s) = A\cos(\Omega) + B\sin(\Omega) \tag{2.68}$$

$$x'(s) = -A\sqrt{k}\sin(\Omega) + B\sqrt{k}\cos(\Omega) \tag{2.69}$$

$$y(s) = C\cosh(\Omega) + D\sinh(\Omega) \tag{2.70}$$

$$y'(s) = C\sqrt{k}\sinh(\Omega) + D\sqrt{k}\cosh(\Omega). \tag{2.71}$$

With the initial conditions (Equation 2.60) the constants of integration can be retrieved revealing

$$\boxed{\begin{aligned} x(s) &= x_0\cos(\Omega) + \frac{x_0'}{\sqrt{k}}\sin(\Omega) \\ x'(s) &= -x_0\sqrt{k}\sin(\Omega) + x_0'\cos(\Omega) \\ y(s) &= y_0\cosh(\Omega) + \frac{y_0'}{\sqrt{k}}\sinh(\Omega) \\ y'(s) &= y_0\sqrt{k}\sinh(\Omega) + y_0'\cosh(\Omega) \end{aligned}} \tag{2.72}$$

For an axial focussing quadrupole the solutions for $x(s)$ and $y(s)$ must be exchanged.

Dipole

With $R = const.$ and $k(s) = 0$ the EOM are

$$x''(s) + \frac{x(s)}{R^2}x(s) = \frac{\delta}{R} \tag{2.73}$$

$$y''(s) = 0. \tag{2.74}$$

In the axial plane a dipole corresponds to a drift (Equation 2.65) with $s = R\alpha$ (arc length) where α is

the bending angle of the dipole. The solution to the homogeneous part of the radial EOM for ideal particles with $\delta = 0$

$$x_h''(s) + \frac{u(s)}{R^2} x_h(s) = 0 \tag{2.75}$$

again corresponds to the well known harmonic oscillator and is easily found.

$$x_h(s) = A\cos(\alpha) + B\sin(\alpha) \tag{2.76}$$

$$x_h'(s) = -\frac{A}{R}\sin(\alpha) + \frac{B}{R}\cos(\alpha) \tag{2.77}$$

The general solution to the inhomogeneous EOM for off-momentum particles can be written as the sum of the complementary solution x_h and the particular solution x_p - later refered to as the dispersion. Since the inhomogeneity is constant $x_p = const$ is a suitable approach. When inserted into the EOM (Equation 2.73) it yields:

$$x_p = \delta R \tag{2.78}$$

giving a general solution to equation 2.73:

$$x(s) = A\cos(\alpha) + B\sin(\alpha) + \delta R \tag{2.79}$$

$$x'(s) = -\frac{A}{R}\sin(\alpha) + \frac{B}{R}\cos(\alpha). \tag{2.80}$$

With the initial conditions (Equation 2.60) the constants of integration can be retrieved revealing

$$\boxed{\begin{aligned} x(s) &= x_0\cos(\alpha) + x_0' R\sin(\alpha) + \delta[R(1 - \cos(\alpha))] \\ x'(s) &= -x_0\frac{\sin(\alpha)}{R} + x_0'\cos(\alpha) + \delta\sin(\alpha). \end{aligned}} \tag{2.81}$$

2.1.7. Longitudinal motion

The longitudinal offset of an arbitrary particle from the ideal particle ($\vec{x} = \vec{0}$) be $l(0)$. With constant relative momentum offset [9]

$$\boxed{\delta(s) = \delta(0) = \delta_0 = const} \tag{2.82}$$

a formula for the longitudinal spacial offset $l(s)$ for this particle when the reference particle covers the distance s on the orbit can be derived. Two effects must be considered: the path length difference Δs_1 due to particle momentum dependant bending radii in the dipoles and the path length difference Δs_2 due to different speeds (only relevant for $v < c$).

$$l(s) = l(0) - \Delta s_1 + \Delta s_2 \tag{2.83}$$

$$\Delta s_1 = L - S \tag{2.84}$$

$$\Delta s_2 = t_0\Delta v \tag{2.85}$$

With the acutally travelled distance L, the distance on the orbit s, the time of flight for the reference particle from 0 to s being t_0 and the speed difference $\Delta v = v - v_0$. So in total $l(s)$ becomes

$$l(s) = l(0) - (L - s) + t_0\Delta v. \tag{2.86}$$

With some relations from relativistic kinematics (Appendix A.2) we get:

$$\Delta s_2 = t_0 \Delta v = \frac{s}{v_0} \Delta v = s \frac{\Delta v}{v_0} \approx s \frac{\delta}{\gamma^2}. \tag{2.87}$$

The actually travelled distance L can be calculated from the line element (Equation 2.31):

$$L = \int_0^s \left\| \frac{d\vec{r}}{ds} \right\| ds = \int_0^s \left\| \begin{pmatrix} x'(s) \\ y'(s) \\ 1 + \frac{x(s)}{R} \end{pmatrix} \right\| ds = \int_0^s \sqrt{x'^2(s) + y'^2(s) + \left(1 + \frac{x(s)}{R}\right)^2} ds. \tag{2.88}$$

In linear approximation L reduces to:

$$L = \int_0^s \left(1 + \frac{x(s)}{R}\right) ds = s + \frac{1}{R} \int_0^s x(s) ds \tag{2.89}$$

$$\rightarrow \Delta s_1 = L - s = \frac{1}{R} \int_0^s x(s) ds. \tag{2.90}$$

Drift and quadrupole
For curvature free elements with $R \rightarrow \infty$ we obtain $\Delta s_1 = 0$ and thus with equation 2.87 follows:

$$\boxed{l(s) = l(0) + s \frac{\delta}{\gamma^2}} \tag{2.91}$$

Dipole
To get Δs_1 for Dipoles Equation 2.81 must be inserted in 2.90 revealing

$$\Delta s_1 = \frac{x_0}{R} \int_0^s \cos\left(\frac{s}{R}\right) ds + x_0' \int_0^s \sin\left(\frac{s}{R}\right) ds + \delta \int_0^s \left[1 - \cos\left(\frac{s}{R}\right)\right] ds \tag{2.92}$$

$$= x_0 \sin\left(\frac{s}{R}\right) - x_0' R \left[\cos\left(\frac{s}{R}\right) - 1\right] + \delta \left[s - R \sin\left(\frac{s}{R}\right)\right]. \tag{2.93}$$

By inserting equations 2.87 and 2.93 in 2.83 we obtain

$$\boxed{l(s) = l(0) - x_0 \sin\left(\frac{s}{R}\right) - x_0' R \left[1 - \cos\left(\frac{s}{R}\right)\right] + \delta \left[s \frac{\delta}{\gamma^2} - s + R \sin\left(\frac{s}{R}\right)\right]} \tag{2.94}$$

2.1.8. Transfer matrix

The linear optics of charged particles can be calculated with matrices just as in geometrical optics. For fully describing a moving particle the six dimensional phase space is required. In accelerator physics the particle vector (Equation 2.60) is usually defined. It differs from the often used standard coordinates in the six dimensional phase space [11]:

$$\begin{pmatrix} x \\ x' \\ y \\ y' \\ z \\ z' \end{pmatrix} = \begin{pmatrix} 1 & 0 & 0 & 0 & 0 & 0 \\ 0 & 0 & 0 & 1 & 0 & 0 \\ 0 & 1 & 0 & 0 & 0 & 0 \\ 0 & 0 & 0 & 0 & 1 & 0 \\ 0 & 0 & 1 & 0 & 0 & 0 \\ 0 & 0 & 0 & 0 & 0 & 1 \end{pmatrix} \begin{pmatrix} x \\ y \\ z \\ x' \\ y' \\ z' \end{pmatrix} \quad \text{with } T_{Acc.CS}^{Std.CS} = T_A^S = \begin{pmatrix} 1 & 0 & 0 & 0 & 0 & 0 \\ 0 & 0 & 0 & 1 & 0 & 0 \\ 0 & 1 & 0 & 0 & 0 & 0 \\ 0 & 0 & 0 & 0 & 1 & 0 \\ 0 & 0 & 1 & 0 & 0 & 0 \\ 0 & 0 & 0 & 0 & 0 & 1 \end{pmatrix}. \tag{2.95}$$

But can easily be transformed back and forth with the transformation T_A^S. The particle vector (Equation 2.60) can be transformed along its trajectory with the transfer matrix R (amongst others also known as the R-matrix or transport matrix).

$$R = \begin{pmatrix} R_{11} & R_{12} & R_{13} & R_{14} & R_{15} & R_{16} \\ R_{21} & R_{22} & R_{23} & R_{24} & R_{25} & R_{26} \\ R_{31} & R_{32} & R_{33} & R_{34} & R_{35} & R_{36} \\ R_{41} & R_{42} & R_{43} & R_{44} & R_{45} & R_{46} \\ R_{51} & R_{52} & R_{53} & R_{54} & R_{55} & R_{56} \\ R_{61} & R_{62} & R_{63} & R_{64} & R_{65} & R_{66} \end{pmatrix} = \begin{pmatrix} (x|x_0) & (x|x_0') & (x|y_0) & (x|y_0') & (x|l_0) & (x|\delta_0) \\ (x'|x_0) & (x'|x_0') & (x'|y_0) & (x'|y_0') & (x'|l_0) & (x'|\delta_0) \\ (y|x_0) & (y|x_0') & (y|y_0) & (y|y_0') & (y|l_0) & (y|\delta_0) \\ (y'|x_0) & (y'|x_0') & (y'|y_0) & (y'|y_0') & (y'|l_0) & (y'|\delta_0) \\ (l|x_0) & (l|x_0') & (l|y_0) & (l|y_0') & (l|l_0) & (l|\delta_0) \\ (\delta|x_0) & (\delta|x_0') & (\delta|y_0) & (\delta|y_0') & (\delta|l_0) & (\delta|\delta_0) \end{pmatrix}$$

(2.96)

It maps the particle vector along its trajectory.

$$\vec{r}(s_n) = R(s_1 \to s_n) \cdot \vec{r}(0) = R(s_{n-1} \to s_n)R(s_{n-2} \to s_{n-1})...R(s_1 \to s_2) \cdot \vec{r}(0) \qquad (2.97)$$

The transfer matrix can be simplified with assumptions that hold for most accelerators. Taking into account that $\frac{\Delta p}{p_0} = \delta = const$ in a conservative system and that all effects of the magnets on the particles are independent of l leads to:

$$\begin{pmatrix} R_{11} & R_{12} & R_{13} & R_{14} & 0 & R_{16} \\ R_{21} & R_{22} & R_{23} & R_{24} & 0 & R_{26} \\ R_{31} & R_{32} & R_{33} & R_{34} & 0 & R_{36} \\ R_{41} & R_{42} & R_{43} & R_{44} & 0 & R_{46} \\ R_{51} & R_{52} & R_{53} & R_{54} & 1 & R_{56} \\ 0 & 0 & 0 & 0 & 0 & 1 \end{pmatrix}$$

(2.98)

Furthermore the mid plane symmetry

$$B_x(x, y, s) = -B_x(x, -y, s) \qquad (2.99)$$

$$B_y(x, y, s) = +B_y(x, -y, s) \qquad (2.100)$$

$$B_s(x, y, s) = -B_s(x, -y, s) \qquad (2.101)$$

holds for most accelerators resulting in decoupled radial and axial components of the transfer matrix.

$$\begin{pmatrix} R_{11} & R_{12} & 0 & 0 & 0 & R_{16} \\ R_{21} & R_{22} & 0 & 0 & 0 & R_{26} \\ 0 & 0 & R_{33} & R_{34} & 0 & 0 \\ 0 & 0 & R_{43} & R_{44} & 0 & 0 \\ R_{51} & R_{52} & 0 & 0 & 1 & R_{56} \\ 0 & 0 & 0 & 0 & 0 & 1 \end{pmatrix}$$

(2.102)

Dispersion in dipoles couples longitudinal and radial motion, hence R_{51}, R_{52}, R_{56}, R_{16} and R_{26} are not zero. Neglecting radiation loss and interaction with the residual gas amongst other minor effects Liouville's theorem holds for accelerators in first approximation. So phase space must be conserved

$$det(R) = 1 \qquad (2.103)$$

For uncoupled machines this also holds for each plane separately $det(R_x) = det(R_y) = 1$.
Furthermore the Hamiltonian formalism shows us that R must be simplectic since it performs a
canonical transformation meaning

$$R^\mathsf{T}\Omega R \stackrel{!}{=} \Omega \qquad \text{with} \qquad \Omega = \begin{pmatrix} 0 & \mathbb{1}_3 \\ -\mathbb{1}_3 & 0 \end{pmatrix} \tag{2.104}$$

must hold. Ω must be transformed to accelerator coordinates

$$\Omega = T_A^S \Omega T_A^{S\,T} = \begin{pmatrix} 0 & 1 & 0 & 0 & 0 & 0 \\ -1 & 0 & 0 & 0 & 0 & 0 \\ 0 & 0 & 0 & 1 & 0 & 0 \\ 0 & 0 & -1 & 0 & 0 & 0 \\ 0 & 0 & 0 & 0 & 0 & 1 \\ 0 & 0 & 0 & 0 & -1 & 0 \end{pmatrix} \tag{2.105}$$

The equations from symplecticity and Liouvilles theorem can be used to eliminate further variables
in the R-matrix (Equation 2.102) giving:

$$R = \begin{pmatrix} r_{11} & r_{12} & 0 & 0 & 0 & r_{16} \\ r_{21} & \frac{r_{12}r_{21}+1}{r_{11}} & 0 & 0 & 0 & r_{26} \\ 0 & 0 & r_{33} & r_{34} & 0 & 0 \\ 0 & 0 & r_{43} & \frac{r_{34}r_{43}+1}{r_{33}} & 0 & 0 \\ r_{16}r_{21} - r_{11}r_{26} & \frac{r_{12}r_{21}r_{16}+r_{16}-r_{11}r_{12}r_{26}}{r_{11}} & 0 & 0 & 1 & r_{56} \\ 0 & 0 & 0 & 0 & 0 & 1 \end{pmatrix} \tag{2.106}$$

From the derived equations for $x(s)$, $x'(s)$, $y(s)$, $y'(s)$, $l(s)$ and $\delta(s)$ in the sections 2.1.6, 2.1.7 the
R-matrix for each element can be directly written down.

Drift

$$R_{DRIFT} = \begin{pmatrix} 1 & L & 0 & 0 & 0 & 0 \\ 0 & 1 & 0 & 0 & 0 & 0 \\ 0 & 0 & 1 & L & 0 & 0 \\ 0 & 0 & 0 & 1 & 0 & 0 \\ 0 & 0 & 0 & 0 & 1 & L/\gamma^2 \\ 0 & 0 & 0 & 0 & 0 & 1 \end{pmatrix} \tag{2.107}$$

Uninform dipole as sector bending magnet

$$R_{SBEND} = \begin{pmatrix} \cos(\alpha) & R\sin(\alpha) & 0 & 0 & 0 & R(1-\cos(\alpha)) \\ -\sin(\alpha)/R & \cos(\alpha) & 0 & 0 & 0 & \sin(\alpha) \\ 0 & 0 & 1 & L & 0 & 0 \\ 0 & 0 & 0 & 1 & 0 & 0 \\ -\sin(\alpha) & -R(1-\cos(\alpha)) & 0 & 0 & 1 & R(\alpha/\gamma^2 - \alpha + \sin(\alpha))L \\ 0 & 0 & 0 & 0 & 0 & 1 \end{pmatrix} \tag{2.108}$$

Radial focussing and radial defocussing quadrupole

$$
R_{QF} = \begin{pmatrix}
\cos(\Omega) & \sin(\Omega)/\sqrt{k} & 0 & 0 & 0 & 0 \\
-\sqrt{k}\sin(\Omega) & \cos(\Omega) & 0 & 0 & 0 & 0 \\
0 & 0 & \cosh(\Omega) & \sinh(\Omega)/\sqrt{k} & 0 & 0 \\
0 & 0 & \sqrt{k}\sinh(\Omega) & \cosh(\Omega) & 0 & 0 \\
0 & 0 & 0 & 0 & 1 & L/\gamma^2 \\
0 & 0 & 0 & 0 & 0 & 1
\end{pmatrix}
\tag{2.109}
$$

$$
R_{QD} = \begin{pmatrix}
\cosh(\Omega) & \sinh(\Omega)/\sqrt{k} & 0 & 0 & 0 & 0 \\
\sqrt{k}\sinh(\Omega) & \cosh(\Omega) & 0 & 0 & 0 & 0 \\
0 & 0 & \cos(\Omega) & \sin(\Omega)/\sqrt{k} & 0 & 0 \\
0 & 0 & -\sqrt{k}\sin(\Omega) & \cos(\Omega) & 0 & 0 \\
0 & 0 & 0 & 0 & 1 & L/\gamma^2 \\
0 & 0 & 0 & 0 & 0 & 1
\end{pmatrix}
\tag{2.110}
$$

2.1.9. Focussing dipole edge

Often the dipole yoke is composed of parallel flat metal sheets so that there is an angle β between the orbit normal plane and the pole face plane at the entrance to the dipole. The effect of this edge angle in the radial plane is easily derived from geometry (Figure 2.5). Particles with $x_0 > 0$ enter the magnetic field later when the pole face angle β is greater than zero. They travel $\Delta s = x_0 \tan(\beta)$ less distance in the field. This is equivalent to an angle kick of[9]

$$
\Delta x' = \frac{\Delta s}{R} = x_0 \frac{\tan(\beta)}{R}
\tag{2.111}
$$

that changes its sign if $x_0 < 0$. The offset $x = x_0$ is preserved. The fringe field of the dipole has components normal to the pole shoe face with opposite signs over and below the orbit. When the pole shoe face is perpendicular to the orbit these are parallel to v_s and can be neglected. But when the pole face plane is rotated by β particles with an axial offset y_0 see a B_x field component corresponding to an axial angle kick. This can be approximated by integrating B_x along the pole face plane normal vector $\hat{\mu}_z$ [10]
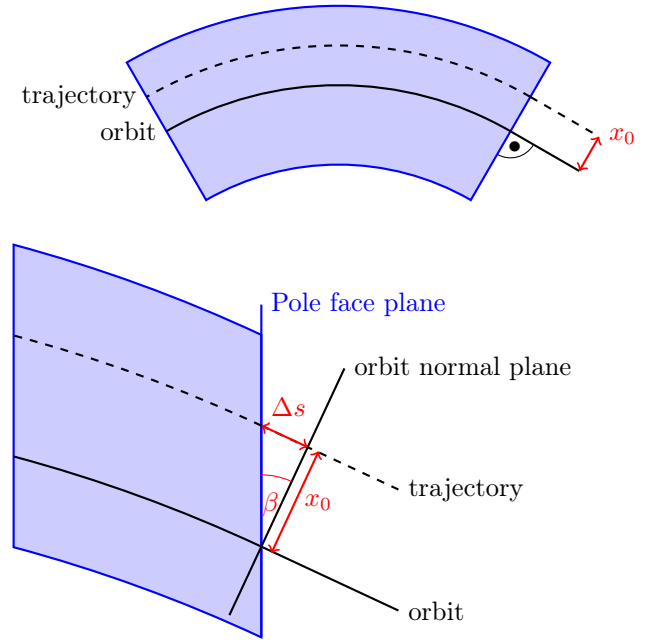

Figure 2.5.: (Above) Sector dipole magnet with pole face planes perpendicular to the orbit
(Below) Rectangular dipole magnet with angle β between pole face plane and orbit normal plane[7]

$$
\Delta y' \approx \frac{1}{B_0 R} \int B_x dz = -y_0 \frac{\tan(\beta)}{R}
\tag{2.112}
$$

or to include the decreasing axial offset y due to the focussing effect and the actual edge angle due to curvature of the trajectory[9]

$$\Delta y' = \frac{1}{B_0 R} \int B_x ds \approx -y_0 \left(-\frac{\tan(\beta)}{R} + \frac{g}{R^2} \frac{1+\sin^2(\beta)}{\cos^3(\beta)} K \right) \tag{2.113}$$

with the pole shoe gap g and the fringe field integral K. With $\vec{z} \perp$ pole shoe plane the fringe field integral is[9]

$$K = \int_{innerField}^{outsideField} \frac{B_y (B_0 - B_y)}{g B_0^2} dz \approx \begin{cases} 0.45, & \text{for rectangular pole shoe.} \\ 0.7, & \text{for Rogowski formed pole shoe} \end{cases} \tag{2.114}$$

So in total the effect of a rotated pole face plane on the particles is given by the R-matrix

$$R_{EDGE} = \begin{pmatrix} 1 & 0 & 0 & 0 & 0 & 0 \\ \frac{\tan(\beta)}{R} & 1 & 0 & 0 & 0 & 0 \\ 0 & 0 & 1 & 0 & 0 & 0 \\ 0 & 0 & -\frac{\tan(\beta)}{R} + \frac{g}{R^2}\frac{1+\sin^2(\beta)}{\cos^3(\beta)} K & 1 & 0 & 0 \\ 0 & 0 & 0 & 0 & 1 & 0 \\ 0 & 0 & 0 & 0 & 0 & 1 \end{pmatrix} \tag{2.115}$$

The total transport matrix of a dipole can now be de written as

$$R_{RBEND} = R_{EDGE} R_{SBEND} R_{EDGE} \tag{2.116}$$

with $\beta = \frac{\alpha}{2}$ for a rectangular dipole with parallel pole face planes on each side and error free positioning.

2.1.10. Twiss parameters and phase ellipse

The solutions to the transverse, linear EOM (Equation 2.59) for individual particles ($\delta = const$) were found with a rectangular field model as shown in section 2.1.6 and give the transformation of each element of the six dimensional particle vector. This transformation can be written as a matrix - the transport matrix. In this section we want to derive special lattice functions that allow us to describe the beam as an ensemble of many particles oscillating around the reference trajectory (orbit). The Hill differential equations follow from the linear EOM with s dependant quadrupole strengths and mono energetic particles[10]:

$$x''(s) = k_x(s)x(s) \qquad \text{with} \qquad k_x(s) = -\frac{1}{R^2(s)} + \frac{q}{p}\frac{\partial dB_y}{\partial x} \tag{2.117}$$

$$y''(s) = k_y(s)y(s) \qquad \text{with} \qquad k_y(s) = -\frac{q}{p}\frac{\partial dB_y}{\partial x} \tag{2.118}$$

The Hill differential equations correspond to a harmonic oscillator with s dependant restoring force. They were originally used in astronomy to investigate the stability of lunar orbits. In accelerators the transverse offsets $u(s)$ oscillate with s dependent phase and amplitude around the orbit. The first application to accelerators was to describe orbit stability in betatrons therefore the oscillation amplitude functions are known as the betatron functions $\beta_u(s)$. With a change of variables introducing the first two Twiss parameters $\beta(s) = u^2(s)$ and $\alpha(s) := -\frac{\beta'(s)}{2}$ the solution to

these EOM can be written as (for detailed derivation see[10]):

$$u(s) = \sqrt{\epsilon\beta(s)}\cos(\Psi(s) + \phi) \tag{2.119}$$

$$u'(s) = -\sqrt{\frac{\epsilon}{\beta(s)}}[\alpha(s)\cos(\Psi(s) + \phi) + \sin(\Psi(s) + \phi)] \tag{2.120}$$

The amplitude factor $\sqrt{\epsilon}$ (section 2.3) corresponds to the 1σ occupied phase space surface by the ensemble. ϵ and the phase offset ϕ are constants of integration. The betatron function $\beta(s)$ is periodic in s for closed orbits so $\beta(s + L) = \beta(s)$ where L could be the circumference C of the machine. The phase Ψ advances from 0 to 2π over one period length L and is given by

$$\Psi(s) = \int_0^s \frac{d\overline{s}}{\beta(\overline{s})}). \tag{2.121}$$

In closed orbit machines the amount of oscillations per revolution is the tune.

$$Q_u = \frac{\Psi(s + C) - \Psi(s)}{2\pi} = \frac{1}{2\pi}\int_s^{s+C} \frac{d\overline{s}}{\beta_u(\overline{s})} \tag{2.122}$$

The ensemble of particles perform betatron oscillations determined by the focussing magnet structure. The envelope function $E_u(s) = \sqrt{\epsilon_u\beta_u(s)}$ reflects the beam width (Figure 2.6) that is determined by the betatron oscillation amplitude and the emittance of the ensemble neglecting dispersion.
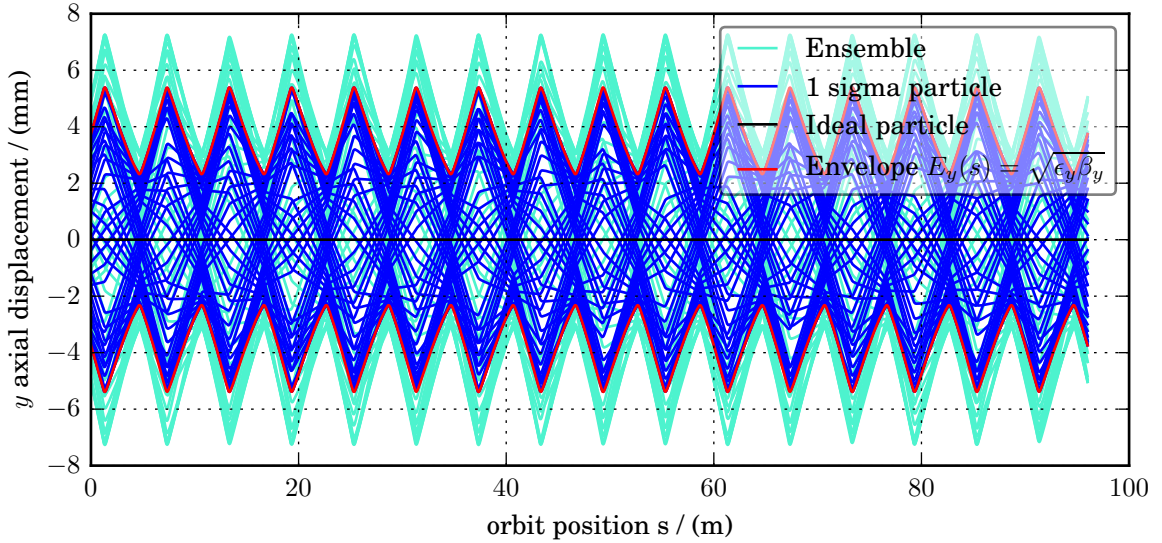
Figure 2.6.: Axial beam extent over the BESSY II booster lattice calculated and plotted with AC-CPY[1,2]

The Ψ-dependence can be eliminated by inserting equation 2.119 solved for $\cos(\Psi(s) + \phi)$ into equation 2.120 and solving for $\sin((\Psi(s) + \phi)$:

$$\cos(\Psi(s) + \phi) = \frac{u(s)}{\sqrt{\epsilon\beta(s)}} \tag{2.123}$$

$$\sin((\Psi(s) + \phi) = \frac{\sqrt{\beta(s)}u'(s)}{\sqrt{\epsilon}} + \frac{\alpha(s)u(s)}{\sqrt{\epsilon\beta(s)}} \tag{2.124}$$

2. Theory

Then the square of the gained results can be inserted into $\sin^2(\Psi) + \cos^2(\Psi) = 1$ and solved for ϵ:

$$\epsilon = \frac{u^2(s)}{\beta(s)} + \left((\sqrt{\beta(s)}u'(s) + \frac{\alpha(s)u(s)}{\sqrt{\beta(s)}} \right)^2 \tag{2.125}$$

$$= \frac{1 + \alpha^2(s)}{\beta(s)}u^2(s) + 2\alpha(s)u'(s)u(s) + \frac{\alpha^2(s)}{\beta(s)}u'^2(s) \tag{2.126}$$

By introducing the third Twiss parameter $\gamma := \frac{1+\alpha^2(s)}{\beta(s)}$ we can write:

$$\boxed{\epsilon = \gamma(s)u^2(s) + 2\alpha(s)u(s)u'(s) + \beta(s)u'^2(s)} \tag{2.127}$$
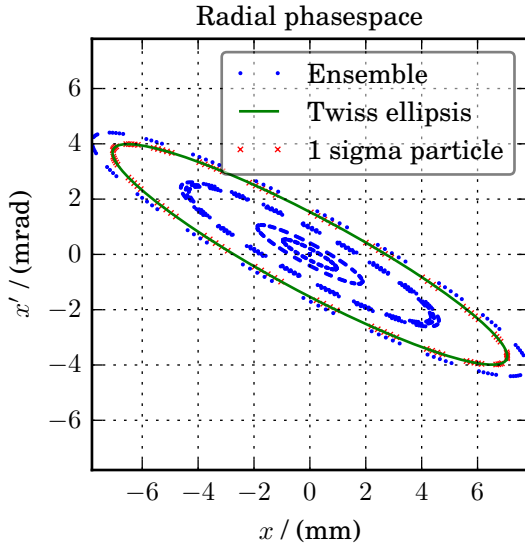
Figure 2.7.: Tracked particles and phase ellipses calculated from twiss parameters [1]

This equation describes an ellipse in the u-u'-plane (Figure 2.7) on which the particles advance with every revolution. The emittance ϵ times π gives the area of the ellipse[9]

$$\int_{ellipse} dudu' = \pi\epsilon_u \tag{2.128}$$

which according to Liouville's theorem must stay constant in a conservative system where the particle movement is described by canonical EOM. The shape and angle of the ellipse change with the Twiss parameters $\beta(s)$, $\alpha(s)$ and $\gamma(s)$ while its area and the emittance ϵ as constant of integration are conserved.

If the ensemble of particles is normally distributed the transverse charge density distribution is given by:

$$\rho(x, y) = \frac{Nq}{2\pi\sigma_x\sigma_y} \exp\left(\frac{-x^2}{2\sigma_x^2} + \frac{-y^2}{2\sigma_y^2} \right). \tag{2.129}$$

All particles with less than one standard deviation transverse offset move inside the ellipse that is determined by the 1σ emittance and neglecting dispersion lead to a beam width of

$$\sigma_u(s) = \sqrt{\epsilon_u^{1\sigma}\beta_u(s)} \tag{2.130}$$

The superscript 1σ can be left away as this is the standard convention in electron accelerator physics meaning that the emittance ϵ usually refers to 60.7% of the particles of one plane. The transverse acceptance of an accelerator is defined by the maximum emittance value for the beam to fit the vacuum chamber. It refers to the optically tightest spot where the proportion of the vacuum chamber aperture d to the beam width σ_u is minimal:

$$A_u = \left(\frac{d^2}{\beta_u} \right)_{min} \tag{2.131}$$

For storage rings as a rule of thumb the acceptance should be 50 times greater then the emittance [10].

2.1.11. Transformation of Twiss parameters

The Twiss parameters are useful for describing the movement of an ensemble of particles. The transformation of these using the transfer matrices in analogy to the transformation of the particle vector (Equation 2.97) can be derived as shown in[10]. The betamatrix (subscript u left away)

$$B(s) := \begin{pmatrix} \beta(s) & -\alpha(s) \\ -\alpha(s) & \gamma(s) \end{pmatrix} \tag{2.132}$$

with $det(B) = 1$ transforms according to:

$$B(s) = R_{0 \to s} B(0) R_{0 \to s}^T \tag{2.133}$$

so that the transformation of Twiss parameters can be written as:

$$\boxed{\beta^f = R_{11}^2 \beta^i - 2R_{11}R_{12}\alpha^i + R_{12}^2 \gamma^i} \tag{2.134}$$

$$\boxed{\alpha^f = -R_{11}R_{21}\beta^i + (R_{12}R_{21} + R_{11}R_{22})\alpha^i - R_{12}R_{22}\gamma^i} \tag{2.135}$$

$$\boxed{\gamma^f = R_{21}^2 \beta^i - 2R_{22}R_{21}\alpha^i + R_{22}^2 \gamma^i} \tag{2.136}$$

The transfermatrix R can also be written as a function of the Twiss parameters and the phase Ψ up- and downstream to give their transformation by inserting the Twiss solutions of the EOM (Equations 2.119, 2.120) into equation 2.97 giving:

$$R = \begin{pmatrix} \sqrt{\frac{\beta}{\beta_0}}(\cos(\Psi) + \alpha_0 \sin(\Psi)) & \sqrt{\beta\beta_0}\sin(\Psi) \\ \frac{(\alpha_0 - \alpha)\cos(\Psi) - (1+\alpha\alpha_0)\sin(\Psi)}{\sqrt{\beta\beta_0}} & \sqrt{\frac{\beta_0}{\beta}}(\cos(\Psi) - \alpha \sin(\Psi)) \end{pmatrix} \tag{2.137}$$

In periodic structures the Twiss parameters of a closed orbit must match when transformed by the one turn transport matrix R_{1T} so we can write:

$$R_{u,1T} = \begin{pmatrix} \cos(2\pi Q_u) + \alpha_0 \sin(2\pi Q_u) & \beta_0 \sin(2\pi Q_u) \\ \gamma_0 \sin(2\pi Q_u) & \cos(2\pi Q_u) - \alpha_0 \sin(2\pi Q_u) \end{pmatrix}. \tag{2.138}$$

Initial values for the Twiss parameters can also be gained from the one turn matrix:

$$B_0 \stackrel{!}{=} R_{1T} B_0 R_{1T}^T \tag{2.139}$$

$$\to \beta_0 = \frac{-2R_{12}}{sgn(R_{12})\sqrt{4 - (Tr(R))^2}} \tag{2.140}$$

$$\to \alpha_0 = \frac{R_{11} - R_{22}}{sgn(R_{12})\sqrt{4 - (Tr(R))^2}} \tag{2.141}$$

$$\to \gamma_0 = \frac{1 + \alpha_0^2}{\beta_0} \tag{2.142}$$

2.1.12. Transformation of the radial dispersion

The dispersion D corresponds to the additional transverse offset from the orbit due to the relative momentum offset $\delta = 1$. It only occurs in the radial plane for most accelerators. Its transformation

can be written as[10]:

$$
\begin{pmatrix} D \\ D' \\ 1 \end{pmatrix}_f = \begin{pmatrix} R_{11} & R_{12} & R_{16} \\ R_{21} & R_{22} & R_{26} \\ 0 & 0 & 1 \end{pmatrix} \begin{pmatrix} D_0 \\ D'_0 \\ 1 \end{pmatrix}_i \tag{2.143}
$$

In analogy to the solution of the EOM for particles with $\delta = 1$ in Dipoles (Equation 2.81) it is usually introduced by dipoles with non zero R_{16} and R_{26}. The total offset for a particle with $\delta \neq 0$ is

$$
x(s) = x(s) + D(s)\sigma_\delta \tag{2.144}
$$

and the actual beam width with dispersion is

$$
\sigma_x(s) = \sqrt{\epsilon_x \beta_x(s) + (D(s)\sigma_\delta)^2} \tag{2.145}
$$

The periodic solution for the dispersion can be found in analogy to that of the Twiss parameters discussed in the previous section:

$$
\begin{pmatrix} D_0 \\ D'_0 \\ 1 \end{pmatrix} \overset{!}{=} R_{1T} \begin{pmatrix} D_0 \\ D'_0 \\ 1 \end{pmatrix} \tag{2.146}
$$

$$
\rightarrow D'_0 = \frac{R_{21}R_{13} + R_{23}(1 - R_{11})}{2 - R_{11} - R_{22}} \tag{2.147}
$$

$$
\rightarrow D_0 = \frac{R_{12}D'_0 + R_{13}}{1 - R_{11}} \tag{2.148}
$$

2.1.13. Momentum compaction factor

The dispersive trajectories are in general of different length than the orbit. The momentum compaction factor α_p gives the ratio of the change in path length to the corresponding relative momentum offset δ of a charged particle[10]:

$$
\frac{\Delta L}{L} = \alpha_p \frac{\Delta p}{p} = \alpha_p \sigma_\delta \tag{2.149}
$$

$$
\rightarrow \alpha_p = \frac{\Delta L}{L \sigma_\delta} \tag{2.150}
$$

In first order only dipoles contribute to this change in path length. The path length difference between the inner and outer trajectory in dipoles corresponds to that in any curve of a race track:

$$
\Delta L = \oint \left(\frac{R(s) + x_D(s)}{R(s)} - 1 \right) ds = \sigma_\delta \oint \frac{D(s)}{R(s)} ds \tag{2.151}
$$

so the momentum compaction factor can be written as

$$
\alpha_p = \frac{1}{L} \oint \frac{D(s)}{R(s)} ds. \tag{2.152}
$$

or for an isomagnetic ring with constant R:

$$
\alpha_p = \frac{1}{LR} \oint D(s) ds. \tag{2.153}
$$

For closed orbits with circumference L the momentum compaction factor can be calculated from the transformation of the particle vector by the one turn matrix [11];

$$\alpha_p = \frac{\Delta L}{L\delta} = \frac{l(s) - l_0}{L\delta} = \frac{R_{51}x_i + R_{52}x_i' + R_{56}\delta}{L\delta} = \frac{R_{56}}{L} \tag{2.154}$$

The smaller α_p gets the closer the dispersive trajectories are to one another. Additionally to the momentum compaction factor α_p gamma transition

$$\gamma_{tr} = \frac{1}{\sqrt{\alpha_p}} \tag{2.155}$$

is often introduced. The transition energy $E_{tr} = \gamma_{tr}mc^2$ corresponds to the energy when the effects of increased round time due to increased path length due to $\delta > 0$ and reduced round time due to increased speed due to $\delta > 0$ compensate one another.

2.1.14. Chromaticity

The chromaticity is defined as the change of tune due to non zero relative momentum offset δ [10]

$$\xi := \frac{\Delta Q}{\delta}. \tag{2.156}$$

As derived in [10] the known similarity and thus equality of the traces of the transformation matrices (Equation 2.138) for a small tune offset $Q = Q_0 + dQ$ and for a small quadrupole strength offset Δk can be used to derive:

$$4\pi dQ = \Delta k \beta(s)ds \tag{2.157}$$

$$\rightarrow \Delta Q = \frac{1}{4\pi}\int_{s_0}^{s_0+l} \Delta k \beta(s)ds \tag{2.158}$$

Particles with $\delta \neq 0$ undergo a different focussing strength in the quadrupoles. The change of the experienced quadrupole strength k for particles with wrong energy ($\delta \ll 1$) is

$$k(p + \Delta p) = -\frac{e}{p}\left(\frac{1}{1+\delta}\right)g \approx -\frac{e}{p}(1-\delta)g = k(p) - \Delta k(\Delta p) \tag{2.159}$$

$$\rightarrow \Delta k = -\delta\frac{e}{p}g = \delta k_0 \tag{2.160}$$

The impact of the energy dependant change in focussing strength of the quadrupoles on the number of betatron oscillations per revolution is expressed by the natural chromaticity and can be found by inserting equation 2.160 into 2.158 and the result into 2.156:

$$\xi_{nat} = -\frac{1}{4\pi}\oint k(s)\beta(s)ds \tag{2.161}$$

The total or corrected chromaticity is the sum of natural chromaticity and additional chromaticity introduced by sextupoles of strength m in dispersive sections which give an additional focussing of $k_{sext} = mD\delta$

$$\xi_{tot} = \frac{1}{4\pi}\oint [m(s)D(s) + k(s)]\beta(s)ds \tag{2.162}$$

21

2.2. Synchrotron radiation

Dedicated light sources have only one main raison d'être - to provide synchrotron radiation to their user experiments. This section will give an introduction to the fundamental physics behind the emitted synchrotron radiation by charged particles as well as an overview of the user demands on synchrotron radiation.

2.2.1. Radiated power

Synchrotron radiation is emitted when charged particles are accelerated. This complies to the fundamental rules of classical electrodynamics that give radiated power for non relativistic particles in Larmor's formulae[10,12]:

$$P_\gamma^{cgs} = \frac{2}{3}\frac{q^2}{m_0^2 c^3}\left(\frac{d\vec{p}}{dt}\right)^2 \tag{2.163}$$

$$P_\gamma^{SI} = \frac{q^2}{6\pi\epsilon_0 m_0^2 c^3}\left(\frac{d\vec{p}}{dt}\right)^2. \tag{2.164}$$

Since the power in the particles rest frame and laboratory frame must be equal, the Lorentz invariant generalisation can be found with the proper time $d\tau = dt/\gamma$ and the four-momentum p^μ of the charged particle (notation: always SI):

$$P_\gamma = \frac{q^2}{6\pi\epsilon_0 m_0^2 c^3}\left[\left(\frac{d\vec{p}}{d\tau}\right)^2 - \frac{1}{c^2}\left(\frac{dE}{d\tau}\right)^2\right]. \tag{2.165}$$

The effect can usually be neglected for non relativistic particles. Longitudinal radiation can generally be neglected for accelerating fields smaller than $2 \cdot 10^{14}$ MV/m[12]. In circular accelerators the energy change in the cavity is small compared to the momentum change in dipoles thus the radiated power (Equation 2.165) simplifies to[10]:

$$P_\gamma = \frac{q^2}{6\pi\epsilon_0 m_0^2 c^3}\left(\frac{d\vec{p}}{d\tau}\right)^2 = \frac{q^2 c\gamma^2}{6\pi\epsilon_0 E_0^2}\left(\frac{d\vec{p}}{dt}\right)^2 \qquad \text{with} \quad E_0 = m_0 c^2. \tag{2.166}$$

The momentum $\vec{p}$ changes per circumnavigation of the angle $d\phi$ by $dp = p\,d\phi$ thus with the angular velocity $\omega = \frac{d\phi}{dt}$ we can write:

$$\left(\frac{d\vec{p}}{dt}\right)^2 = p^2\omega^2 = \left.\frac{p^2 v^2}{R^2}\right|_{v\approx c} = \frac{E^2}{R^2}. \tag{2.167}$$

The radiated power goes with the particle Energy to the power of 4:

$$\boxed{P_\gamma = \frac{q^2 c}{6\pi\epsilon_0}\frac{\gamma^4}{R^2} = \frac{cC_\gamma}{2\pi}\frac{E^4}{R^2}}. \tag{2.168}$$

$$\text{with} \qquad C_\gamma = \frac{4\pi r_e}{3E_0^3} \approx 8.85 \cdot 10^{-5}\frac{m}{GeV^3}, \quad r_e = \frac{1}{4\pi\epsilon_0}\frac{e^2}{E_0} \tag{2.169}$$

It limits the feasible particle energy due to the technical limitations of power regain in the cavities. The total radiated power per revolution can be calculated by integrating the radiated power over one turn. For isomagnetic rings this corresponds to multiplying the radiated power (Equation 2.168) with

the revolution time spent in dipoles ($R \neq \infty$):

$$U = P_\gamma T_{rev} \approx P_\gamma \frac{2\pi R}{c} = C_\gamma \frac{E^4}{R} \tag{2.170}$$

2.2.2. Angular distribution

The azimuthal distribution of the emitted radiation of non relativistic particles (Equation 2.164) complies with that of a dipole antenna[12]

$$\frac{dP}{d\Omega} = \frac{q^2}{16\pi^2 \epsilon_0 m_0^2 c^3} \left(\frac{d\vec{p}}{dt}\right)^2 \sin^2 \Psi \tag{2.171}$$

and can be neglected. The angular distribution of relativistic radiating particles can be derived by Lorentz transformation of the particle's dipole radiation around the acceleration axis in the center-of-momentum frame to the laboratory frame of reference[10]. In good approximation the emitted radiation is reduced to one eighth of the peak intensity in forward direction for an opening angle of:

$$\Theta \leq \pm \frac{1}{\gamma}. \tag{2.172}$$

Due to the small opening angle the emission of synchrotron radiation does not significantly change the position or direction of the emitting particle - only the energy is decreased.

2.2.3. Spectrum and time structure

The time structure of a radiation pulse follows from the time difference Δt between the first and last observed photon. The first and last photons are observed when the inner and outer edge of the particles radiation cone with an opening angle of $\Theta = 2/\gamma$ (Equation 2.172) are in line with the observer. The time difference Δt can be calculated from the time of flight difference between the radiating particle and the first photon to the point B on the particles trajectory where the last photon is emitted[10]:

$$\Delta t = t_e - t_\gamma = \frac{2R}{c\beta\gamma} - \frac{2R\sin(1/\gamma)}{c} = \frac{2R}{c}\left(\frac{1}{\beta\gamma} - \sin(1/\gamma)\right) \tag{2.173}$$

The spectral distribution of the radiated power is given by[9]:

$$P_\gamma(\omega) = \frac{P_\gamma}{\omega_c} S\left(\frac{\omega}{\omega_c}\right) \qquad \text{with} \qquad \omega_c = \frac{3c\gamma^3}{2R}. \tag{2.174}$$

For a bending magnet the spectral function is given by integration over the modified Besselfunction:

$$S\left(\frac{\omega}{\omega_c}\right) = \frac{9\sqrt{3}}{8\pi} \frac{\omega}{\omega_c} \int_{\omega/\omega_C}^{\infty} K_{5/3}\left(\frac{\omega}{\omega_c}\right) d\left(\frac{\omega}{\omega_c}\right) \tag{2.175}$$

The critical angular frequency divides the radiated power spectrum equally according to the total radiated energy.

2.2.4. User demands

Many experiments require high flux (Equation 2.176) which gives the synchrotron radiation intensity in bandwidth of 0.1% around the required photon energy normalised to 1 Ampere of beam current. For high space-resolution measurements the transverse extent and divergence of the beam are also of importance - hence these experiments require high brightness (Equation 2.177) (flux normalised to transverse angle divergence) and brilliance (Equation 2.178) (brightness normalised to transverse beam extent):[10]

$$F = \frac{photons}{1\,second \cdot 0.1\%bandwidth \cdot ampere} \tag{2.176}$$

$$S = \frac{F}{2\pi\sigma_{x'}\sigma_{y'}} \tag{2.177}$$

$$B = \frac{S}{2\pi\sigma_x\sigma_y} = \frac{F}{4\pi^2\epsilon_x\epsilon_y} \tag{2.178}$$

For time resolved experiments the pulse duration that is directly determined by the bunch length becomes of great importance.

2.3. Emittance

The emittance of a single particle is defined by the ratio of π and the surface of the phase ellipse this particle moves on[9].

$$\epsilon_u = \sigma_u\sigma_{u'} = \frac{S_{u,u'}}{\pi} \tag{2.179}$$

In a canonical system the phase space volume must be constant according to Liouville's theorem and hence the emittance in accelerators is constant when the energy change of the beam amongst others due to cavities, radiation, induced currents and interaction with the residual gas can be neglected. In this section emittance damping and excitation effects are described and formulae for the dynamic and equilibrium emittance are derived.

2.3.1. Radiation integrals and constants

For the electron alone the emission of radiation energy dp_γ is not conservative. For one particle on a dispersive section (dipoles) the emittance is increased in the process. Namely the surface of the ellipse around the new dispersion trajectory the particle should be on after emission of energy dp_γ[10]:

$$\Delta x(s) = D(s)\frac{dp_\gamma}{p} \tag{2.180}$$

$$\Delta x'(s) = D'(s)\frac{dp_\gamma}{p} \tag{2.181}$$

Resulting in the new total emittance(Equation 2.127):

$$\epsilon_{tot} = \gamma(s)[x(s) + \Delta x(s)]^2 \tag{2.182}$$

$$+ 2\alpha(s)[x(s) + \Delta x(s)][x'(s) + \Delta x'(s)] \tag{2.183}$$

$$+ \beta(s)[x'(s) + \Delta x'(s)]^2. \tag{2.184}$$

With the contribution from the radiation of a photon:

$$\epsilon_{rad} = \left(\frac{dp_\gamma}{p}\right)^2 \left[\gamma(s)D^2(s) + 2\alpha(s)D(s)D'(s) + \beta(s)D'^2(s)\right]. \tag{2.185}$$

For describing the effect on the beam emittance the $\mathcal{H}$ function is introduced:

$$\boxed{\mathcal{H}_u(s) = \gamma_u(s)D_u^2(s) + 2\alpha_u(s)D_u(s)D_u'(s) + \beta_u(s)_u'^2(s)} \tag{2.186}$$

The effects of synchrotron radiation on the beam properties and especially the beam emittances are discussed next. Therefore the synchrotron radiation integrals[11] that can be used to describe these effects are introduced here:[11,13]

$$\mathcal{I}_1 = \oint \frac{D(s)}{R(s)} ds \tag{2.187}$$

$$\mathcal{I}_2 = \oint \frac{1}{R^2(s)} ds \tag{2.188}$$

$$\mathcal{I}_3 = \oint \frac{1}{|R^3(s)|} ds \tag{2.189}$$

$$\mathcal{I}_{4u,sbend} = \oint \frac{D_u(s)}{R^3(s)} \left[1 \pm 2R^2(s)k_u(s)\right] ds \tag{2.190}$$

$$\mathcal{I}_{4u,rbend} = \pm \oint \frac{D_u(s)}{R^3(s)} ds \tag{2.191}$$

$$\mathcal{I}_{5u} = \oint \frac{\mathcal{H}_u(s)}{R^3(s)}. \tag{2.192}$$

2.3.2. Adiabatic Damping and the normalized emittance

Adiabatic damping is not a real beam cooling effect. It occurs when particles are accelerated (in the cavities) and can be explained with Liouville's Theorem which states that the occupied six dimensional phase space volume must remain constant. For the uncoupled case Liouville's theorem also holds for each two dimensional phase surface separately[9]:

Figure 2.8.: Adiabatic Damping[7]

$$\Delta u \Delta p_u = const. \tag{2.193}$$

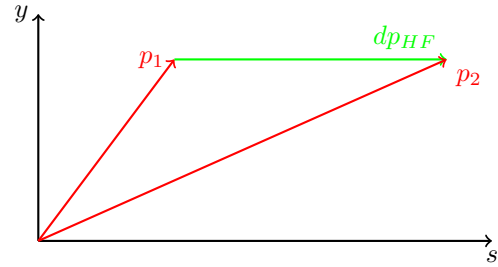In consequence the emittance, defined by the two dimensional phase space surface:

$$\epsilon_u = \Delta u \frac{\Delta p_u}{p_u} = \frac{const}{p_u} \tag{2.194}$$

is inversely proportional to the momentum or energy that is increased in the cavities. This can be described by the differential equation:

$$\boxed{\frac{\dot{\epsilon}_x(t)}{\epsilon_x(t)} = -\frac{\dot{E}(t)}{E(t)}} \tag{2.195}$$

Since adiabatic damping does not actually reduce the occupied phase space - it is often desirable to introduce the normalized emittance:

$$\epsilon^* = \epsilon\beta\gamma = \epsilon\sqrt{\gamma^2 - 1} = \epsilon\frac{p}{m_0}. \tag{2.196}$$
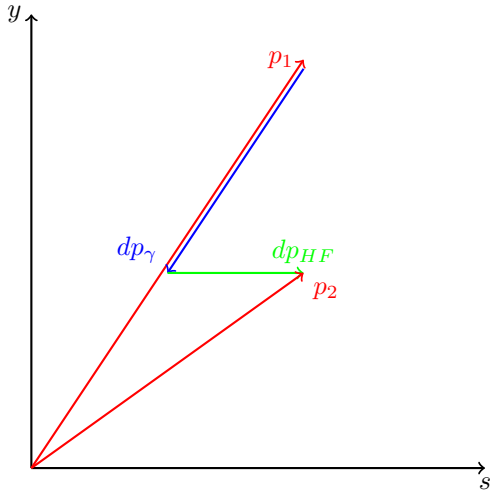
2.3.3. Radiation damping

Figure 2.9.: Radiation damping[7]

Due to the betatron oscillations synchrotron radiation is emitted transversally to the orbit. But in the cavities only longitudinal momentum is regained. Hence the amplitude of the transverse betatron oscillations and longitudinal synchrotron oscillations are damped over time as well as the corresponding emittances. This beam cooling is described by[9]:

$$\epsilon_u(t) = \epsilon_{u,0}\exp\left(-\frac{t}{\tau_u}\right) \tag{2.197}$$

$$\frac{\dot{\epsilon}_u(t)}{\epsilon_u(t)} = -\frac{1}{\tau_u} = -\alpha_u . \tag{2.198}$$

Generally the damping times τ_u can be given either for the emittance or for the oscillation amplitudes. In analogy to the adiabatic damping (Equation 2.194) for relativistic particles ($\Delta p/p = \Delta E/E$) the averaged damping per turn is found with the energy loss per turn (Equation 2.170)[9]:

$$\frac{\Delta\epsilon_u}{\epsilon_u} = -\frac{U}{E} \tag{2.199}$$

by multiplying with $1/T_{rev}$ we find

$$\frac{1}{\tau_u} = \frac{1}{T_{rev}}\frac{U}{E}. \tag{2.200}$$

In case of non zero dispersion where the photon is emitted the change of the equilibrium orbit has to be considered. This effect is given by the damping partition numbers J_u[11]:

$$J_x = 1 - \frac{\mathcal{I}_{4x}}{\mathcal{I}_2} \tag{2.201}$$

$$J_y = 1 - \frac{\mathcal{I}_{4y}}{\mathcal{I}_2} \tag{2.202}$$

$$J_s = 2 + \frac{\mathcal{I}_{4x} + \mathcal{I}_{4y}}{\mathcal{I}_2} \tag{2.203}$$

$$\rightarrow \boxed{\sum_u J_u = 4} \qquad \text{(Robinson's sum rule)}. \tag{2.204}$$

The damping decrements $\alpha_u = \tau_u^{-1}$ (with $u = x, y, s$) are then given by:

$$\boxed{\alpha_u = \frac{1}{\tau_u} = \frac{1}{T_{rev}} \frac{U}{E} J_u = \frac{cC_\gamma E^3}{2\pi R^2} J_u = \frac{2C_\alpha E^3}{R^2} J_u} \tag{2.205}$$

$$\text{with} \quad C_\alpha = \frac{cC_\gamma}{4\pi} = \frac{cr_e}{3E_0^3} \tag{2.206}$$

The damping decrements for the betatron and synchrotron oscillations as presented in [11] are retrieved by multiplying the emittance damping decrements by $\frac{1}{2}$.

2.3.4. Radiation excitation

The discrete energy loss by quantized emission of synchrotron radiation increases the emittance of the longitudinal and transverse planes when the dispersion is not zero. The sudden emission of photons ($dp_\gamma = \hbar\omega$) leads to an instantaneous change of the equilibrium orbit for the emitting electron. It then starts to oscillate around this dispersive orbit - thus increasing the emittance. The differential increase of the emittance is given by the quantum excitation q_u [14]:
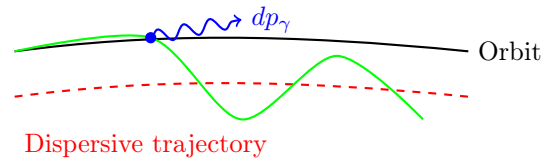
Figure 2.10.: Radiation excitation by quantized emittance of synchrotron radiation [7]

$$\boxed{\dot{\epsilon}_u(t) = q_u(t)}. \tag{2.207}$$

It can be derived from the average emitted photon energies that are found by integrating the spectral distribution (Equation 2.175) of the emitted radiation [9].

$$\langle dp_\gamma \rangle = \langle \hbar\omega \rangle = \frac{8}{15\sqrt{3}} \hbar\omega_c \tag{2.208}$$

$$\langle dp_\gamma^2 \rangle = \langle (\hbar\omega)^2 \rangle = \frac{11}{27} (\hbar\omega_c)^2 \tag{2.209}$$

The number of emitted photons per time (total photon flux) follows from the mean radiated power P_γ (Equation 2.168) divided by the mean energy of the emitted photons (Equation 2.208):

$$\dot{N}_\gamma = \frac{P_\gamma}{\langle dp_\gamma \rangle} = \frac{15\sqrt{3}}{8} \frac{P_\gamma}{\hbar\omega_c} \tag{2.210}$$

and can be used to calculate the root mean square energy radiated per time [9,11,15,16] by multiplying with (Equation 2.208) and inserting ω_c and C_γ (Equations 2.174, 2.206):

$$\dot{N}_\gamma \langle dp_\gamma^2 \rangle = \frac{55\hbar\omega_c}{24\sqrt{3}} P_\gamma = \frac{55\hbar\omega_c}{24\sqrt{3}} \frac{cC_\gamma}{2\pi} \frac{E^4}{R^2} \tag{2.211}$$

$$= \frac{55\hbar^2 c^3}{24\sqrt{3}} \alpha \frac{\gamma^7}{R^3} \quad \text{with} \quad \alpha = \frac{e^2}{4\pi\epsilon_0 \hbar} \tag{2.212}$$

$$= \frac{4C_q C_\alpha}{R^3} \gamma^2 E^5 \quad \text{with} \quad C_q = \frac{55\hbar c}{32\sqrt{3}E_0} \tag{2.213}$$

with the fine structure constant $\alpha \approx 1/137$. The additional root mean square energy deviation of the beam due to quantum excitation q_u corresponds to this radiated energy and can be calculated by integrating over one turn.

$$q_s(t) = \frac{\langle \dot{N}_\gamma \langle dp_\gamma^2 \rangle \rangle}{E^2} = \frac{1}{2CE^2} \oint \dot{N}_\gamma \langle dp_\gamma^2 \rangle \, ds \tag{2.214}$$

In the dispersive plane(s) the increase of emittance due to the increased energy spread is described by $\mathcal{H}_u$ (Equation 2.186):

$$q_u(t) = \frac{\langle \dot{N}_\gamma \langle dp_\gamma^2 \rangle \mathcal{H}_u \rangle}{E^2} = \frac{1}{2CE^2} \oint \dot{N}_\gamma \langle dp_\gamma^2 \rangle \mathcal{H}_u ds \tag{2.215}$$

Often the radius is piecewise constant greatly simplifying the integrals. The quantum excitation is then given by:

$$q_u(t) = \frac{2C_q C_\alpha}{R^2} \gamma(t)^2 E(t)^3 \frac{\mathcal{I}_{5u}}{\mathcal{I}_2} \quad \text{with} \quad u = x, y \tag{2.216}$$

$$q_s(t) = \frac{2C_q C_\alpha}{R^2} \gamma(t)^2 E(t)^3 \frac{\mathcal{I}_3}{\mathcal{I}_2} \tag{2.217}$$

2.3.5. Dynamic emittance

The differential equation describing the evolution of the emittances in an accelerator can be found by summing up the differential contributions of the adiabatic damping (Equation 2.195), the radiation damping (Equation 2.198) and the quantum excitation (Equation 2.207) [14,16].

$$\dot{\epsilon}_u(t) = q_u(t) - \left(\frac{\dot{E}(t)}{E(t)} + \alpha_u(t) \right) \epsilon_u(t) \tag{2.218}$$

2.3.6. Equilibrium emittance

The natural or equilibrium emittance is the result of an equilibrium between the damping and stimulation of the beam oscillations due to synchrotron radiation. It is determined by the lattice and reached when particles are kept in a circular accelerator for a time long against the damping time. The formula can be gained by setting the dynamic emittance to zero [16]:

$$\epsilon_{eq,u} = \frac{C_q \gamma^2(t)}{J_u} \frac{\mathcal{I}_{5u}}{\mathcal{I}_2} \tag{2.219}$$

$$\epsilon_{eq,s} = \sigma_\delta^2 = \frac{C_q \gamma^2(t)}{J_s} \frac{\mathcal{I}_3}{\mathcal{I}_2} \tag{2.220}$$

2.3.7. Fundamental lower emittance limit

The quantum excitation of the emittance due to the recoil of the synchrotron radiation that is emitted in an angle smaller than $1/\gamma$ (Equation 2.172) is an effect that can usually be neglected. It gives the fundamental lower emittance limit [11]:

$$\epsilon_{limit} = \frac{C_q}{C} \oint \frac{\beta_y(s)}{2 J_y R(s)} ds \tag{2.221}$$

and becomes relevant in case of an ideal uncoupled storage ring where the axial emittance does not damp down to zero.

2.4. Transverse emittance measurement

For normally distributed particles with no static offset of the core of the beam ($\langle u \rangle = 0$) the Σ_{beam}-matrix in each plane corresponds to [17]:

$$\Sigma_{beam}^u = \begin{pmatrix} \langle u^2 \rangle - \langle u \rangle^2 & \langle uu' \rangle - \langle u \rangle \langle u' \rangle \\ \langle u'u \rangle - \langle u' \rangle \langle u \rangle & \langle u'^2 \rangle - \langle u' \rangle^2 \end{pmatrix} = \begin{pmatrix} \langle u^2 \rangle & \langle uu' \rangle \\ \langle u'u \rangle & \langle u'^2 \rangle \end{pmatrix} \tag{2.222}$$

and the beta matrix times the emittance:

$$\Sigma_{beam}^u = \epsilon_u \begin{pmatrix} \beta_u & -\alpha_u \\ -\alpha_u & \gamma_u \end{pmatrix}. \tag{2.223}$$

The beam-Σ-matrix is transformed along the machine by $\Sigma = R\Sigma_0 R^T$ in analogy to the transformation of the beta matrix (Equation 2.133) and determines the emittance:

$$det(\Sigma_u) = \epsilon_u \sqrt{\beta_u \gamma_u - \alpha_u^2} = \epsilon_u \qquad with \qquad \sqrt{\beta_u \gamma_u - \alpha_u^2} = 1. \tag{2.224}$$

Thus the emittance can be measured by measuring the beam profile or to be more precise the two-dimensional transverse subspace of the six-dimenional phase space occupied by the ensemble of particles (the beam). Two methods are presented:

1. the measurement of the beam cross section by imaging the synchrotron radiation onto a screen from a spot where the Twiss parameters are known

2. the determination of the upstream beam matrix by measuring the downstream beam profile as a function of the quadrupole strength of a quadrupole in between whose strength is varied.

2.4.1. Synchrotron radiation imaging

Emitted synchrotron radiation from charged particles is used to measure the beam profile. The measured beam widths σ_u (Equation 2.145) are used to calculate the emittance in each plane. The dispersion and beta functions at the radiation source (spot in bend) must be known:

$$\epsilon_u = \frac{\sigma_u^2 - (D_u \sigma_\delta)^2}{\beta_u}. \tag{2.225}$$

2.4.2. Quadrupole scan technique

The initial beam matrix Σ_u^i (with $u = x, y$) represented by Twiss parameters or moments of the beam distribution is transformed by the quadrupole strength dependant transport matrix $R_u(k)$ from upstream (before quadrupole) to downstream (on screen).

$$\Sigma_u^f(k) = R_u(k)\Sigma_u^i R_u^T(k). \tag{2.226}$$

A fit of the (usually) Gaussian beam distribution function to the horizontal and vertical projection of the measured image gives the downstream beam profiles (Equation 2.145)

$$\sigma_u^f(k) = \sqrt{\epsilon_u \beta_u^f(k) + (\sigma_\delta D_u^f(k))^2} \tag{2.227}$$

as the standard values of the Gaussian distribution. They are measured as a function of the varied upstream quadrupole strength k and are determined by the energy spread σ_δ, the emittance ϵ and the k-dependant downstream beta function $\beta_u^f(k)$ and dispersion $D_u^f(k)$. Taking the negligible axial dispersion ($\epsilon \beta_y \gg (\sigma_\delta D_y)^2$) in planar accelerators into account the transformation of the upstream beta functions and the radial dispersion is (Equations 2.134, 2.143):

$$\beta_u^f(k) = R_{u_{11}}^2 \beta_u^i - 2R_{u_{11}} R_{u_{12}} \alpha_u^i + R_{u_{12}}^2 \gamma_u^i \tag{2.228}$$

$$D_x^f(k) = R_{x_{11}} D_x^i + R_{x_{12}} D_x^{'i} + R_{x_{16}} \tag{2.229}$$

Thus the squared downstream beam widths σ_u^f (Equation 2.227) can be written as a function of the initial upstream Twiss parameters and dispersion:

$$\sigma_x^f(k)^2 = \epsilon_x \left(R_{x_{11}}^2 \beta_x^i - 2R_{x_{11}} R_{x_{12}} \alpha_x^i + R_{x_{12}}^2 \gamma_x^i \right) + \sigma_\delta^2 \left(R_{x_{11}} D_x^i + R_{x_{12}} D_x^{'i} + R_{x_{16}} \right)^2 \tag{2.230}$$

$$\sigma_y^f(k)^2 = \epsilon_y \left(R_{y_{11}}^2 \beta_y^i - 2R_{y_{11}} R_{y_{12}} \alpha_y^i + R_{y_{12}}^2 \gamma_y^i \right). \tag{2.231}$$

With knowledge of the k-dependant beam transport matrix $R_u(k)$ the measured beam profiles $\sigma_u^f(k)$ could theoretically be used to determine the upstream Twiss parameters and dispersion as well as the emittance and energy spread by fitting an adequate model function to the data.

Due to the technically limited range of quadrupole strength the measurable part of the beam profile function is usually a quadratic curve. Therefore only 3 parameters can be extracted without overfitting the data. Thus in the radial plane the energy spread σ_δ and upstream dispersion functions D_x^i, $D_x^{'i}$ must be fixed so the k-dependant dispersive broadening $\sigma_\delta^2 D_x^f(k)^2$ can be subtracted from the measured beam profile $\sigma_x^f(k)^2$ before fitting.

To find an appropriate model function the k-dependance of the transport matrix is simplified: In the thin lens approximation it is assumed, that the quadrupole magnet length L is small in comparison to the focal length $f_u = \pm\frac{1}{kL}$.
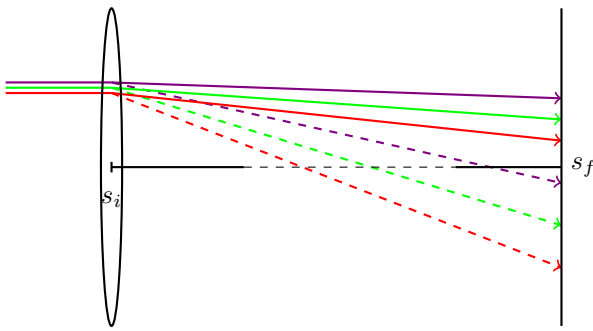
Figure 2.11.: k-dependant dispersion.[7,9,11]

With the thin-lens approximation for the quadrupole matrix:

$$Q_u = \begin{pmatrix} 1 & 0 \\ -\frac{1}{f_u} & 1 \end{pmatrix} = \begin{pmatrix} 1 & 0 \\ K & 1 \end{pmatrix} \tag{2.232}$$

with $K = \pm kL$ (negative in focussing plane) the transfer matrix resolves to:

$$R_u = \begin{pmatrix} T_{11} + KT_{12} & T_{12} \\ T_{21} + KT_{22} & T_{22} \end{pmatrix}. \tag{2.233}$$

So the transformation of the beta function according to (Equation 2.228) can be written as:

$$\beta_u^f(K) = (T_{11} + KT_{12})^2 \beta_u^i - 2(T_{11}T_{12} + KT_{12}^2)\alpha_u^i + T_{12}^2 \gamma_u^i \tag{2.234}$$

and hence giving the dispersion corrected beam width on the screen

$$\sigma_u^{*2}(k) = \sigma_u^f(k)^2 - \left(\sigma_\delta D_u^f(k)\right)^2 = \sigma_u^f(k)^2 - \sigma_\delta^2 \left(R_{x_{11}}(k)D_x^i + R_{x_{12}}(k)D_x^{'i} + R_{x_{16}}(k)\right)^2 \quad (2.235)$$

as a function of K with three unknown coefficients A, B and C:

$$\sigma_u^{*2}(K) = \epsilon_u \beta_u^f(K) \quad (2.236)$$

$$= K^2 \left[T_{12}^2 \epsilon_u \beta_u^i\right] - 2K \left[T_{12}^2 \epsilon_u \alpha_u^i - T_{11}T_{12}\epsilon_u \beta_u^i\right] + \left[T_{11}^2 \epsilon_u \beta_u^i - 2T_{11}T_{12}\epsilon_u \alpha_u^i + T_{12}^2 \epsilon_u \gamma_u^i\right] \quad (2.237)$$

$$= K^2 \left[\Sigma_{11}^i T_{12}^2\right] + 2K \left[\Sigma_{11}^i T_{11}T_{12} + \Sigma_{12}^i T_{12}^2\right] + \left[\Sigma_{11}^i T_{11}^2 + 2\Sigma_{12}^i T_{11}T_{12} + \Sigma_{22}^i T_{12}^2\right] \quad (2.238)$$

$$= K^2 [A] + 2K[B] + [C] \quad (2.239)$$

By fitting the model function (Equation 2.239) to the dispersion corrected measured data the coefficients A, B and C are determined. The beam matrix elements follow directly from these and the known matrix elements of R_u. The emittance and then the Twiss parameters follow:

$$\Sigma_{u,11}^i = \frac{A}{T_{12}^2} \qquad \rightarrow \qquad \beta_u^i = \frac{\Sigma_{u,11}^i}{\epsilon_u} \quad (2.240)$$

$$\Sigma_{u,12}^i = \frac{B - T_{11}T_{12}\Sigma_{u,11}^i}{T_{12}^2} \qquad \rightarrow \qquad \alpha_u^i = -\frac{\Sigma_{u,12}^i}{\epsilon_u} \quad (2.241)$$

$$\Sigma_{u,22}^i = \frac{1}{T_{12}^2}\left[C - T_{11}^2 \Sigma_{u,11}^i - 2T_{11}T_{12}\Sigma_{u,12}^i\right] \qquad \rightarrow \qquad \gamma_u^i = \frac{\Sigma_{u,22}^i}{\epsilon_u} \quad (2.242)$$

$$\epsilon_u = \sqrt{det(\Sigma_u^i)} = \sqrt{\Sigma_{u,11}^i \Sigma_{u,22}^i - (\Sigma_{u,12}^i)^2} \quad (2.243)$$

2.5. Transverse emittance exchange with skew quadrupoles

The matrix R_θ rotates the beam by an angle θ around the tangent to the orbit clockwise in flight direction for $\theta > 0$. It can be derived by transforming the well known rotation matrix $R_{zz'}(\theta)$ to accelerator coordinates (Equation 2.95)

$$R_\theta = T_A^S \begin{pmatrix} \cos\theta & \sin\theta & 0 & 0 & 0 & 0 \\ -\sin\theta & \cos\theta & 0 & 0 & 0 & 0 \\ 0 & 0 & 1 & 0 & 0 & 0 \\ 0 & 0 & 0 & \cos\theta & \sin\theta & 0 \\ 0 & 0 & 0 & -\sin\theta & \cos\theta & 0 \\ 0 & 0 & 0 & 0 & 0 & 1 \end{pmatrix} T_A^{S\,T} = \begin{pmatrix} \cos\theta & 0 & \sin\theta & 0 & 0 & 0 \\ 0 & \cos\theta & 0 & \sin\theta & 0 & 0 \\ -\sin\theta & 0 & \cos\theta & 0 & 0 & 0 \\ 0 & -\sin\theta & 0 & \cos\theta & 0 & 0 \\ 0 & 0 & 0 & 0 & 1 & 0 \\ 0 & 0 & 0 & 0 & 0 & 1 \end{pmatrix}$$
$$(2.244)$$

When transforming the six dimensional Σ_{beam}-matrix of an uncoupled beam

$$\Sigma = \begin{pmatrix} \beta_x \epsilon_x & -\alpha_x \epsilon_x & 0 & 0 & \sigma_{15} & \sigma_{16} \\ -\alpha_x \epsilon_x & \gamma_x \epsilon_x & 0 & 0 & \sigma_{25} & \sigma_{26} \\ 0 & 0 & \beta_y \epsilon_y & -\alpha_x \epsilon_y & 0 & 0 \\ 0 & 0 & -\alpha_y \epsilon_y & \gamma_x \epsilon_y & 0 & 0 \\ \sigma_{15} & \sigma_{25} & 0 & 0 & \sigma_{55} & \sigma_{56} \\ \sigma_{16} & \sigma_{26} & 0 & 0 & \sigma_{56} & \sigma_{66} \end{pmatrix} \quad (2.245)$$

with $|R_\theta|$ for $\theta = \pi/2$

$$R_{\pi/2} = \begin{pmatrix} 0 & 0 & 1 & 0 & 0 & 0 \\ 0 & 0 & 0 & 1 & 0 & 0 \\ -1 & 0 & 0 & 0 & 0 & 0 \\ 0 & -1 & 0 & 0 & 0 & 0 \\ 0 & 0 & 0 & 0 & 1 & 0 \\ 0 & 0 & 0 & 0 & 0 & 1 \end{pmatrix} \tag{2.246}$$

the transverse emittances and Twiss parameters are completely exchanged:

$$|R_{\pi/2}|\Sigma|R_{\pi/2}|^T = \begin{pmatrix} \beta_y\epsilon_y & -\alpha_y\epsilon_y & 0 & 0 & 0 & 0 \\ -\alpha_y\epsilon_y & \gamma_y\epsilon_y & 0 & 0 & 0 & 0 \\ 0 & 0 & \beta_x\epsilon_x & -\alpha_x\epsilon_x & \sigma_{15} & \sigma_{16} \\ 0 & 0 & -\alpha_x\epsilon_x & \gamma_x\epsilon_x & \sigma_{25} & \sigma_{26} \\ 0 & 0 & \sigma_{15} & \sigma_{25} & \sigma_{55} & \sigma_{56} \\ 0 & 0 & \sigma_{16} & \sigma_{26} & \sigma_{56} & \sigma_{66} \end{pmatrix} \tag{2.247}$$

Therefore any optics with $|R_{\pi/2}|$ as the total transfer matrix will exchange the transverse emittances and Twiss parameters. Obviously this cannot be achieved with any of the elements introduced so far. Skew quadrupoles are rotated quadrupoles. Their transport matrix is

$$R_{skew} = R_\Theta^T R_Q R_\Theta \tag{2.248}$$

Since the rotation of a drift section has no effect and

$$R_\Theta R_\Theta^T = \mathbb{1}_{6x6} \tag{2.249}$$

holds the rotation of each element of a sequence of drifts and quadrupoles is equal to the rotation of the complete sequence. Thus an emittance exchange section can be found by searching for a combination of drifts and quadrupoles that when rotated by an angle θ gives the desired transport matrix (Equation 2.246). Often the quadrupoles are rotated by 45° - halfway to a simple change of the focussing plane at 90°. Under the condition that all quadrupole will be rotated by 45° a section of drifts and quadrupoles will exchange the transverse emittances if the unrotated section has the total transport matrix:

$$R_{sec} \stackrel{!}{=} R_{\pm\pi/4}^T |R_{\pi/2}| R_{\pm\pi/4} = \begin{pmatrix} \mp 1 & 0 & 0 & 0 & 0 & 0 \\ 0 & \mp 1 & 0 & 0 & 0 & 0 \\ 0 & 0 & \pm 1 & 0 & 0 & 0 \\ 0 & 0 & 0 & \pm 1 & 0 & 0 \\ 0 & 0 & 0 & 0 & 1 & 0 \\ 0 & 0 & 0 & 0 & 0 & 1 \end{pmatrix} \tag{2.250}$$

With the weaker requirement for R_{sec} that only $R_x = -R_y$ the emittances are also exchanged but not the Twiss functions. Such a section (Equation 2.250) can be numerically found as will be shown in section 6.2. A classical textbook example for emittance exchange sections with skew quadrupoles is the Brown Rotator with 6 equidistant quadrupoles all of which are operated at the same strength[9].

3. BESSY II

The history of BESSY II - now Germanys top third generation light source began 1978 in Berlin-Wilmersdorf. There BESSY I the predecessor of BESSY II was commissioned on the 19th December 1981. It was Germanys first dedicated Synchrotron radiation source and used for radiation metrology, X-ray lithography and fundamental research. BESSY I had 800 MeV beam energy with 50 nmrad emittance. 1985 COSY - a compact synchrotron for industrial use based on two superconducting 180° bending magnets was built at the same facility and mainly intended for chip production with X-ray lithography. Plans for the main successor BESSY II were short handedly changed after the reunion of Germany and the fall of the Wall in Berlin. Berlin-Adlershof was soon recognized as a better site for such a big research facility. After breaking ground in Berlin-Adlershof on the 4th of July 1994 BESSY II was finally comissioned 1998 and has been a success up to today. 1999 BESSY I was shut down to lay all focus on its successor BESSY II. 2000 the remaining parts were disassembled and sent to Jordan for SESAME - Synchrotron-light for Experimental Science and Applications in the Middle East. This chapter provides an overview of the momentary status of BESSY II as well as a brief introduction to the next upgrade project.

3.1. Overview

The electrons at BESSY II are extracted from a DC cathode at 90 keV and accelerated to 50 MeV in the linac structure operating at 3 GHz. The injection line transports the bunches to the booster synchrotron where they are accelerated to 1.7 GeV in 33 ms. They reach the storage ring via the transfer line that crosses the radiation protection wall of the booster. The maximum beam current of 300 mA in the storage ring is reached by successive injection of electrons from the injector system. The booster operates at a repetition rate of 10 Hz. Usually over 3 mA beam current are reached in the booster. However the injection rate is administratively reduced to 1 Hz making the filling up of the storage ring possible in 100 s. Since fall 2012 BESSY II is operated in top-up mode where the storage ring is kept at 300 mA by continuously injecting current with open beam shutters.

Figure 3.1.: Overview of BESSY II[7,18]

This has many advantages including constant thermal load on the optical devices (gratings etc.) of the beam lines and constant brightness for the user experiments. But there are also
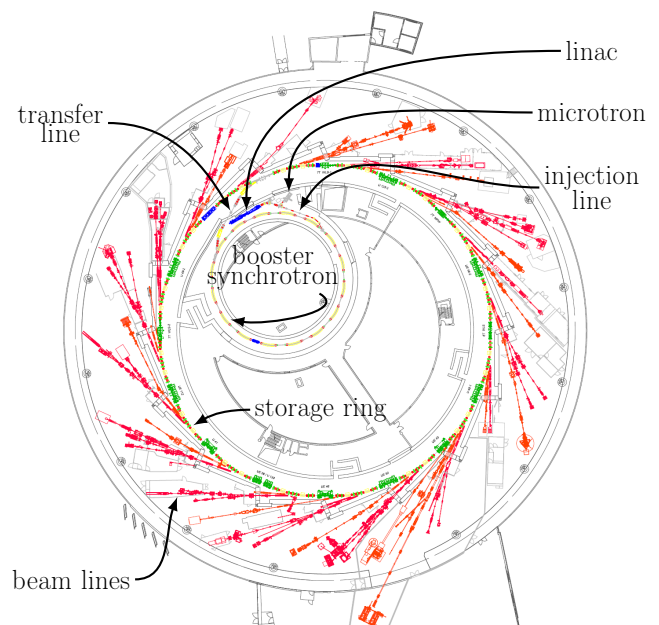
disadvantages like user visible beam movement due to the injection process and higher radiation safety requirements. Due to these the injection efficiency has become a critical parameter. It is permanently and redundantly monitored and must stay over 90 % in 4 h average and over 60 % in every shot otherwise the injector system is automatically deactivated. Before top-up the storage ring was operated in decay mode. On the user side there are 43 available beam lines delivering the light from the bending magnets, undulators and wigglers to some 50 user experiments[19]. The available photon energy ranges from THz to the hard x-ray domain.

3.2. Linac

Quantity	Unit	SPM	LPM
Energy	MeV	50.9	50.6
Charge	nC	0.34	2.15
Energy spread	%	0.24	0.2
Radial emittance	nm rad	376	119
Axial emittance	nm rad	318	104

Table 3.1.: Measured parameters delivered by the BESSY II linac[20]

The linac (Figure 3.2) is the preinjector for BESSY II. It was manufactured by Thales* and installed in 2011 as successor of the 50 MeV microtron which is now in standby and ready to take over in case of linac failures. Advantages of the linac (Table 3.1) are the online configurable operation modes providing flexible bunch population patterns to synchronously fill the storage ring and the 30 times higher[21] single bunch currents/filling rates making time consuming knock out procedures obsolete. The short pulse mode (SPM) delivers 1 to 5 bunches of 1 ns each at 0.34 nC. In long pulse mode (LPM) 40 to 200 ns long bunch trains with a total charge of 2 nC are delivered.

A 90 kV triode gun with an EIMAC Y-845 cathode with 0.5 cm^2 emissive area delivers the electrons. These non-relativistic electrons are guided by short shielded focussing solenoids through two prebunching cavities running at 499.625 (PB1) and 2997.75 MHz (PB2) to the standing wave buncher driven by 5 MW of RF power. Here the electrons are accelerated to 15 MeV with an average field of 18 MV/m. The standing wave buncher is surrounded by two shielded solenoids providing a 0.2 Tesla magnetic field for beam focusing. A solenoid between the buncher and the accelerating structure focusses the beam sufficiently for the travelling wave accelerating structure to operate without external focussing. Here the beam energy reaches the required 50 MeV and the bunch length is compressed to some 20 ps.
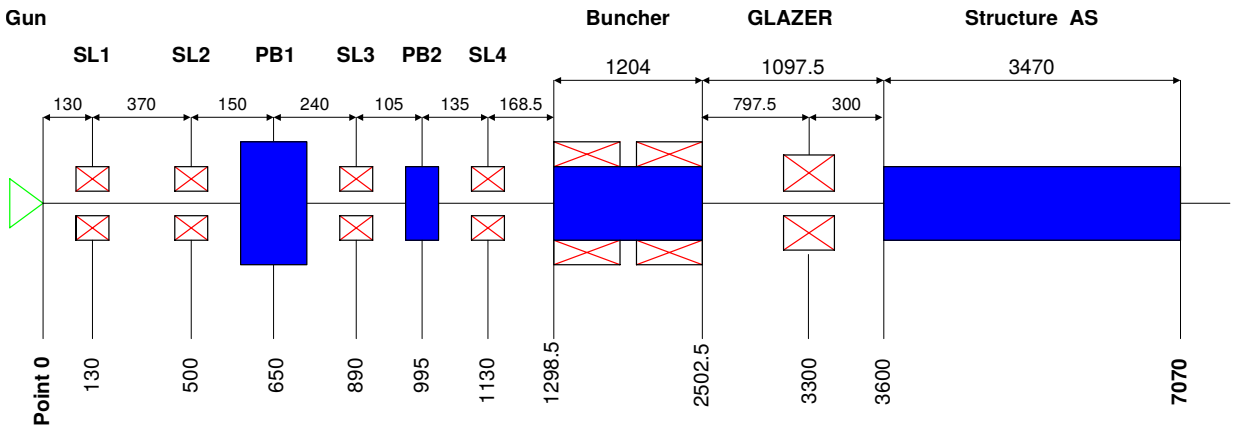

Figure 3.2.: Layout scheme of the linac[22]

---

*A multinational defense, security, aerospace and transportation company better known for the Queen Elizabeth-class aircraft carriers it builds for the British royal navy.

3.3. Injection line

The Bessy II injection line was originally designed for the microtron injector. The linac was set up inside the booster bunker between microtron and transferline (Figure 3.1). Therefore a linac injection line consisting of a two dipole chicane and 7 quadrupoles (Figure 3.3) that ends in the second bending magnet B1P2I of the original microtron injection line was installed. The original injection line is made up of a 2 dipole chicane at the beginning and end and 16 quadrupoles. By switching B1P2I on and off it is possible to toggle between the microtron and linac. Due to the historic development of the injection line it is now rather long and complex. It was optimized by hand for high tolerance against energy fluctuations from the linac. Setting the first two dipole chicane achromatic is essential. Switching off 9 of the 23 quadrupoles proved to not only simplify the injection line and eliminate potential sources of error but also results in high injected beam currents into the booster.

Below the results of a first simulation approach of the linear beam optics of the BESSY II injection line are presented. The drift and magnet lengths were taken from technical drawings and the magnetic fields from the BESSY II database. The polarity of the quadrupoles was checked with a mobile hall sensor.
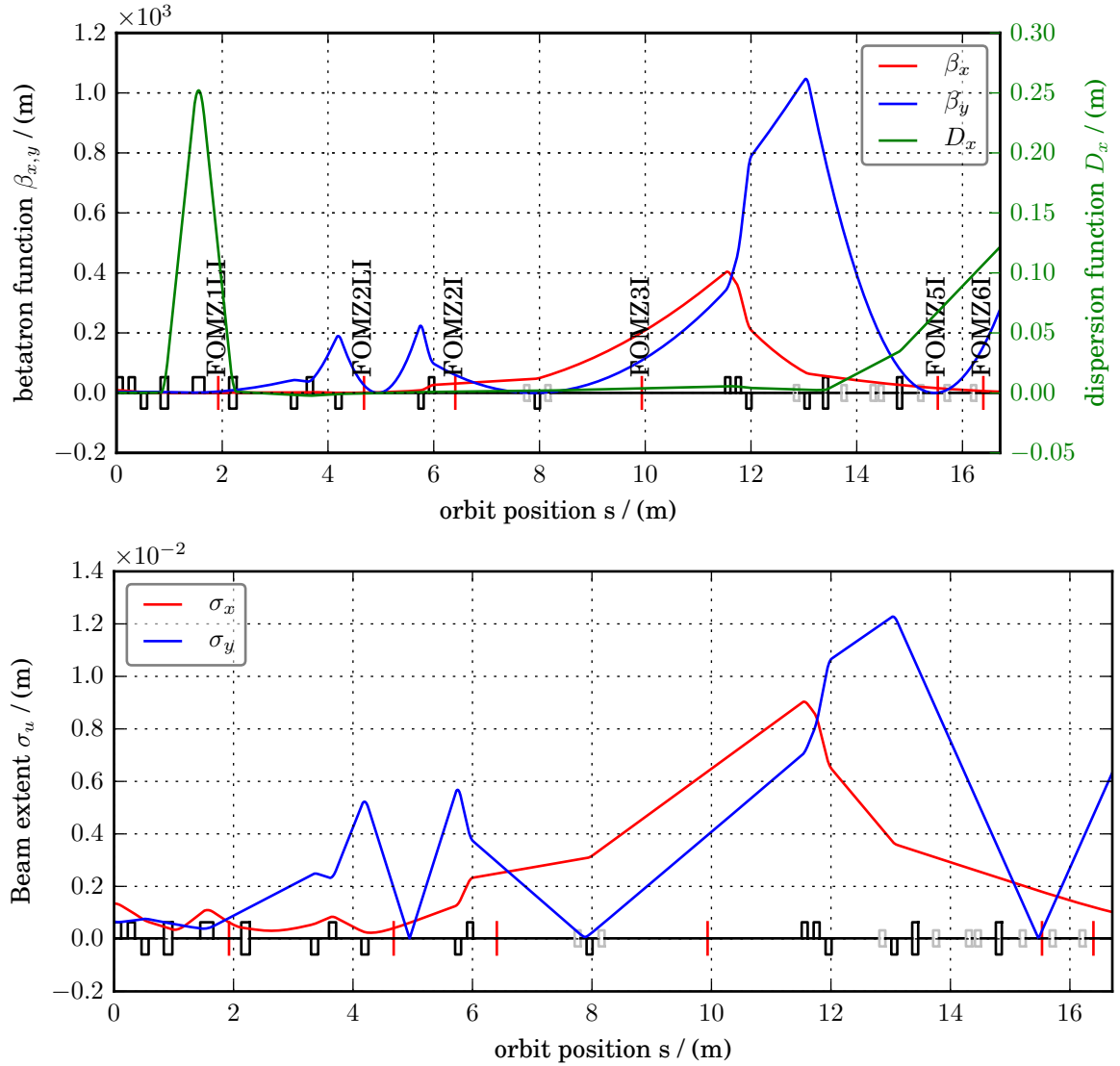

Figure 3.3.: Betatron and dispersion functions and beam extents over the BESSY II injection line[1,2]

The simulations were made with ACCPY[1] as all further simulations unless stated otherwise. The credibility of results from ACCPY was cross-checked with other well known simulation programs and results from measurements (Appendix B). The simulation results for the injection line show maximum beta functions of 404 m in the radial and 1047 m in the axial plane. This would correspond to some 9 mm and 12 mm 1-σ beam extents in a vacuum chamber of 25 mm. The beam parameters coming from the linac are based on quadrupole scan measurements that seem to give reliable values for the emittance

$$\epsilon_x = 202 \, \text{nmrad} \tag{3.1}$$

$$\epsilon_y = 144 \, \text{nmrad} \tag{3.2}$$

but not so for the twiss parameters. A small change in the initial Twiss parameters can change the maximum oscillation amplitudes by a factor of 10 giving beam extents greater than the given aperture. This may be part of the cause for problems with the injection efficiency into the booster. These problems often arise after manual optimization of the linac for maximum current output.

3.4. Booster Synchrotron

Circumference	96m
RF-frequency	500MHz
Revolutiontime	320ns
Extraction energy	1.72GeV
Injection energy	50MeV
Tunes Q_x/Q_y	5.9/3.4
Nat. chromaticities	-9.6/-4.5
Damping times $\tau_x/\tau_y/\tau_s$	5.1/4.7/2.3ms
Energyspread @E_{ext}	$5.6 \cdot 10^{-4}$

Table 3.2.: Main parameters of the BESSY II booster[1,23,24]

The fast ramping BESSY II booster accelerates the electrons from roughly 50 MeV to 1.7 GeV. An overview of the main booster parameters can be found in (Table 3.6)). The booster magnets are powered by three independant 10 Hz white circuits[25] for the dipoles, radial focusing quadrupoles and axial focusing quadrupoles. They keep the load on the main power supply below 500 kW instead of ± 5 MW with direct powering and are designed to keep the tune shift $\delta_{Q_{x,y}}$ below 5 %. With the momentary cabling of the individual white circuits to the quadrupole families these are synchronously ramped up and down at identical current in each family. Thus there exist only 2 knobs for changing the quadrupole strengths - one for the focussing and one for the defocussing quadrupole family.

The booster is in total made up of 8 equal cells (16 when only speaking of the linear optics). The arrangement of the magnets in each half cell is in accordance with a standard FODO (focus - drift - defocus - drift) lattice:
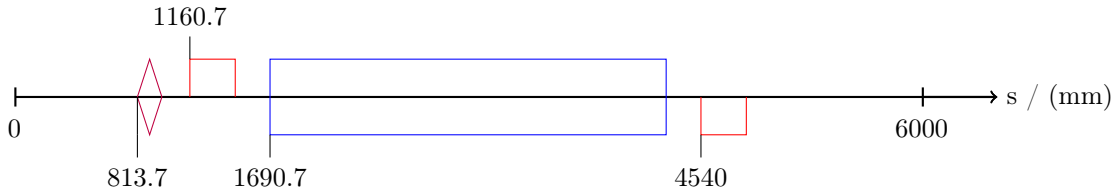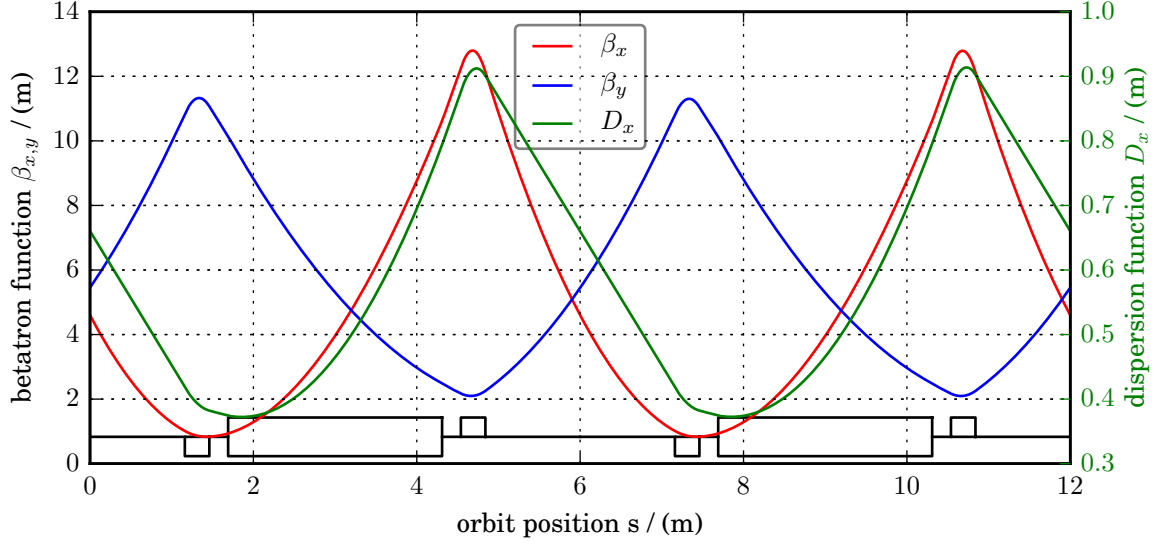

Figure 3.4.: Positions of magnets in BESSY II booster unit cell[7]

The geometry of the magnets (Table B.3) is taken from the BESSY II database. The orbit length of the dipoles is calculated from the constraint that they must in total sum up to a complete circle:

$$2\pi \cdot R \overset{!}{=} N_{sections} \cdot L_{Dipol} \qquad \Rightarrow \qquad L_{Dipol} = \frac{2\pi \cdot R}{16} \approx 2619.3mm \qquad (3.3)$$

The following simulations of the linear optics of the BESSY II booster are based on these numbers (Table B.3) and lattice files from P. Kuske and G. Wüstefeld. The results are in good agreement with tune measurements from 2013[26]. Further simulations on the dynamics of the booster ramp are presented in section 5.

Radial parameters	Axial parameters	Longitudinal parameters
$\beta_{x,max} = 12.799\ m$	$\beta_{y,max} = 11.3283\ m$	$E = 1.72e + 09\ eV$
$\beta_{x,min} = 0.830743\ m$	$\beta_{y,min} = 2.09474\ m$	$\gamma_{lorentz} = 3366.96$
$\alpha_{x,max} = 4.10121$	$\alpha_{y,max} = 2.23783$	$\alpha_p = 0.0330461$
$\alpha_{x,min} = -3.7153$	$\alpha_{y,min} = -2.78909$	$\eta_{slip} = 0.033046$
$\gamma_{x,max} = 1.4679$	$\gamma_{x,max} = 0.81019$	$\gamma_{tr} = 5.50098$
$\gamma_{x,min} = 0.0781313$	$\gamma_{x,min} = 0.0882747$	$Q_s = 0.0187657$
$D_{x,max} = 0.913824\ m$	$Q_y = 3.37727$	$J_s = 2.0757$
$D_{x,min} = 0.372254\ m$	$\xi_{y,nat} = -4.54111$	$\sigma_\delta = 5.601469e - 02\ \%$
$D'_{x,max} = 0.363766$	$J_y = 1$	$\sigma_\tau = 5.02721e - 11\ s$
$D'_{x,min} = -0.208604$	$\epsilon_y = 1.78495e - 13\ \pi m \cdot rad$	$\sigma_s = 0.0150712\ m$
$Q_x = 5.9045$	$\tau_y = 4.744933e - 03s$	$\tau_s = 2.285946e - 03\ s$
$\xi_{x,nat} = -9.64699$		$E_{loss} = 116078\ eV$
$J_x = 0.924302$		$P_{rad} = 580.389\ W$
$\epsilon_x = 7.31856e - 08\ \pi m \cdot rad$		$E_{crit} = 1693.81\ eV$
$\tau_x = 5.133533e - 03\ s$		$\lambda_{crit} = 7.31984e - 10\ m$

Figure 3.5.: Betatron and dispersion functions over half a unit cell of the BESSY II booster and some parameters from the linear optics simulation[1,2]

3.5. Transfer line

The transfer line transports the electron beam from the booster through the radiation protection wall to the storage ring. Since the planning of top-up mode the focus on the transfer line and especially on its influence on the injection efficiency into the storage ring has risen. Viewing screens were exchanged for novel beam size monitors and collimators[27] opening the possibility to trim the beam in the transfer line before injection into the storage ring. Hence raising the efficiency of the injection process itself. These modifications turned out not to be required and will probably be exchanged for diagnostic devices again as the optics of the transfer line are not yet fully understood.
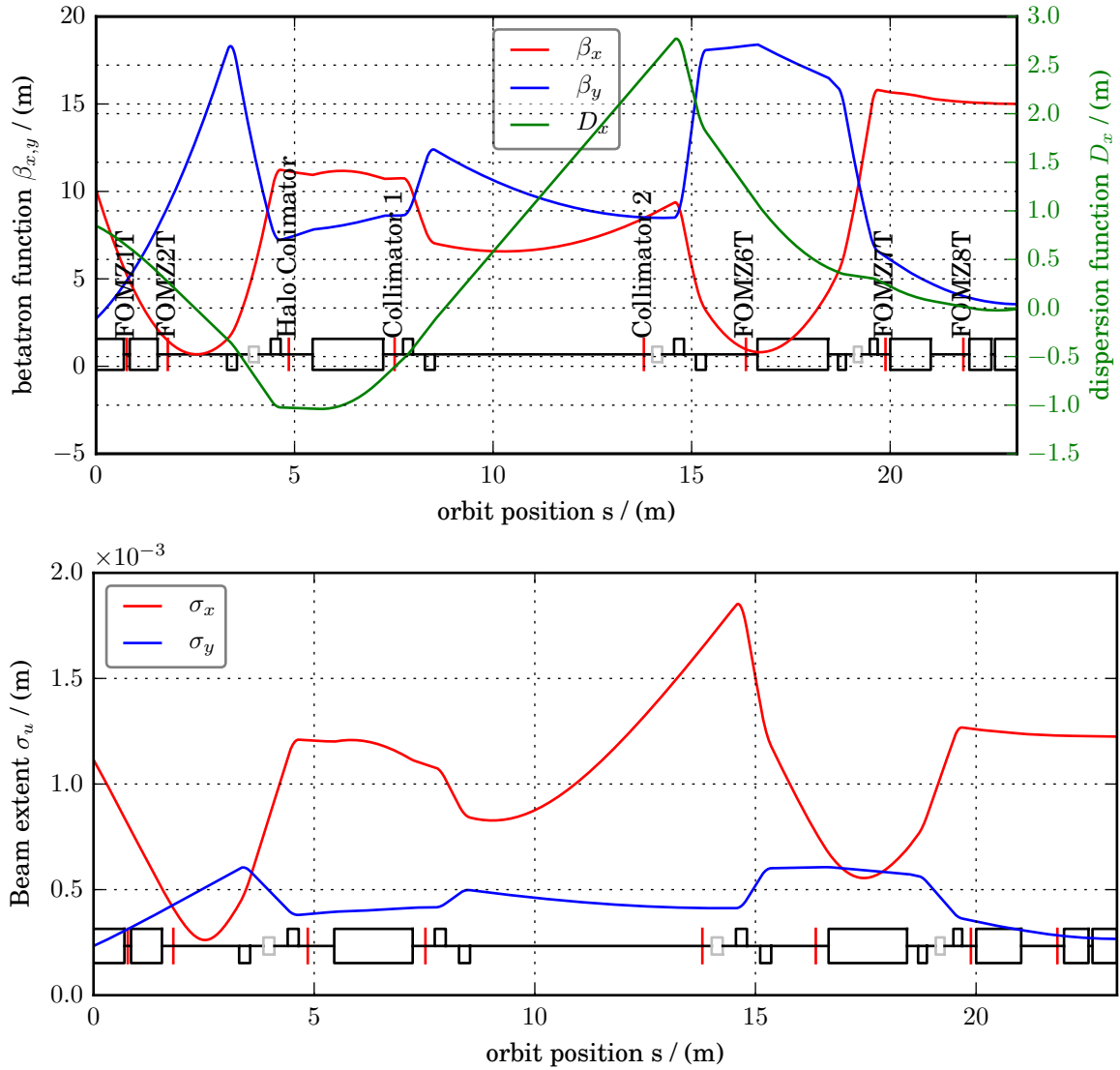
3.5.1. Designed and desired transfer line optics

Figure 3.6.: Betatron and dispersion functions and beam extents over the BESSY II transfer line[1,2]

The beam matrices in the booster and storage ring are well known and validated amongst others by measurements of the tunes, chromaticities and LOCO (Linear optics from closed orbits[28]) measurements. The desired optics of the transfer line (Figure 3.6) was designed to match the beam

matrices of the booster and storage ring while realising preferably zero dispersion for the injection into the storage ring. Furthermore betatron oscillations of amplitude smaller than 20m were achieved. The parameters for the simulation of the linear optics are taken from the lattice files from P. Kuske and G. Wüstefeld.

3.5.2. Possibly actual transfer line optics

It was called into question if the momentary quadrupole setting actually matches the design gradients. An inquiry at DANFYSIK brought the original magnet field measurement report of the transfer line magnets from after manufacturing up to light. The report includes tables with measured currents and corresponding field gradients for every quadrupole magnet of the transfer line. The data showed no significant differences between individual quadrupoles. Therefore the mean values for the short and long quadrupoles are analysed:
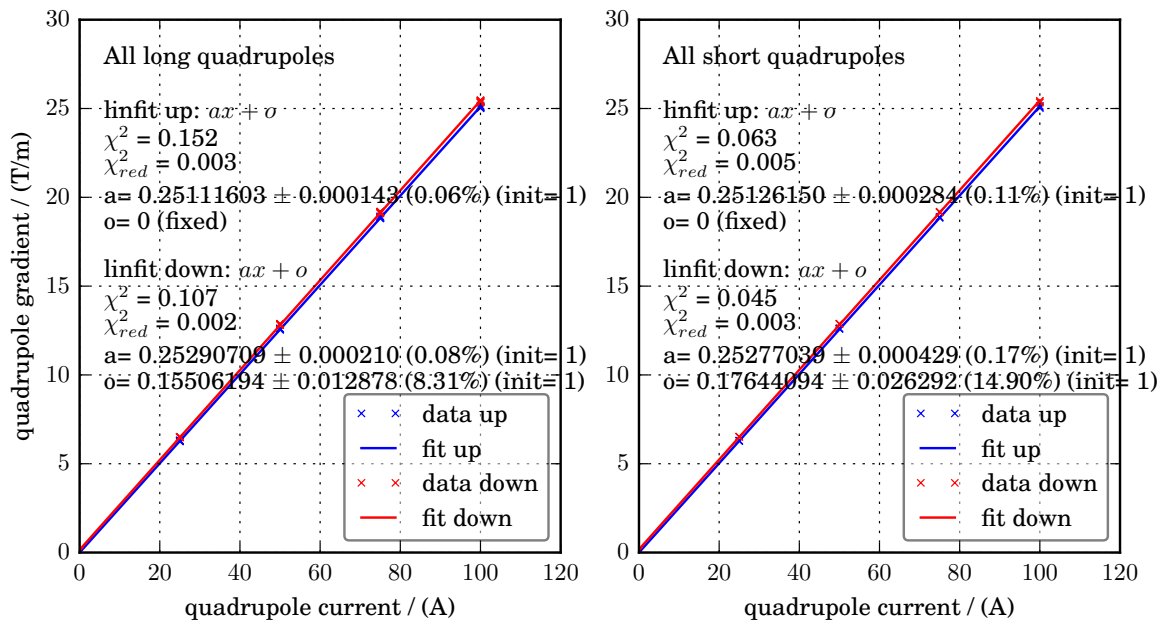

Figure 3.7.: Quadrupole gradients over current according to measurements from manufacturer DAN-FYSIK [2,5,29]

The results show that hysteresis effects are in the order of 1% and are hence neglected further on. The obtained gradient to quadrupole strength conversion factors from the linear fit assuming a beam rigidity of $R(1.72 GeV) = 5.7373$ show significant deviations from the ones used for the design optics (Figure 3.6):

Quadrupole length	BESSY II Database	DANFYSIK
0.25 m	0.06834325	0.043769
0.2 m	0.055562	0.043794

Table 3.3.: Current to gradient conversion factors. [24,29]

The obtained results (Figure 3.8) do not coincide with the stored values from the BESSY II database. The optics simulation using the set quadrupole currents and the new current to field

gradient conversion functions shows a highly undesirable optics with over $2\,\mathrm{m}$ dispersion at injection and up to $80\,\mathrm{m}$ of betatron amplitude. The $1-\sigma$ beam extents stay below $3\,\mathrm{mm}$ - hence this optic cannot be ruled out per se.
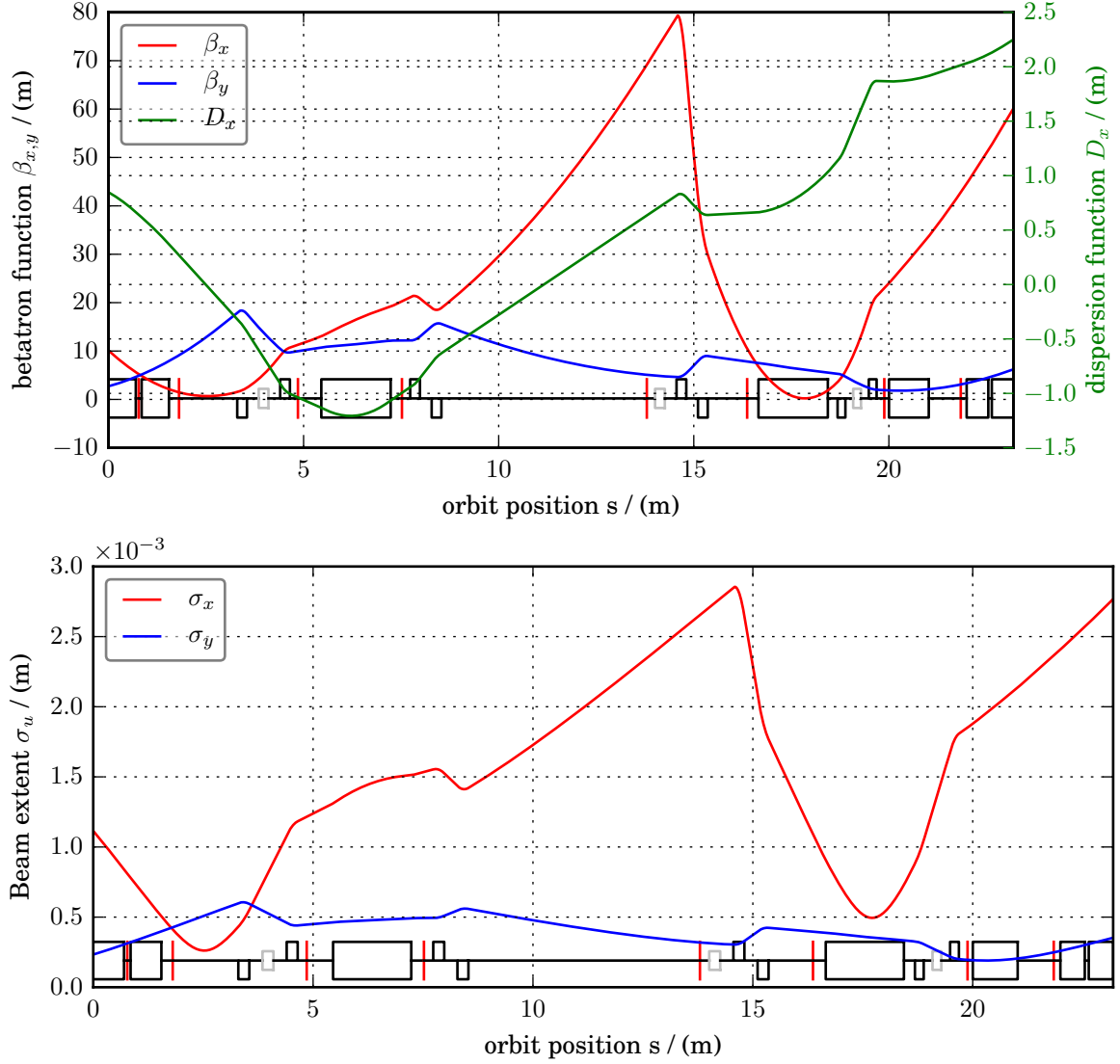

Figure 3.8.: Betatron and dispersion functions and beam extents over the BESSY II transfer line [1,2]

3.5.3. Measurement of dispersive trajectories

To further evaluate the actual optics of the transfer line reliable measurements of the beam parameters at as many spots as possible are required. As the quadrupole scan results only seem reliable concerning the measured emittances (chapter 4) the energy dependant radial displacement of the beam at all available transfer line screens was measured. The beam energy was varied by changing the extraction timing of the booster. Simultaneously the radial beam position was measured on a FOM. A Labview software designed to read out and analyse the FOM camera data was used to extract the radial beam position from a gaussian fit to the horizontal projection of the image data. The observed linear dependence of the radial displacement from the relative energy deviation corresponds to the linear dependence (Equation 2.144) of the radial particle offset from the dispersion.
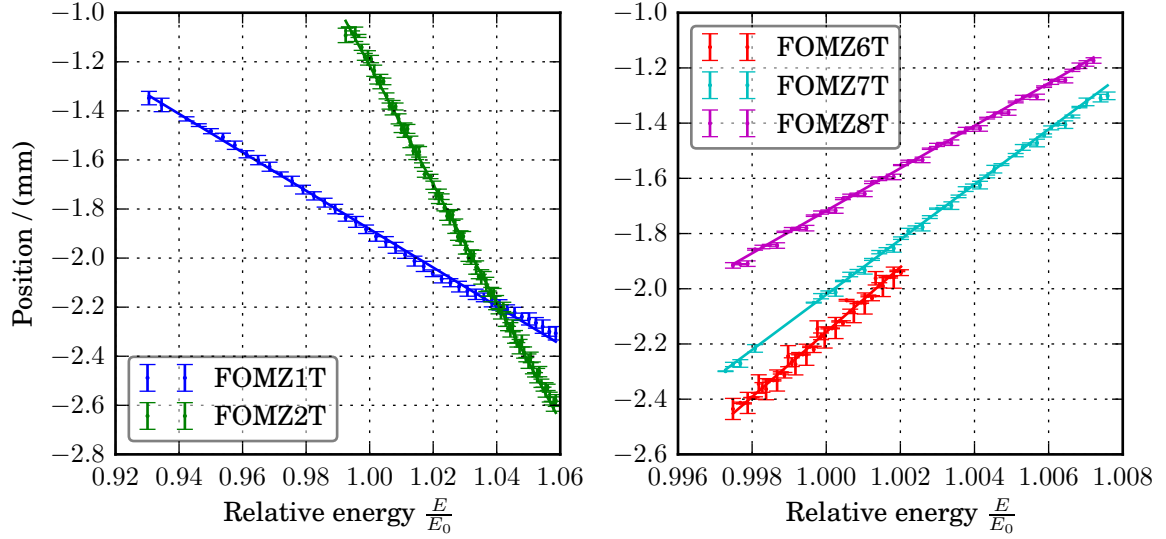
Figure 3.9.: Measurements of radial displacement as a function of extraction energy [2,5]

The linearity of the measured data gives confidence in the reliability of the obtained fit parameters. The visible terracing of the measured values is due to inconvenient variation of the extraction timing in not exact multiples of the revolution time $T_{rev} = 320 \, \text{ns}$. Nevertheless the fit errors indicate good accordance with the linear model function. The dispersion at each FOM depends on the dispersion functions at the beginning of the transfer line and the R_{16}-element of the transport matrix (Equation 2.143) to that screen:

$y = ax + b$	a/(nm)	b/(nm)
FOMZ1T	-78.269 ± 0.632	59.449 ± 0.623
FOMZ2T	-241.473 ± 0.447	229.314 ± 0.447
FOMZ6T	1174.523 ± 3.126	-1196.090 ± 3.123
FOMZ7T	998.679 ± 1.896	-1018.895 ± 1.898
FOMZ8T	769.875 ± 2.018	-787.049 ± 2.022

Table 3.4.: Retrieved parameters from the linear fits [2,5]

$$D(s) = R_{11}D(0) + R_{12}D'(0) + R_{16} \tag{3.4}$$

$$\rightarrow R_{16} = D(s) - R_{11}D(0) - R_{12}D'(0). \tag{3.5}$$

Hence the measured radial beam displacement can be written as:

$$x(s) = R_{11}x(0) + R_{12}x'(0) + R_{16}\delta \tag{3.6}$$

$$= R_{11}x(0) + R_{12}x'(0) + [D(s) - R_{11}D(0) - R_{12}D'(0)]\delta \tag{3.7}$$

The fit functions provide the possibility to compare simulated dispersive trajectories from both optics with measured ones. The following illustrations show points at the screen positions obtained from the measured functions for the energy dependant radial displacement of the beam for a set of given relative Energy offsets δ. These are compared to the corresponding dispersive particle trajectories from linear optics particle tracking simulations based on both optics taking the energy dependant beam rigidity into account. The condition of zero positional and angular displacement at the beginning of the transfer line is used.
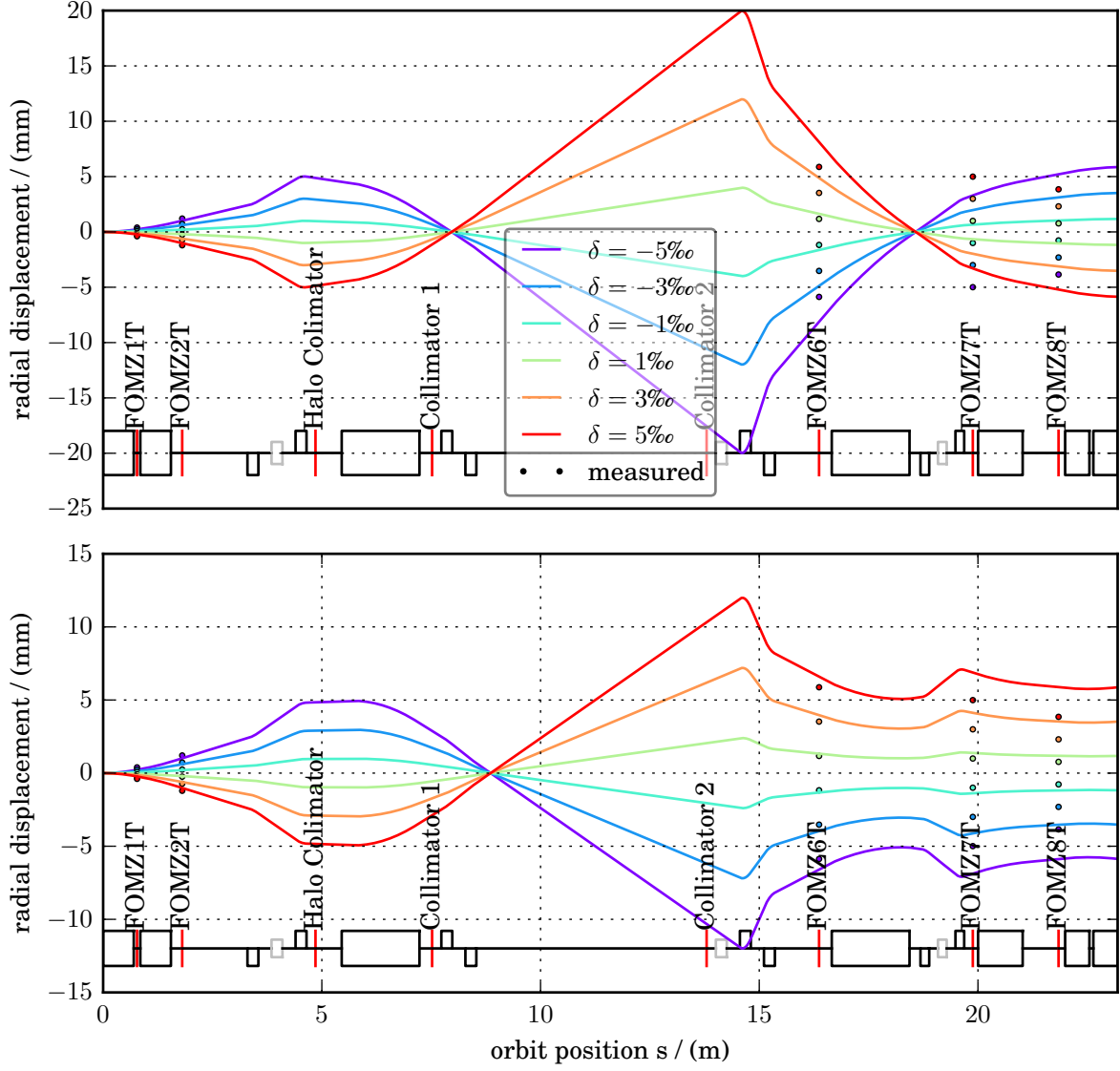
Figure 3.10.: Comparison of measurement and simulation of the radial displacement at different extraction energies for the design optics (upper) and suspected optics (lower) [1,2]

It catches the eye that the design optics trajectories cross before "FOMZ7T" while the measured points do not show this characteristic. The simulation based on the suspected optics that calculates the field gradients from the actual set currents and the new current to field gradient conversion factors is in acceptable accordance with the measured points. The offsets of some $3\,\mathrm{mm}$ seem plausible when taking neglected effects like gradients in the septum magnets and the energy dependant extraction bump in the booster into account. Even more so due to the unclear correlation between the set booster extraction timing and the timings of all elements involved in the extraction process (bumper-, kicker- and septa magnets). It is clear that a small deviation of the beam positions and angles at the beginning of the transfer line ($x(0)$ and $x'(0)$) also has great impact on the measured and simulated radial displacements (Equation 3.7).

In summary the measured data definitely further questions the old conversion factors but does not give enough confidence to validate the new ones due to the mentioned error sources.
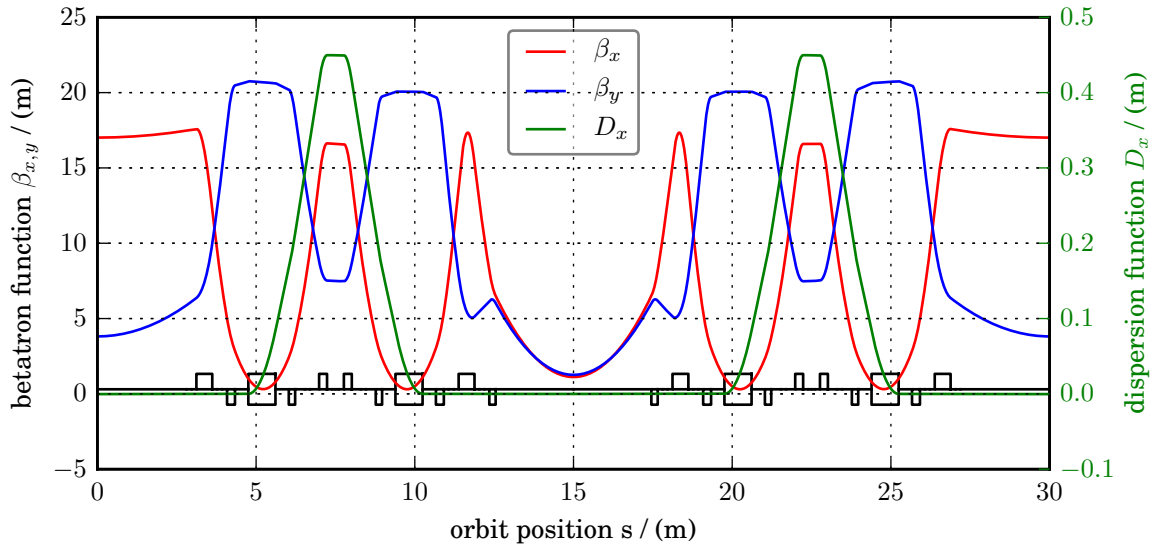
3.6. Storage ring

Circumference	240m
RF-frequency	500MHz
Revolutiontime	800ns
Beam current I_{DC}	300mA
Tunes Q_x/Q_y	17.8/6.6
Nat. chromaticities	-52.8/-21.4
Damping times $\tau_x/\tau_y/\tau_s$	7.8/7.7/3.9ms
Energyspread @E_{ext}	$7 \cdot 10^{-4}$

Table 3.5.: Storage ring parameters[1,24]

The BESSY II storage ring linear optics consists of 16 double bend achromat sections each composed of 2 dipoles surrounded by quadrupole doublets and with a triplet in between. It represents a typical 3rd generation synchrotron light source. 14 of the 16 straight sections are equipped with insertion devices (undulators, wigglers). These are special magnet structures providing synchrotron radiation brightness several orders of magnitude higher than that of bending magnets. The synchrotron radiation emitted in these has impact on the radiation integrals but are neglected in my simulations. Thus the obtained radiation integral dependant results are questionable.

Radial parameters

$\beta_{x,max} = 17.5852 \; m$
$\beta_{x,min} = 0.304174 \; m$
$\alpha_{x,max} = 11.2282$
$\alpha_{x,min} = -11.2282$
$\gamma_{x,max} = 9.15969$
$\gamma_{x,min} = 0.056866$
$D_{x,max} = 0.449659 \; m$
$D_{x,min} = -0.000325011 \; m$
$D'_{x,max} = 0.268651$
$D'_{x,min} = -0.268651$
$Q_x = 17.825$
$\xi_{x,nat} = -52.7822$
$J_x = 0.993582$
$\epsilon_x = 5.30752e - 09 \; \pi m \cdot rad$
$\tau_x = 7.794306e - 03 \; s$

Axial parameters

$\beta_{y,max} = 20.7603 \; m$
$\beta_{y,min} = 1.26085 \; m$
$\alpha_{y,max} = 11.1978$
$\alpha_{y,min} = -11.1978$
$\gamma_{x,max} = 7.58567$
$\gamma_{x,min} = 0.0486314$
$Q_y = 6.60556$
$\xi_{y,nat} = -21.161$
$J_y = 1$
$\epsilon_y = 5.28603e - 13 \; \pi m \cdot rad$
$\tau_y = 7.744279e - 03s$

Longitudinal parameters

$E = 1.72e + 09 \; eV$
$\gamma_{lorentz} = 3366.96$
$\alpha_p = 0.000731697$
$\eta_{slip} = 0.000731609$
$\gamma_{tr} = 36.9687$
$Q_s = 0.00637276$
$J_s = 2.00642$
$\sigma_\delta = 7.051279e - 02 \; \%$
$\sigma_\tau = 1.03141e - 11 \; s$
$\sigma_s = 0.00309208 \; m$
$\tau_s = 3.859753e - 03 \; s$
$E_{loss} = 177803 \; eV$
$P_{rad} = 53340.8 \; W$
$E_{crit} = 2594.5 \; eV$
$\lambda_{crit} = 4.77873e - 10 \; m$

Figure 3.11.: Betatron and dispersion functions over half a unit cell of the BESSY II storage ring and some parameters from the linear optics simulation[1,2]
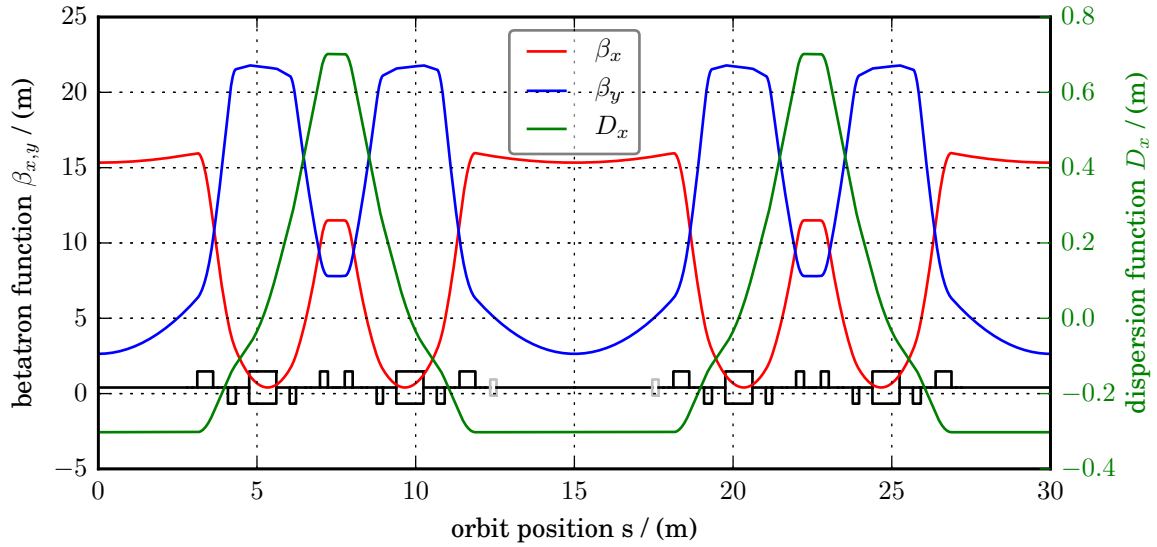
3.6.1. Operation modes

Figure 3.12.: Betatron and dispersion functions over half a unit cell of the BESSY II storage ring low-α optics[1,2]

The BESSY II storage ring has 400 available buckets with 15 ps bunch length using the standard optics and 3 ps in low-α (Figure 3.12) mode where the optics is tuned to minimize the momentum compaction factor. The injection efficiency in low-α mode does not meet the radiation safety requirements. Hence it is operated in decay mode.

Independently of the optics the filling pattern can be chosen to provide:

- high average brightness by equally filling many bunches

- the possibility of bunch separation with a rotating wheel (MHz-chopper[30]) by leaving dark gaps of 200 ns

- bunches for energy modulation with ultrashort laser pulses in the undulator retrieving synchrotron light with the lasers time stucture[31]

- special bunches for **P**ulse **P**icking by **R**esonant **E**xcitation (PPRE)[32]

The filling pattern is usually composed of many of the required special bunches mentioned above providing light for many different user demands. In single bunch mode only one of the 400 buckets is filled with a purity (ratio of electrons in desired bucket to those in others) in the order of 10^4. In accordance with the revolution time of 800 ns the single bunch mode represents a special tool for some time-resolved experiments.

In the standard user mode a hybrid filling mode is implemented to simultaneously provide multi- and single bunches for standard and time resolved experiments. In the hybrid filling mode 300 of the 400 15 ns buckets are filled with 0.88 mA each and additionally special single bunches are located in and around the filling gap. Since July 2015 a new hybrid filling mode including a 3 mA PPRE bunch 84 ns after the chopper bunch in the dark gap and 4 4 mA slicing bunches for ultra fast experiments at the femtoslicing facility is established.
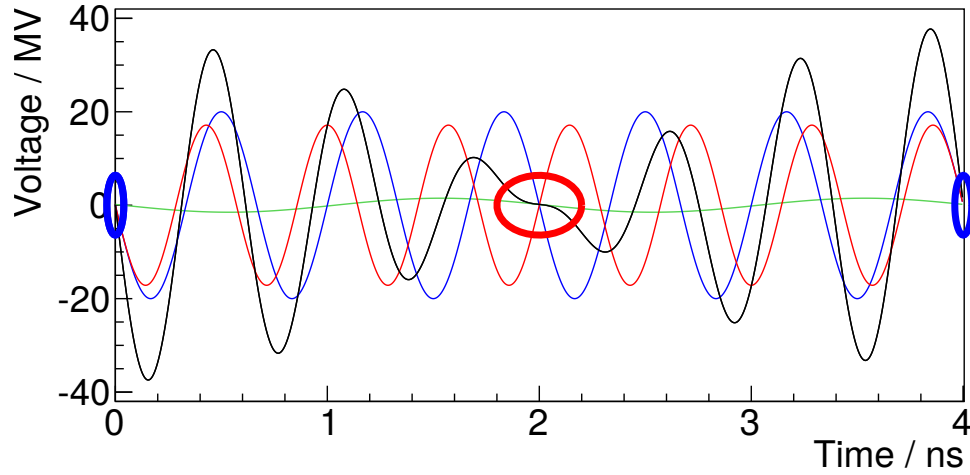
3.7. BESSY VSR

Figure 3.13.: Interaction of the individual cavity voltages (green 500 MHz, blue 1.5 GHz and red 1.75 GHz) to create long and short pulses in accordance with the sum voltage (black line) [33]

The next major upgrade planned for BESSY II is the installation of 2 additional superconducting semi-passive RF cavities operating at 1.5 and 1.75 GHz in the storage ring enabling **V**ariable bunch lengths in the **S**torage **R**ing (VSR). The equilibrium bunch length $\sigma_{s,0}$ in storage rings in the zero current limit is determined by the equilibrium energy spread (Equation 2.220) and given by [11,34]:

σ_s/ps	standard	low-alpha
BESSY II	15	3
BESSY VSR	1.7	0.3

Table 3.6.: Bunch lengths σ_s in the BESSY II storage ring at standard and low-alpha optics settings [33]

$$\sigma_{s,0} = \frac{|\eta|}{2\pi f_s}\sigma_\delta = \sigma_\delta \sqrt{\frac{E\alpha_p}{f_{rev}e\dot{U}}} \qquad \text{with} \quad \eta = \alpha_p - \frac{1}{\gamma^2} \tag{3.8}$$

where η is the phase slip factor. Therefore the beat wave of the different cavity voltages (Figure 3.13) with areas of high (blue ellipse) and low (red ellipse) gradients ($\dot{U}$) will facilitate simultaneous long (15 ps) and short (3 ps) bunches in the storage ring. Thus clearing the path for state of the art time and space resolved user experiments in standard operation mode. This upgrade will raise the requirements for the injector system as top-up injection into the short bunches will not meet the radiation safety requirements with the present injector system as now in low-α mode. Thus the great challenge of BESSY VSR concerning the injector system is to reach the required injection efficiency into short bunches. Therefore the transverse and longitudinal (bunch length) emittance must be optimized for the injection process. Further details on the challenges and prospects of BESSY VSR are presented in the technical design report [33].

4. Measurement of the transverse emittance in the injection chain

4.1. Methods

Two methods and the corresponding formulae for measuring the beam emittance where derived in section 2.4. Here experimental details on these methods and results from measurements will be presented.

4.1.1. Synchrotron radiation

Basically it is possible to either directly measure the angular spread of the emitted synchrotron radiation or to image it and measure the cross section. This technique can be used to measure the transverse beam emittance in a booster over the ramp without disturbing the beam. It requires enough photons in the energy domain of the band gap of silicon which most sensors are made of and good knowledge of the beam parameters at the observed position. The wavelength of the light visible for the used CCD ranges from 300 to 1100 nm[35,36]. Saturation effects and dependencies between the incident photon flux on the CCD and the measured beam widths falsify results and have to be prevented by going to short exposure times and low currents from the linac - preferably single bunch mode. The BESSY II booster synchrotron radiation becomes visible for the installed imaging system starting from about 200 MeV beam energy. As the axial plane is dispersion free its results can be considered superior since there is no energy spread dependant broadening of the beam. The energy dependant energy spread itself varies over the ramp and is taken from the simulation results presented in chapter 5 to obtain the radial emittance from the measurements.

4.1.2. Quadrupole Scan

In contrast to the parasitic measurement of synchrotron radiation the quadrupole scan technique uses a beam destroying fluorescent screen (FOM). The intercepting screen is usually made of or coated with a fluorescent material (light emitted in the range of ns after excitation) and possibly also phosphorescent material (light emitted in the range of μs after excitation) material[37]. Coating the screen with a thin conductive layer is required to avoid charging the screen. It is inserted into the beam path at 45° making a direct observation of the beam distribution possible with a camera. The camera captures the luminescence on the screen and digitizes the image. At BESSY II the image data can be analysed in real time with a Labview software providing amongst others horizontal and vertical beam widths from Gaussian fits to the corresponding projections of the image. The results are made available over the **E**xperimental **P**hysics and **I**ndustrial **C**ontrol **S**ystem (EPICS). Fitting the measured data to the mathematically derived exact function did not converge for all tested optimisation algorithms from Matlab and Scipy. Therefore the equations derived from the thin lens approximation for the quadrupole (Equation 2.239) are fitted to the squared measured beam

widths in order to determine the emittance and upstream Twiss functions. As said (Equation 2.230) the k-dependant dispersive broadening $\left(\sigma_\delta D_x^f(k)\right)^2$ must be calculated with fixed upstream values for the dispersion functions (from the linear optics simulation) and subtracted from the measured beam widths. The following quadrupole scan simulations compare the results of the full linear beam transformation, the linear beam transformation using the thin lens approximation for the quadrupole transfer matrix with and without the upstream dispersion of 0.5 m.
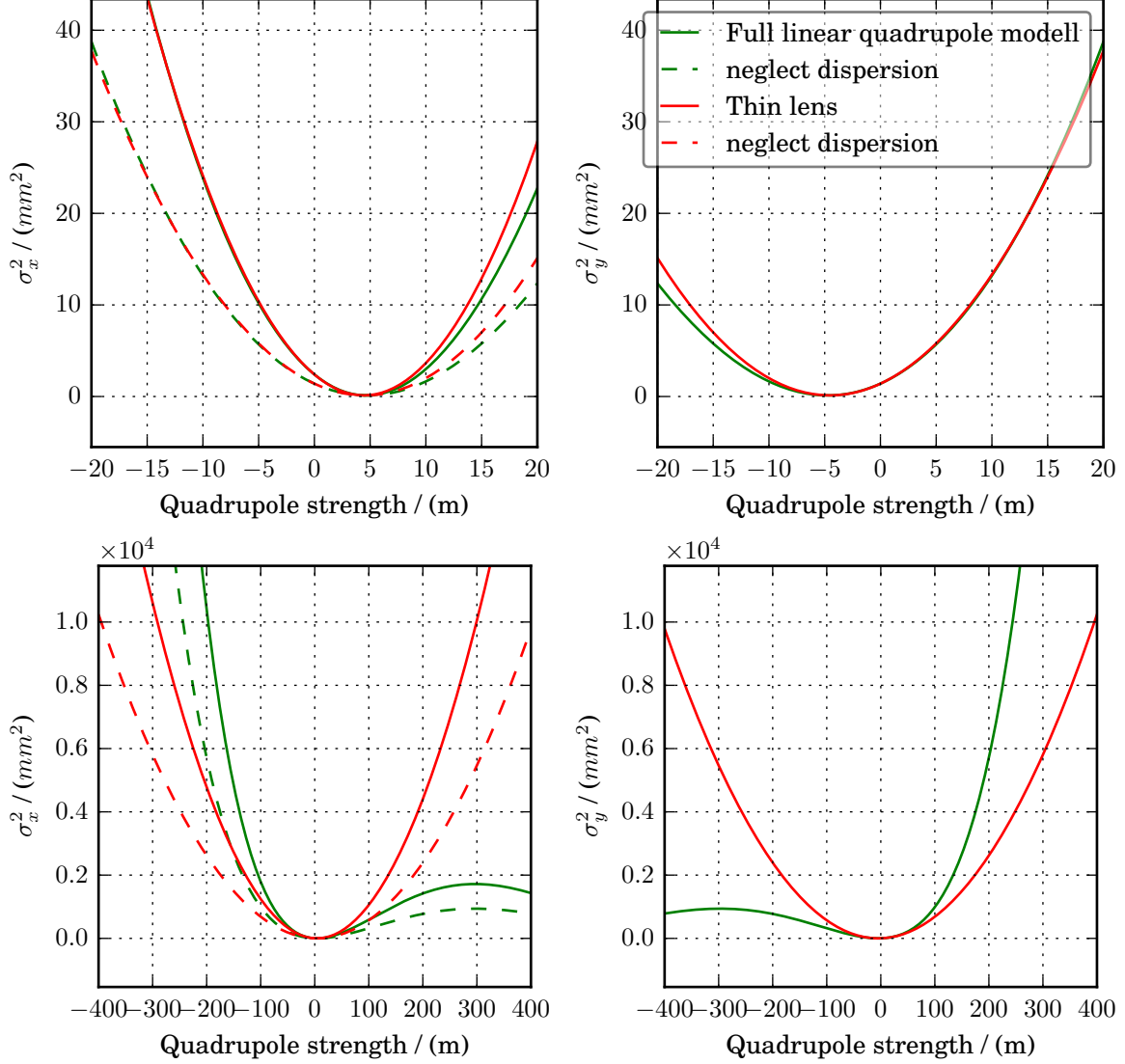

Figure 4.1.: Simulations of quadrupole scan ($L_q = 0.119$ m and $L_{drift} = 1.8$ m) using thin lens approximation and full linear model showing the parabolic behaviour in the measurable region allowing only for fit of three parameters. ($\epsilon_u = 200\,\pi$nmrad, $\beta_u^i = 6$ m, $\alpha_u^i = -0.1$, $E = 52$ MeV, $\sigma_{\delta,u} = 1$, $D_u^i = 1$ m and $D_u'^i = -0.1$ rad)[1,2]

The results show (also tested for other common upstream beam parameters) that the thin lens approximation is a valid replacement for the actual quadrupole transfer matrix at usual quadrupole strengths for these measurements. The dispersion however can not be neglected as the measurements in the transfer line (4.4) will confirm.

As with the imaging of synchrotron radiation also the direct measurement of the beam widths on FOMS proved to be technically falsified from saturation effects and non linearity between the

measured beam extents and the intensity on the FOM. Therefore all measurements are made in single bunch mode and at low current output from the linac. When taking data the summed intensity in the region of interest (ROI) on the image and the beam current are monitored and data accompanied by fluctuations is trimmed.

4.2. Injection line

The emittance in the injection line can be measured with a beam destructive method like a quadrupole scan. The advantage of this technique in dispersion free sections is that due to direct beam width measurement no knowledge of the beam parameters is required. A measurement with synchrotron light is technically out of question in the injection line due to the low electron energy of about 50MeV. As only straight ahead of the linac certainty of measuring a dispersion free beam is given all trustworthy measurements are made before the first double bend on FOMZ3LI directly in front of the linacs beam dump. The results of measurements between the third quadrupole Q3PLI in the axial plane and the first quadrupole Q1PLI in the radial plane on FOMZ3LI straight ahead of the linac showed the best results. The gained emittances are in fair agreement with those measured 2013 by Stepan Wesch: $\epsilon_x^* = 20.73 \pm 0.29 \, \pi \mu\mathrm{m} \cdot \mathrm{rad}$, $\epsilon_y^* = 14.79 \pm 0.13 \, \pi \mu\mathrm{m} \cdot \mathrm{rad}$ [38].
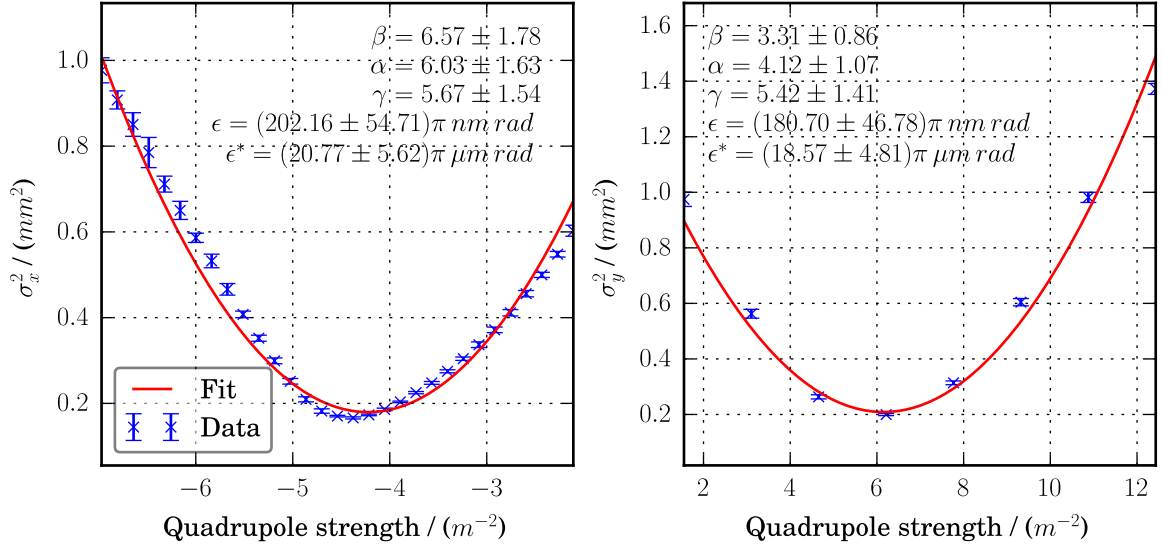

Figure 4.2.: Dispersion free ($\sigma_\delta = 2.4$) quadrupole scan straight ahead of linac. With Q1PLI (left side, $L_{drift} = 2.29775\,\mathrm{m}$) and Q3PLI (right side, $L_{drift} = 2.29775\,\mathrm{m}$) on FOMZ3LI[1,2]

The high uncertainties of the determined Twiss parameters come from error propagation of the obtained errors of the fit parameters for $y = ax^2 + bx + c$ according to their formulae (Equations 2.240, 2.240, 2.240):

$$\sigma_{\Sigma_{11}} = \frac{1}{T_{12}^2}\sigma_a \tag{4.1}$$

$$\sigma_{\Sigma_{12}} = \frac{1}{T_{12}^2}\sqrt{\sigma_b^2 + \left(-T_{11}T_{12}\sigma_{\Sigma_{11}}\right)^2} \tag{4.2}$$

$$\sigma_{\Sigma_{22}} = \frac{1}{T_{12}^2}\sqrt{\sigma_c^2 + \left(-T_{11}^2\sigma_{\Sigma_{11}}\right)^2 + \left(-2T_{11}T_{12}\sigma_{\Sigma_{12}}\right)^2} \tag{4.3}$$

$$\sigma_\epsilon = \frac{1}{2\epsilon}\sqrt{\left(\Sigma_{22}\sigma_{\Sigma_{11}}\right)^2 + \left(\Sigma_{11}\sigma_{\Sigma_{22}}\right)^2 + \left(-2\Sigma_{12}\sigma_{\Sigma_{12}}\right)^2} \tag{4.4}$$

$$\sigma_\beta = \frac{1}{\epsilon} \sqrt{\sigma^2_{\Sigma_{11}} + \left(-\frac{\Sigma_{11}}{\epsilon}\sigma_\epsilon\right)^2} \tag{4.5}$$

$$\sigma_\alpha = \frac{1}{\epsilon} \sqrt{\sigma^2_{\Sigma_{12}} + \left(\frac{\Sigma_{12}}{\epsilon}\sigma_\epsilon\right)^2} \tag{4.6}$$

$$\sigma_\gamma = \frac{1}{\epsilon} \sqrt{\sigma^2_{\Sigma_{22}} + \left(-\frac{\Sigma_{22}}{\epsilon}\sigma_\epsilon\right)^2}. \tag{4.7}$$

The obtained Twiss parameters strongly depend on the set fit region and should be treated with care. Further on the image of the beam on the FOM clearly showed several overlapping Gaussian distributions (bunches) at certain quadrupole strength settings increasing the skeptism over the obtained values.
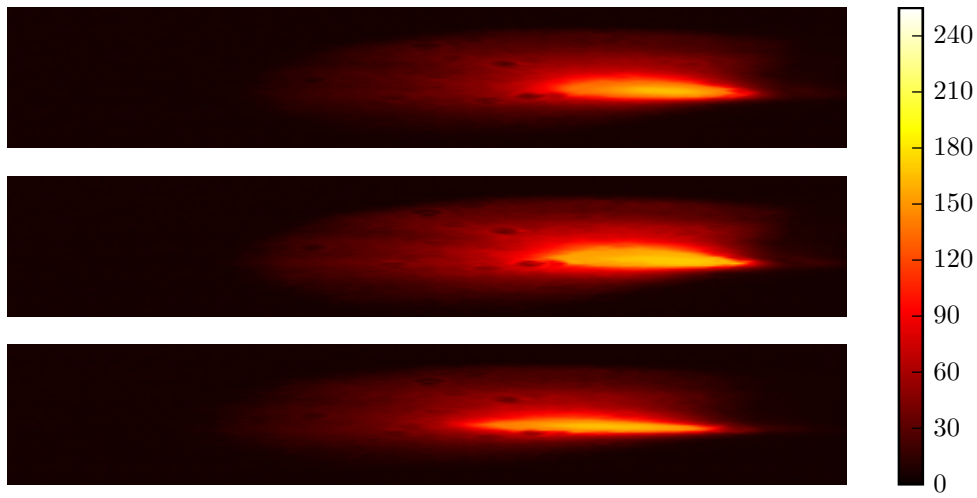
4.3. Booster

Figure 4.3.: Intensitymaps of the booster synchrotron radiation from a dipole 11, 44 and 78 ms after injection. [2]
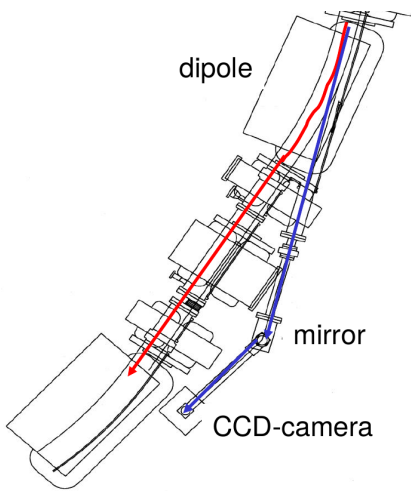

Figure 4.4.: Engineering drawing showing setup of booster camera

The emittance over the booster ramp must be measured with a non-invasive method - in this case the synchrotron radiation of a dipole is imaged onto a camera chip (Figure 4.4). First qualitative measurements show the expected increase of the horizontal and decrease of the axial beam width at high energies (Figure 4.3). The expected graph for the radial beam width corresponding to the radial emittance should be dominated by damping processes at low energies after injection. Later the radiation excitation should kick in and the emittance up which should then before extraction be on the order of the equilibrium emittance. The axial emittance is expected to only show damping but not to the fundamental lower limit as the booster is not coupling free. The same Labview program used to analyse the image data for the quadrupole scans is also used with the synchrotron radiation.

To calculate the actual beam width from the measured widths of the synchrotron light spot on the camera sensor the imaging properties of the optical path from the vacuum chamber to the camera are required. Due to the undocumented camera setup and the use of a zoom camera lens only a very rough estimation of the imaging factor could be made from the available information (Figure 4.5).
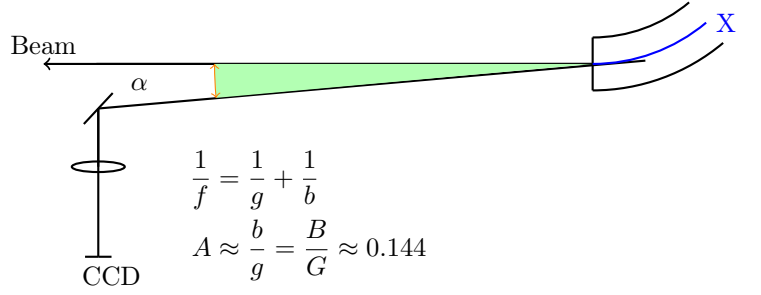
$$\frac{1}{f} = \frac{1}{g} + \frac{1}{b}$$

$$A \approx \frac{b}{g} = \frac{B}{G} \approx 0.144$$

Figure 4.5.: Simple estimation of the imaging factor. [7]

To calculate the emittance from the beam widths the Twiss parameters and dispersion at the observation point on the orbit are required. The linear booster optics (Figure 3.5) is trusted as it show good consistence with measured tunes and chromaticities [26]. The deviation of the transverse tunes over the ramp is in the order of some % (Figure 4.6).
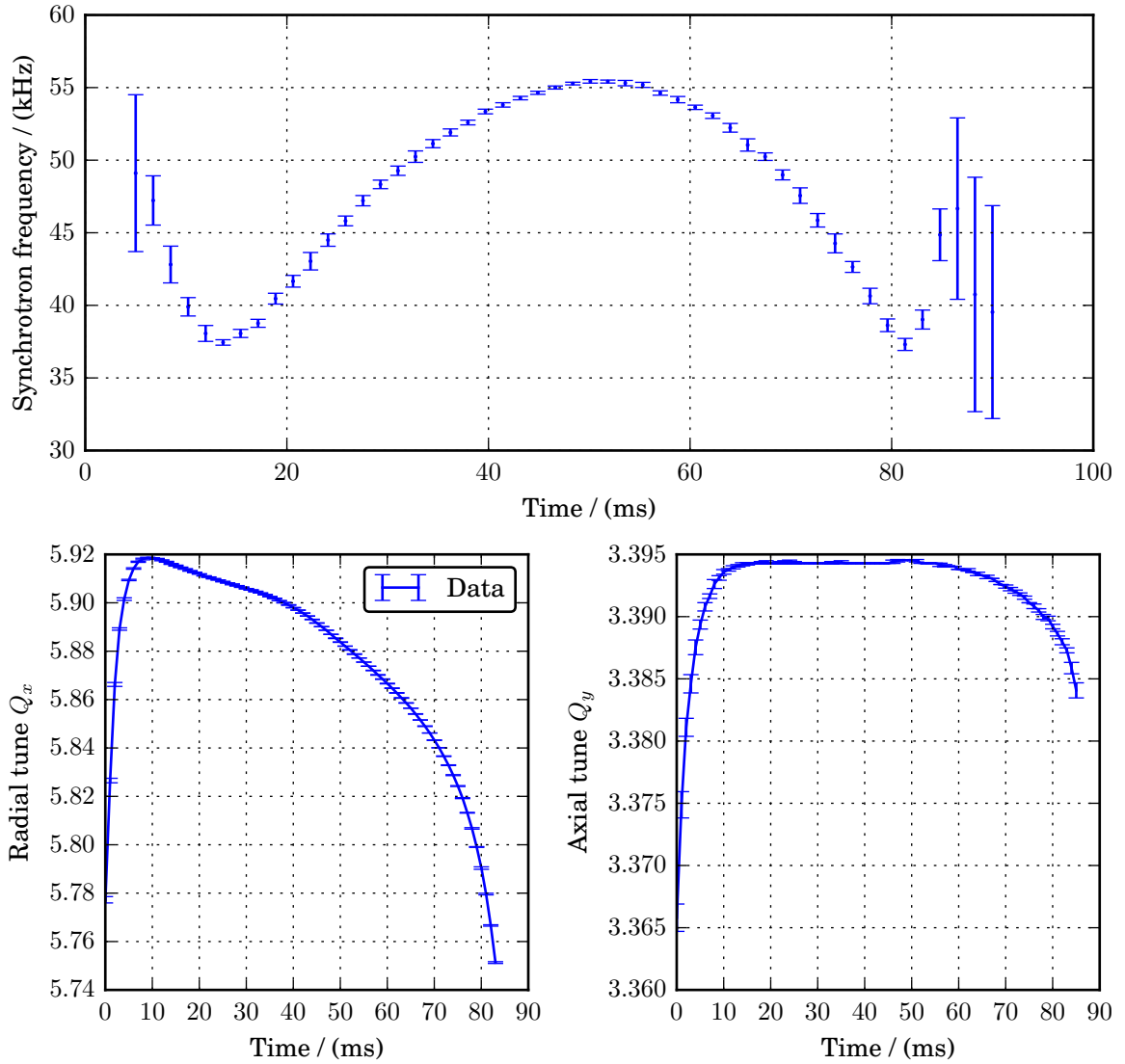

Figure 4.6.: The measured transverse tunes and synchrotron frequency over time on the booster ramp show a small transverse tune variation of $\sim$3 % in Q_x and $\sim$1 % in Q_y. [1,26]
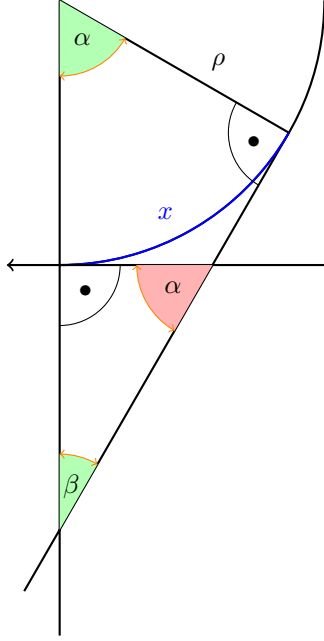
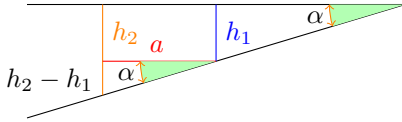Figure 4.7.: Length x of arc into dipole before camera. [7]

Figure 4.8.: Determination of angle of beam spot camera line. [7]

Thus the assumption of an energy independent booster optics can be made. In order to find the imaged orbit position the unknown and not accessible arc length x (Figure 4.7) along the orbit into the dipole must be determined:

$$\alpha = \frac{x}{R} \qquad \Rightarrow \qquad x = R\alpha. \tag{4.8}$$

The bending radius R is well known and the angle α can be determined from the distance between the orbit and the optical path at two points (Figure 4.8):

$$\alpha = \frac{h_2 - h_1}{a}. \tag{4.9}$$

Where a is the distance between the two points. The distances h_1 and h_2 were measured with a Vernier scale:

$$h_1 = (99.55 \pm 0.05)\,\text{mm} \tag{4.10}$$

$$h_2 = (114.1 \pm 0.05)\,\text{mm} \tag{4.11}$$

$$a = (383 \pm 3)\,\text{mm} \tag{4.12}$$

$$\Rightarrow \alpha \approx \boxed{0.0379 \pm 0.0196} \tag{4.13}$$

$$\Rightarrow x \approx \boxed{(0.253 \pm 0.131)\,\text{m}}. \tag{4.14}$$

The simulation gives the following Twiss parameters and dispersion at $0.253\,\text{m}$ before the end of a dipole:

$$\beta_x(s_0) = 9.1 \pm 0.8 \tag{4.15}$$

$$\beta_y(s_0) = 2.9 \pm 0.2 \tag{4.16}$$

$$D_x(s_0) = 0.71 \pm 0.05. \tag{4.17}$$

The axial emittance of the beam can now be calculated (Equation 2.130) from the measured spot sizes and the simulated Twiss parameters using the simple estimation of the imaging factor. The results are far off. The problem is that there are no existing scales for the beam position monitors (BPM) and also no reliable tables for the fields in the steerer magnets oft the booster. Thus there was no available reference measurement for the beam size in the booster. The solution was to calibrate the measured dispersion free axial emittance to match the one measured in the transfer line (Figure 4.15). This gave a new and far more trustworthy imaging factor of $A \approx 0.59$.

For the radial emittance (Equation 2.145) the energy spread dependant dispersion has to be considered. Also the energy dependence of the energy spread itself has to be taken into account. The energy spread $\sigma_\delta(E)$ is taken from the booster ramp simulations (Section 5.4) derived from the differential equation for the dynamic emittance and using the known starting values from the linac (Table 3.1).

For this measurement a Pulnix TM-9701[35] camera with a silicon CCD "KODAK KAI-0373 IMAGE SENSOR"[36] was used. The photon energy dependant quantum efficiency of the used CCD combined with the energy dependant transmittance of the optical path allows measurements starting at some 200 MeV with $E_c \approx 2.7$ eV. Taking the optical transmittance of fused quartz from 200 up to 3000 nm with fused quartz being the protective layer on the CCD and hopefully also the window for the synchrotron radiation and the band gap of silicon at 1116.97 nm=1.11 eV (near infra red) the measurable wavelength should lie between some 300 and 1100 nm. Presumably the glass of the standard consumer grade zoom camera lens is the limiting factor here. The first camera showed a strong non linearity between the measured spot sizes and the intensity that was found to be due to some mismatch in the analogue signal processing between the camera and

Figure 4.9.: Observed error function at extraction reveals the exposure time of the synchrotron radiation imaging camera[2,3]

the frame grabber card. The camera was therefore exchanged for another camera of the same type. The second camera was an improvement but also gave intensity dependant spot sizes (measured beam widths at one time setting of the booster are current dependant). The integration time of the camera is in the order of 0.3 ms (Figure 4.9). To minimize the effect of the non linearity on the measured spot sizes the summed ROI intensity and the booster current were used to filter the data (Figure 4.10) from measurements at fluctuating booster currents and ROI intensities.
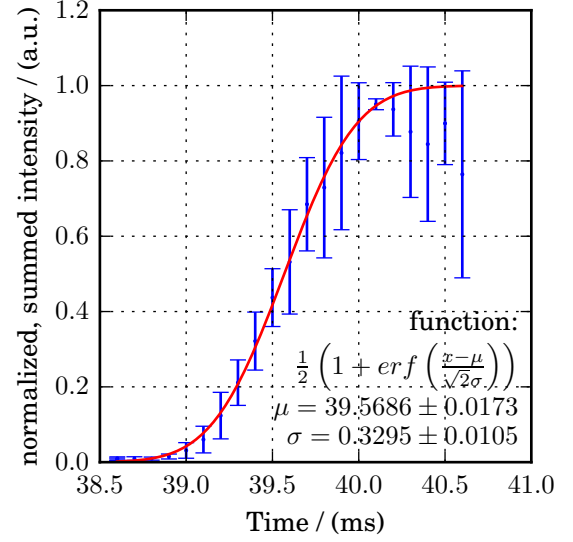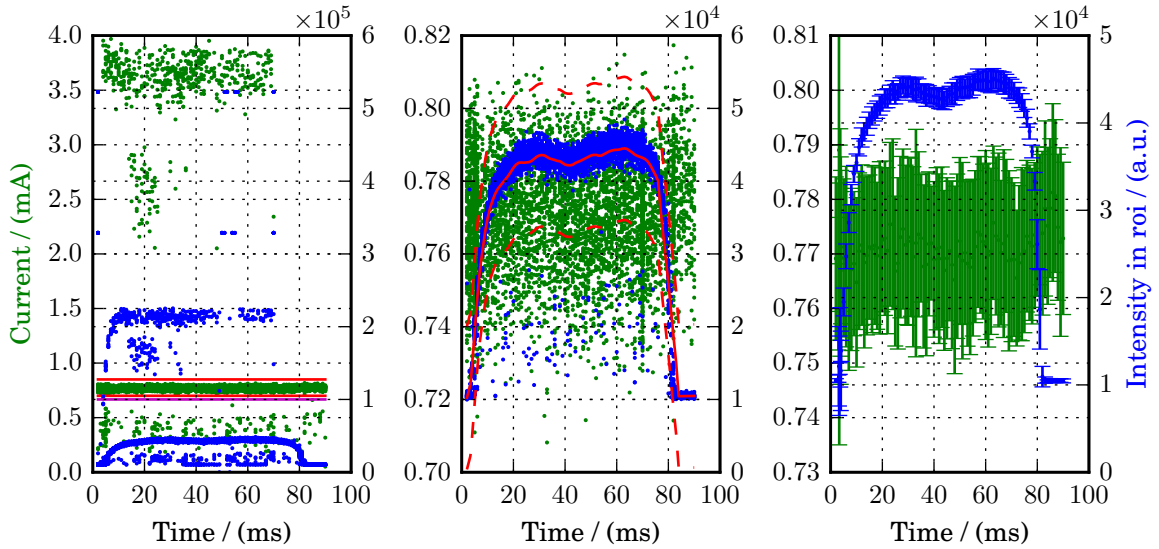

Figure 4.10.: Intensity in ROI and current are used as filters for sorting the data. First the dataset is trimmed to the low booster currents. Then a locally weighted linear regression curve through the ROI summed intensity data is used to trim far off data points.[39]

4. Measurement of the transverse emittance in the injection chain

The measured transverse emittance ramps (Figures 4.11,4.12,4.13,4.14) after calibrating the imaging factor to match the measured axial emittance in the transfer line show some agreement with the simulated ones (Figures 5.5,5.6). After injection into the booster the quality of the measured data is dominated by the low synchrotron radiation power. At first the adiabatic damping of the emittance should be observed as decrease of the emittance curve and flat region for the normalized emittance. Then the quantum excitation should start to dominate the damping effects and the emittance should rise to reach its maximum at maximum booster energy.
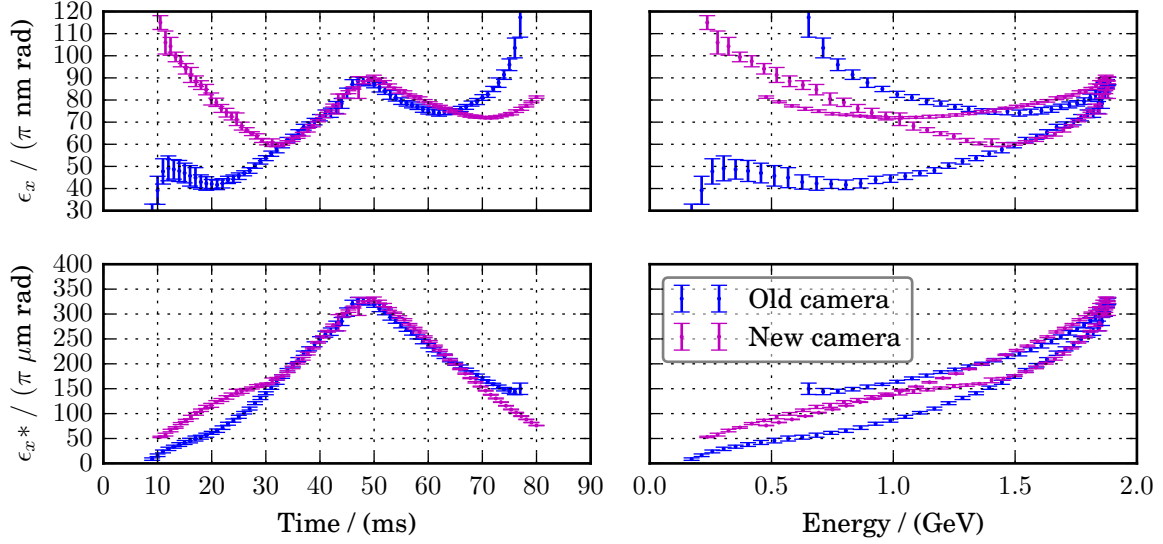

Figure 4.11.: Radial emittance over the booster ramp shows damping and quantum excitation. [1,2]
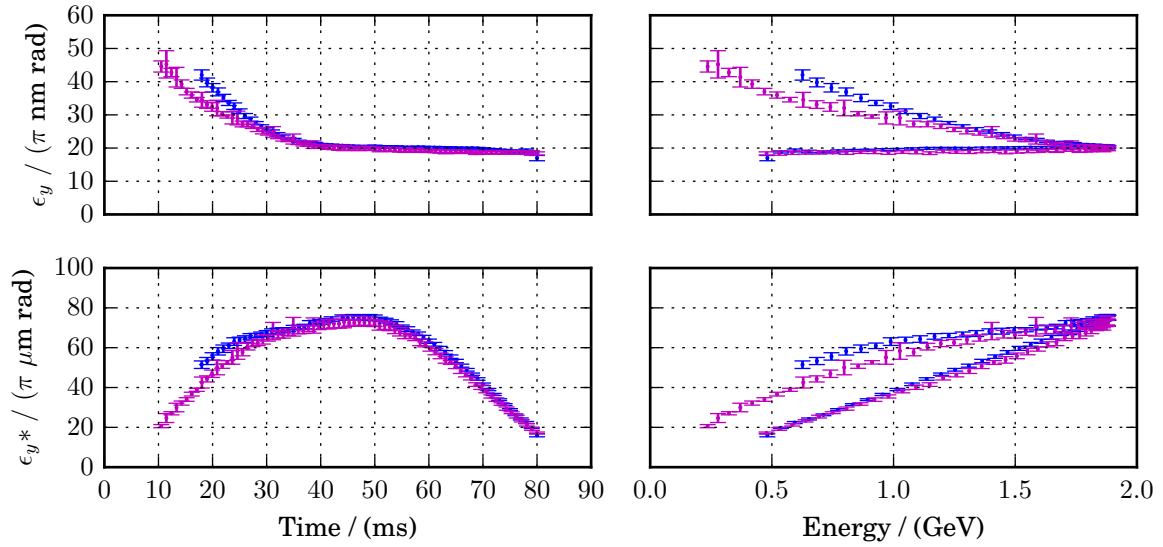
Figure 4.12.: Axial emittance over the booster ramp only shows damping but not to the fundamental limit indicating coupling in the booster. [1,2]

The plots show that the original camera measurements were dominated by the non linearity of the camera at low intensities and not conform to the measured injected emittance of some $200\,\pi$nm·rad. They even showed a non existent excitation of the curve directly after injection. In contrast the measured curve of the new camera seems to be conform with the measured injected emittances

(Figure 5.5). In the lower plots the normalized emittance is plotted where the adiabatic damping is multiplied out. Here the curve should stay flat until quantum excitation kicks in.

The locations of the minima can be controlled to a certain extent by the cavity timing.
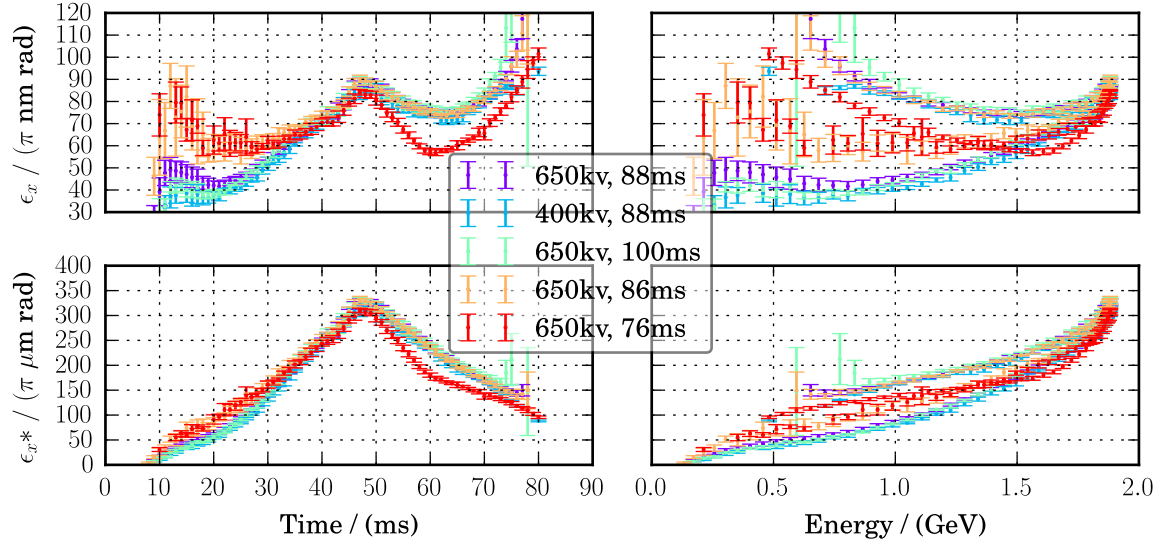

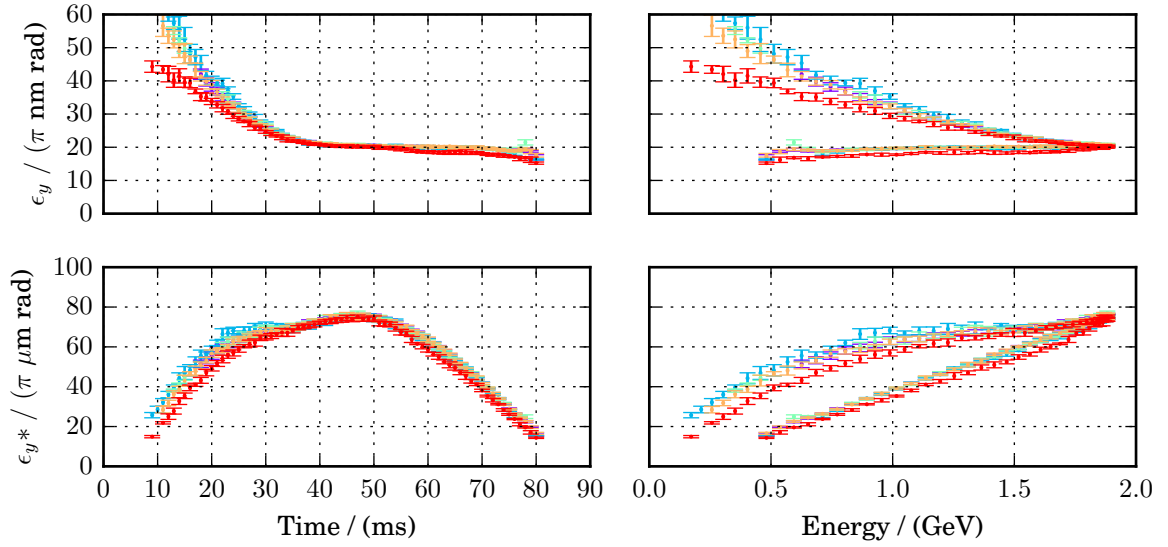Figure 4.13.: Radial emittance over the booster ramp for different cavity peak voltages and phase offsets. [1,2]

Figure 4.14.: Axial emittance over the booster ramp for different cavity peak voltages and phase offsets. [1,2]

4.4. Transfer line

As the transfer line runs right past the linac measurements must be carefully planned taking the radiation sensitive cathode of the linac into account. Only when the linac is running at low currents and single bunches should a FOM be inserted into the beam path.
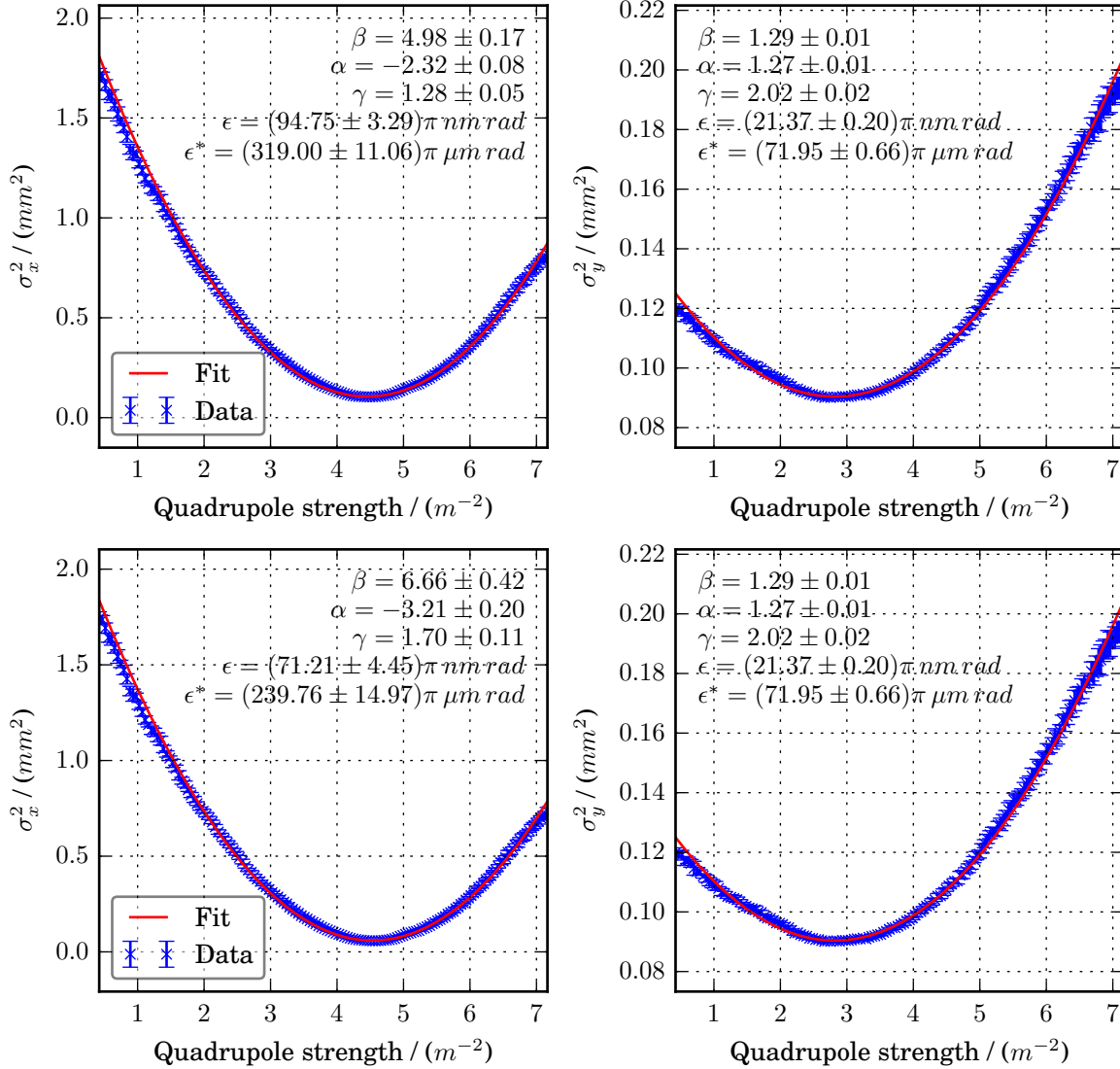
Figure 4.15.: Quadrupole scan with $\sigma_\delta = 0.56$ and the upstream dispersion functions:
a) from the linear optics simulation of the design optics: $D = 0.313\,\text{m}$, $D' = -0.05\,\text{rad}$
b) $D = 0.313\,\text{m}$, $D' = -0.15\,\text{rad}$[1,2]

Since the transfer line is not dispersion free the measurements are accompanied by high uncertainties not reflected by the given uncertainties that are based on the fit errors. The shown results are from the end of the transfer line where the dispersion is smallest according to the design optics. The last transfer line quadrupole Q12PT is varied and the beam is measured on FOMZ8T. The obtained radial emittance can be doubled by only slightly changing the fixed upstream derived dispersion. This shows the biggest difficulty with quadrupole scans in dispersive sections. The required derived dispersion to reach the suspected radial emittance of $\epsilon_x \approx 70\,\pi\text{nm} \cdot \text{rad}$ is close to the design optics. But the Twiss parameters do not agree well(Table 4.1). The dispersion of the DANFYSIK optics is

not compatible to the measurements which strongly questions this optics and the quadrupole current to strength conversion functions taken from the DANFYSIK measurements.

	β_x	α_x	β_y	α_y	D	D'
Quadrupole scan	6.66	-3.21	1.29	1.27	0.313	-0.18
Design optics	14.3	-7.4	7.65	4.71	0.313	-0.05
Alternative optics	18.3	-12.8	2.32	1.55	1.78	0.86

Table 4.1.: Comparison of Twiss parameters and dispersion from different optics and a quadrupole scan measurement.

This result is disappointing: on the one hand there are the measured R_{16} (Table 3.4) showing a reasonable agreement of the energy dependant orbit with the new transfer line optics based on the DANYFYSIK magnet scaling and on the other hand these optics fail to predict Twiss parameters in order of those measured with the quadrupole scan. Thus it remains an unsorted issue and a challenge to understand the linear optics of the transfer line.

5. Simulation of the booster ramp

The magnetic fields and thus the Energy over the BESSY II booster ramp are defined by the white circuits[25] powering the magnets. These run with 10Hz and are designed to provide the fields required to reach the injection Energy of 52 MeV at the beginning and the extraction energy of 1.7 GeV matching the storage ring energy at extraction.

5.1. Timing
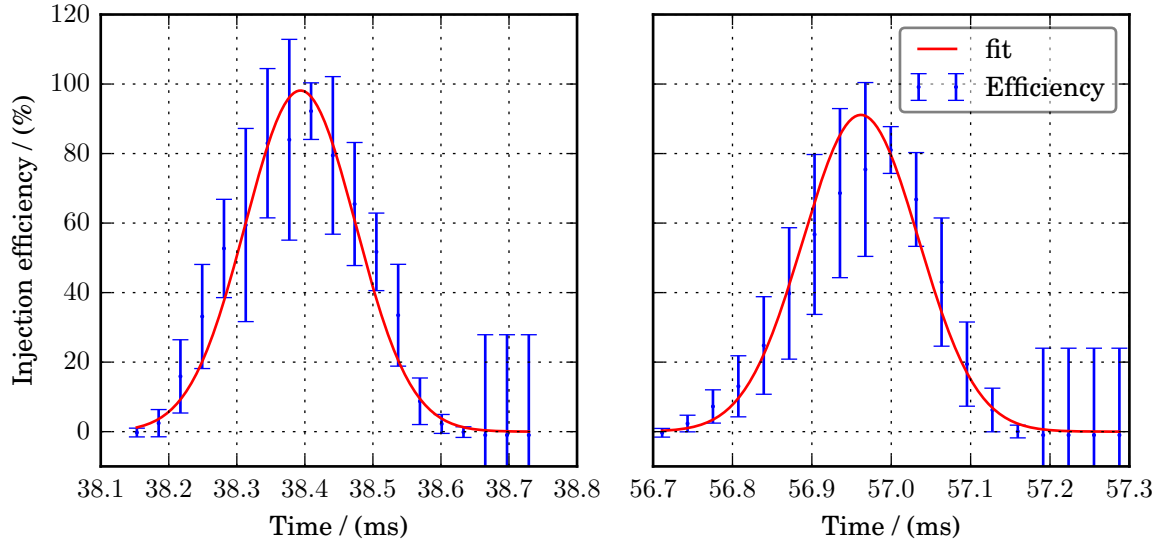
Figure 5.1.: Injection efficiency into the storage Ring gives the times at which the booster has the storage ring design energy of 1.72 GeV [2,5]

Before simulating the booster ramp timing information is required. The booster time with the same energy as in the storage ring, which is well known to be 1.72 GeV[24,40], was determined by varying the extraction time and measuring the injection efficiency into the storage ring. It is maximized when the energies match. A Gaussian fit to the measured data gives:

$$t_{ext1} = 38.39 \pm 0.08 \text{ms} \tag{5.1}$$

$$t_{ext2} = 56.96 \pm 0.07 \text{ms} \tag{5.2}$$

The injection time

$$t_{inj} = 5.52 \text{ ms} \tag{5.3}$$

is taken from the set timings in the BESSY II control system.

5.2. Energy

Taking the three points of known time and energy and assuming a sinusoidal energy ramp the energy and corresponding magnetic flux density in the dipoles can easily be calculated over the ramp (Figure 5.2).

$$E(t) = A \sin(\omega(t + t_0)) + E_{off} \tag{5.4}$$

$$\Rightarrow \quad t_0 = \frac{1}{4f} - \hat{t} \tag{5.5}$$

$$\Rightarrow \quad A = \frac{E_{ext} - E_{inj}}{\sin(\omega(t_{ext} + t_0)) - \sin(\omega(t_{inj} + t_0))} \tag{5.6}$$

$$\Rightarrow \quad E_{off} = E_{inj} - A \sin(\omega * (t_{inj} + t_0)) \tag{5.7}$$

The white circuits powering the booster magnets determine the magnetic flux density B in the magnets. The fixed bending radius R of the dipoles in combination with this flux density defines the energy of the electrons (Equation 2.50) in the booster at any given time (Figure 5.2). The booster cavity provides the necessary acceleration to keep the injected electrons at this energy over the entire ramp.

With its circumference of 96 m the booster has a revolution time of about 320 ns. Together with the cavity RF-frequency of 500 MHz this results in 160 buckets with an acceptance of 0.5 ns or 15 cm that are each 2 ns apart.
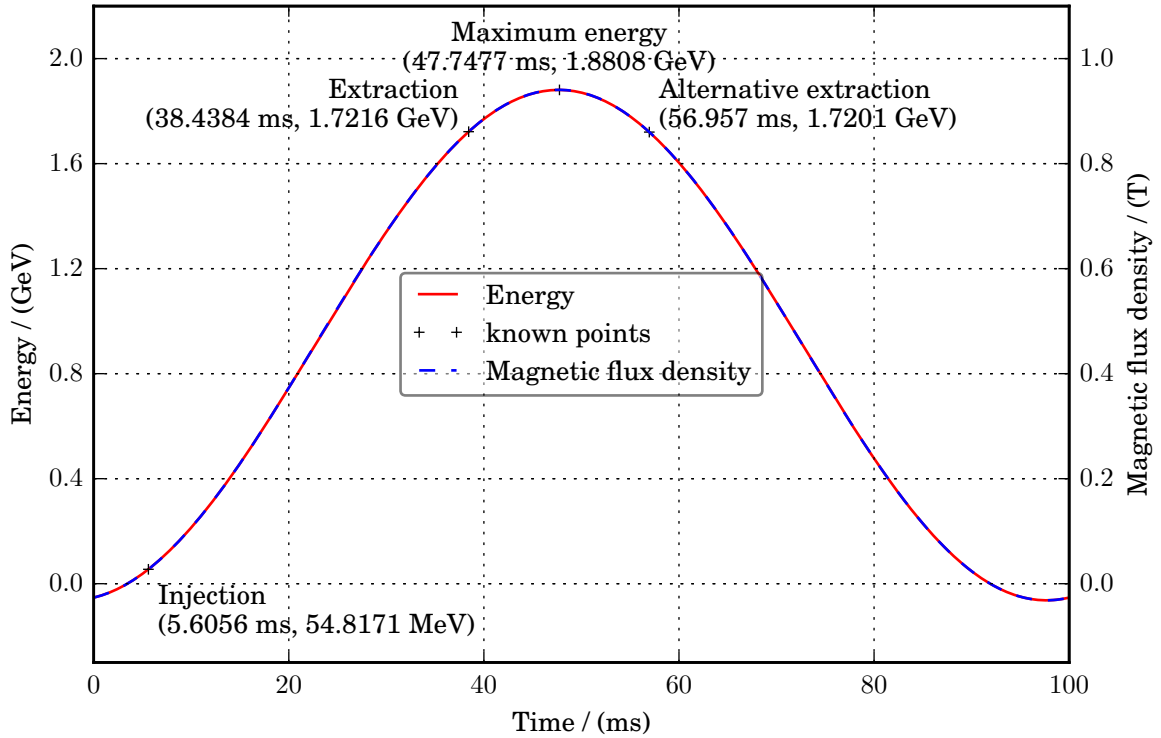

Figure 5.2.: Particle energy and magnetic flux density in dipoles in the booster [1,2]

5.3. Radiation loss and cavity

The cavity does not only have to provide the acceleration to the energy defined by the white circuits, but also has to compensate for the synchrotron radiation loss (Figure 5.3). The energy loss per turn and electron (Equation 2.170) is calculated from the revolution time spent in the bending magnets $T_{rev} = \frac{2\pi R}{\beta c}$ and the mean radiated power (Equation 2.166) at the momentary energy.
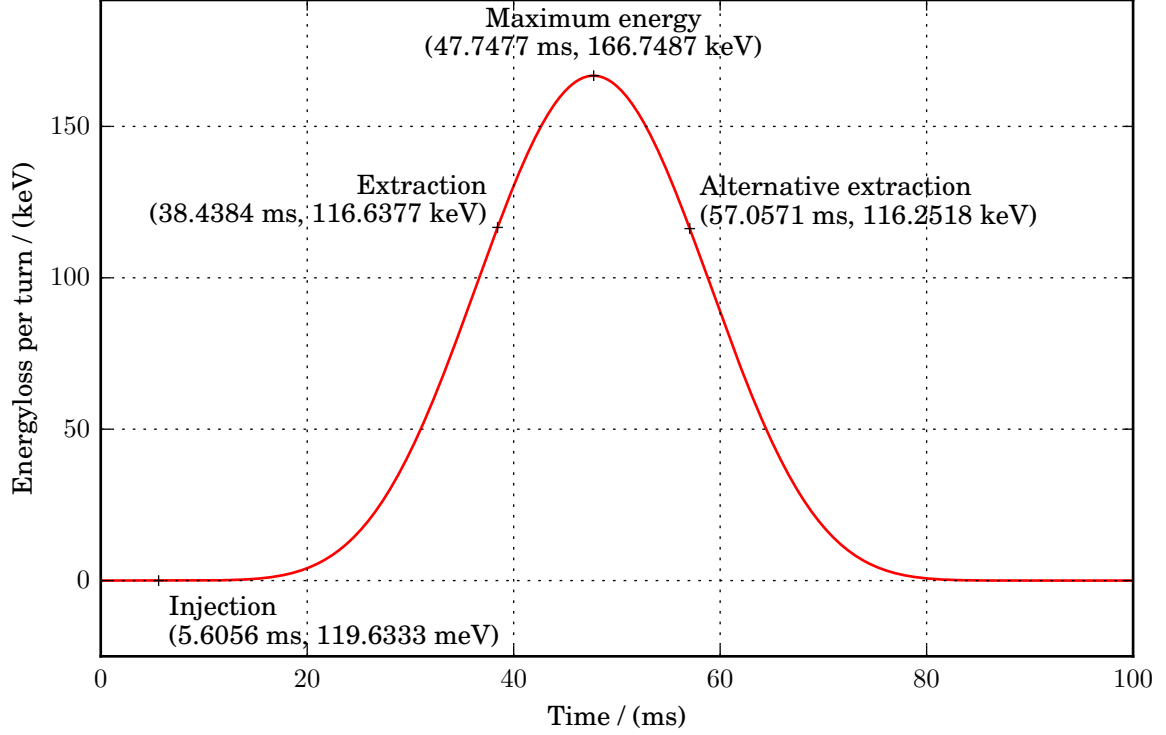
Figure 5.3.: Energy loss per turn due to synchrotron radiation in the booster

This lost energy and the required acceleration to comply with the energy defined by the dipole fields (Figure 5.2) must be gained in the booster cavity. The energy gain in the electric field of the cavity can be calculated by integrating over the accelerating force (Equation 2.39). Since the magnetic fields are always perpendicular to the velocity ($\Rightarrow \vec{v} \times \vec{B} = 0$), the acceleration is given by the "seen" voltage[9]:

$$\Delta E = e \int_{\vec{r_1}}^{\vec{r_2}} \vec{E} d\vec{r} = eU$$

making it simple to calculate the voltage the electrons need in the cavity (Figure 5.4). The peak voltage in the cavity is usually significantly higher to shorten the bunches by phase focussing[26] due to the higher voltage gradient at the correct phase. This so called over voltage factor is on the order of 4.3 with approximately $720\,\mathrm{kV}$ cavity voltage in the BESSY II booster cavity.

Figure 5.4.: Required voltage in the booster cavity for each electron to compensate radiation loss of last turn and accelerate to the required energy of the next turn
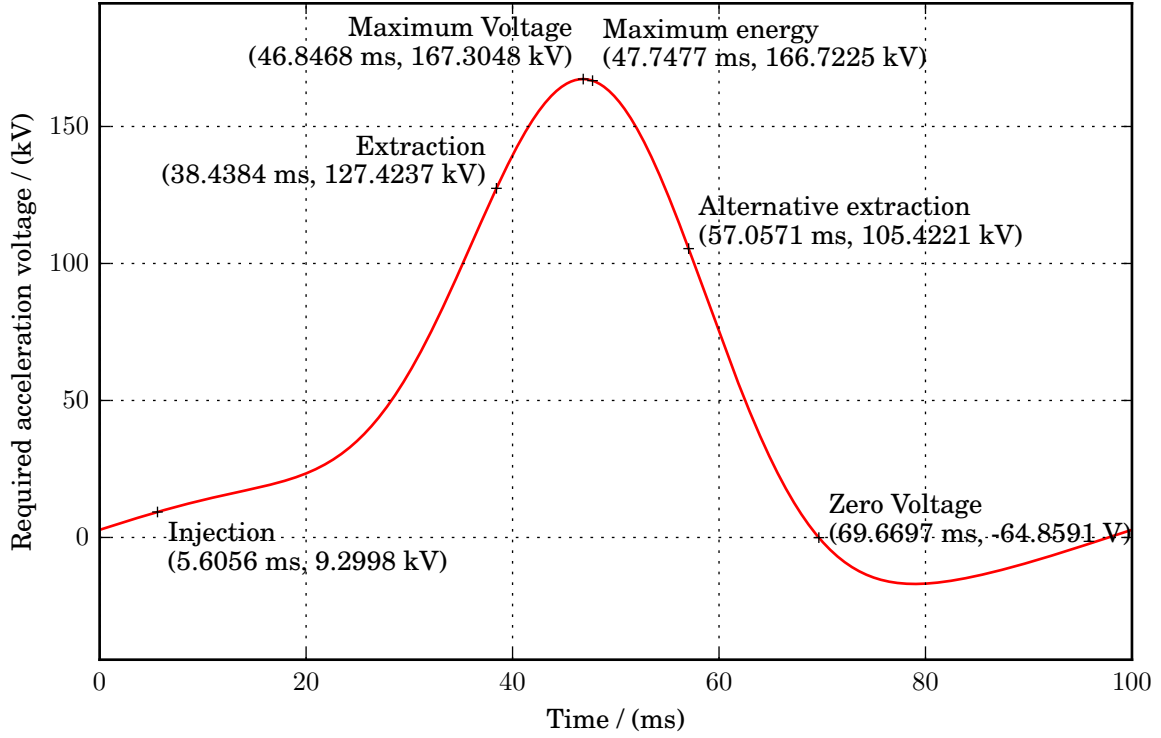
5.4. Emittance

The dynamic emittance derived in section 2.2

$$\dot{\epsilon}_u(t) = q_u(t) - \left(\frac{\dot{E}(t)}{E(t)} + \alpha_u(t) \right) \epsilon_u(t) \tag{5.8}$$

can be solved from a fixed initial emittance with an appropriate numerical integrator. The time dependant energy (Figure 5.2) and its derivative are already known. The synchrotron integrals (Equations 2.188, 2.189, 2.190, 2.192) required for the calculation of the time dependant damping decrement (Equation 2.205) and quantum excitation (Equation 2.217) are calculated from the well understood linear optics of the booster.

First simulations were run using an own Euler and later Runge-Kutta integrator still available in the source code of ACCPY. But the built in numerical integrator "Real-valued Variable-coefficient Ordinary Differential Equation solver (VODE)" from SCIPY[3] turned out to be faster and is now implemented. A simulation of the BESSY II booster ramp emittance in all planes with 1000 slicing points takes less than 10 seconds on a laptop with an Intel© Core™ i7-4710MQ processor.

Radial emittance

$$q_x(t) = \frac{2C_q C_\alpha}{R^2} \gamma(t)^2 E(t)^3 \frac{\mathcal{I}_{5x}}{\mathcal{I}_2} \tag{5.9}$$

$$\alpha_x(t) = \frac{2C_\alpha E^3}{R^2} J_x \qquad \text{with:} \quad J_x = 1 - \frac{\mathcal{I}_{4x}}{\mathcal{I}_2} \tag{5.10}$$

The time dependant radial emittance is the result of adiabatic and radiation damping working against the quantum excitation(Figure 5.5). At low energies the radiated synchrotron power is small and the adiabatic damping dominates giving a curve, falling exponentially with the damping time. At higher energies the excitation kicks in and increases the radial emittance. The time or energy of the minima in between is determined by the injected emittance. The bigger the injected emittance is the later the minima is reached. Shortly after and before extraction the emittance becomes independent from the injected value.
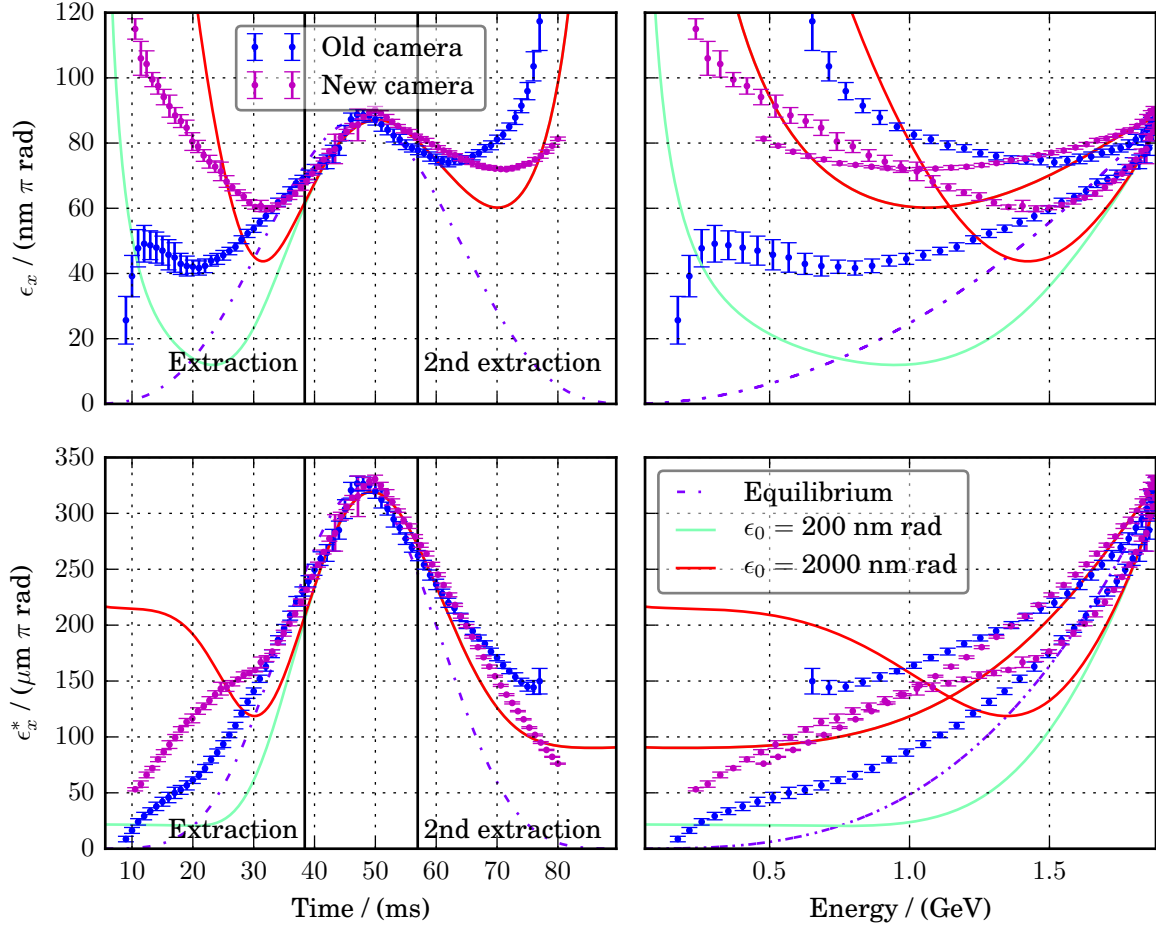

Figure 5.5.: Development of the dynamic (for different initial ϵ_x), equilibrium and measured radial emittance over time (left side) and energy (right side) and the corresponding normalized emittances (below).

The measured data's absolute values near the maxima are in good agreement with simulation for both cameras. They give an emittance at extraction of some $60\,\pi$nm·rad so about $18\,\%$ smaller than the equilibrium emittance of some $73\,\pi$nm·rad at extraction. These $18\,\%$ emittance are won by the fast ramp. The qualitative curve propagation further away from the maxima shows the strong non linearity of the old camera measuring smaller spot sizes due to the low intensity at lower energies. The new cameras qualitative curve propagation is in fair agreement with the simulation. The position of its minima seems to correspond to an injected emittance of some $2000\,\pi$nm·rad - 10 times bigger than the measured radial emittance in the injection line. This could be due to an off orbit injection into the booster, resulting in a beam with non-zero first order moments of the beam distribution function. These are neglected in the derived formulae (Equations 2.225, 2.222) used to calculate the

emittance from the measured beam widths.

Axial emittance

$$q_y(t) = \frac{2C_q C_\alpha}{R^2} \gamma(t)^2 E(t)^3 \frac{\mathcal{I}_{5y}}{\mathcal{I}_2} \approx 0 \tag{5.11}$$

$$\alpha_y(t) = \frac{2C_\alpha E^3}{R^2} J_y \qquad \text{with:} \quad J_y = 1 - \frac{\mathcal{I}_{4y}}{\mathcal{I}_2} \tag{5.12}$$

With zero axial dispersion follows $\mathcal{I}_{5y} = 0$ and thus there is usually no quantum excitation in the axial plane. In an ideal lattice the time dependant axial emittance is the result of adiabatic and radiation damping working against excitation due to the recoil of emitted photons (Figure 5.6). The emittance is then damped to the fundamental lower limit of some $0.2\,\pi$pm·rad. The measured lower limit is in the order of $20\,\pi$nm·rad so 10^5 times bigger than the actual value due to coupling effects that enable sharing of transverse emittance. The time at which the measured axial emittance reaches its equilibrium is in good accordance with the simulated one.
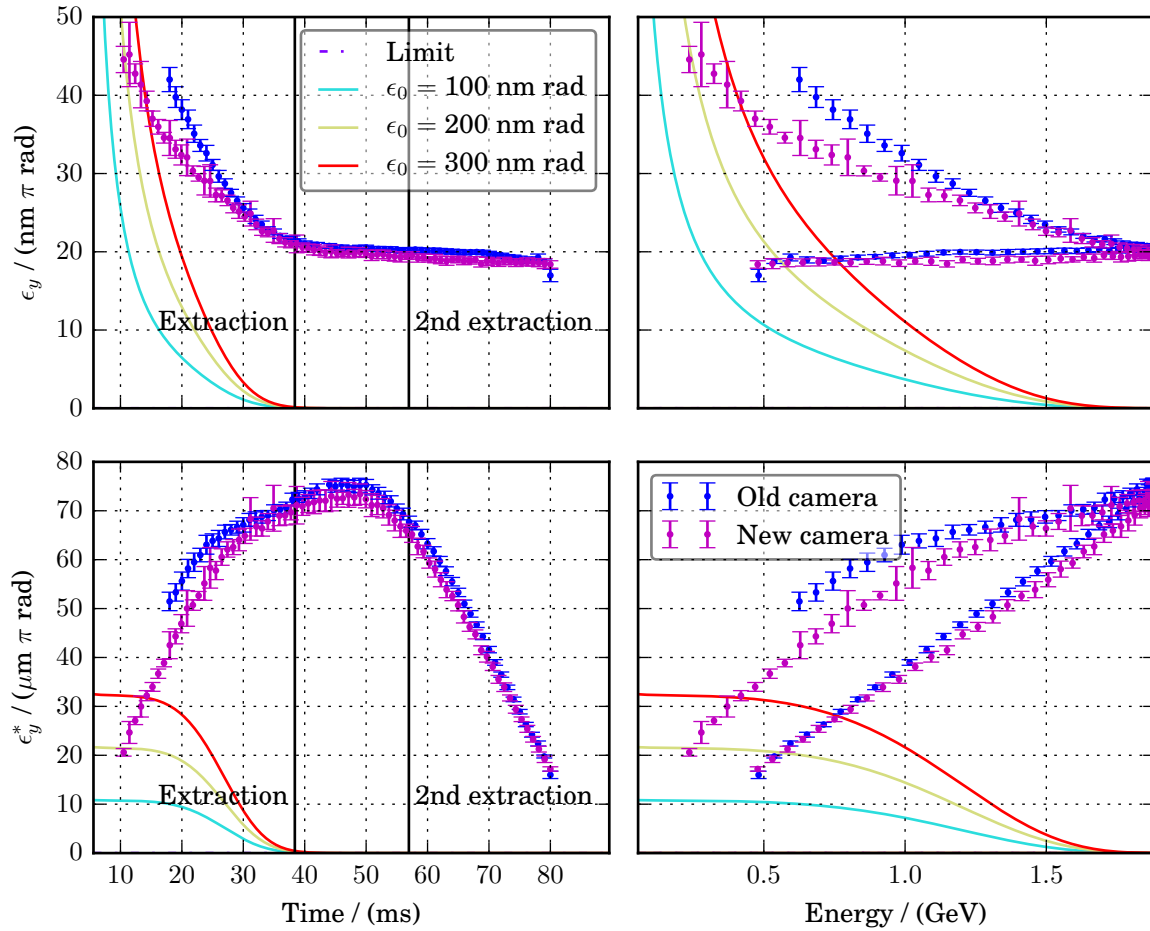
Figure 5.6.: Development of the dynamic (for different initial ϵ_y), equilibrium and measured axial emittance over time (left side) and energy (right side) and the corresponding normalized emittances (below).

Energy spread

$$q_s(t) = \frac{2C_q C_\alpha}{R^2} \gamma(t)^2 E(t)^3 \frac{\mathcal{I}_3}{\mathcal{I}_2} \tag{5.13}$$

$$\alpha_s(t) = \frac{2C_\alpha E^3}{R^2} J_s \qquad \text{with:} \quad J_s = 2 + \frac{\mathcal{I}_{4x} + \mathcal{I}_{4y}}{\mathcal{I}_2} \tag{5.14}$$

The time dependant behaviour of the energy spread is determined in analogy to the radial emittance by the struggle between the damping processes and the quantum excitation(Figure 5.7). It also becomes independent of the injected value before extraction. Giving an extracted energy spread of some 0.54 ‰ so about 3.5 % smaller than the equilibrium energy spread of about 0.56 ‰ at extraction. This smaller difference between equilibrium and dynamic emittance at extraction corresponds to the shorter longitudinal damping time in the booster (Figure 3.5).
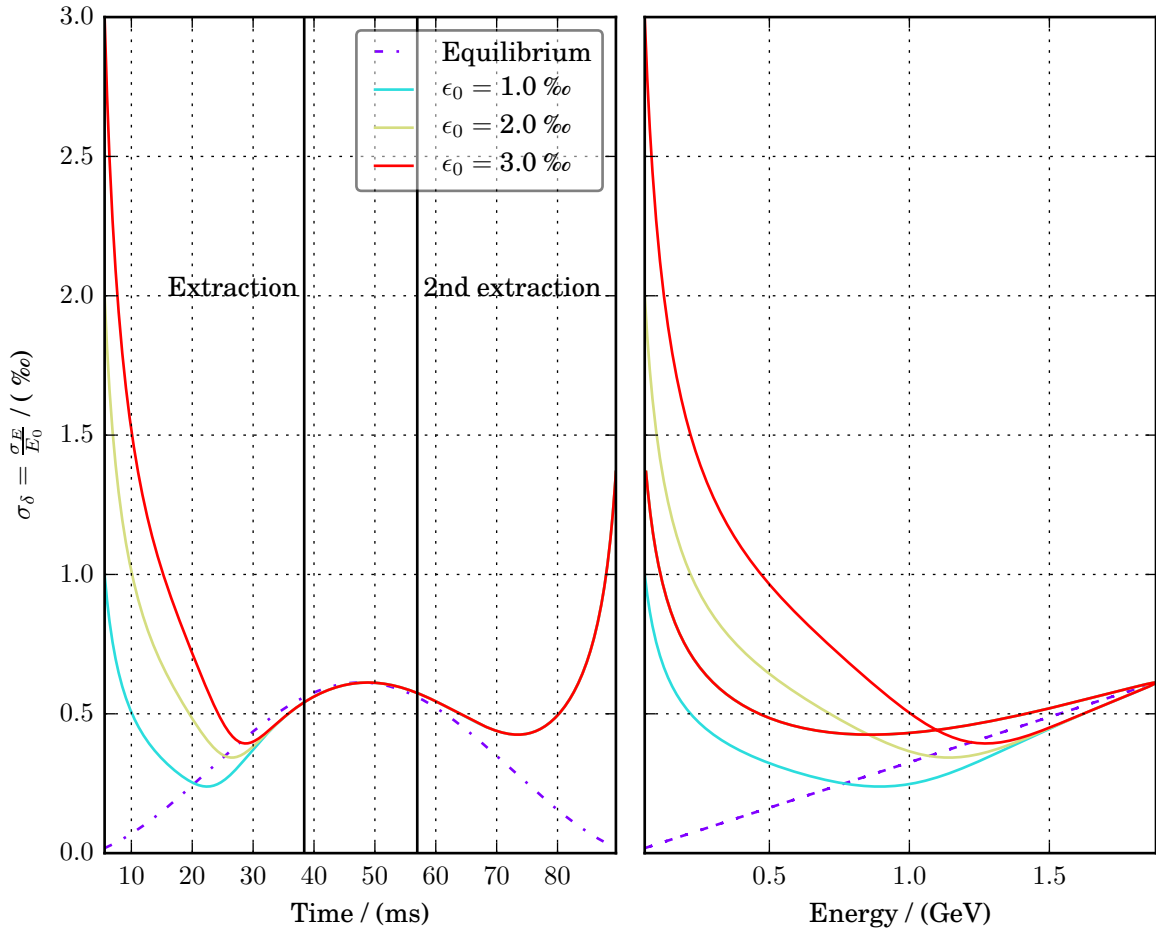

Figure 5.7.: Development of the dynamic (for different initial $\sigma_{\delta,0}$) and equilibrium energy spread over time (left side) and energy (right side).[1,2]

Synchrotron frequency

$$f_s = \frac{1}{T_{rev}} \sqrt{\frac{h\eta(t)V_{HF}(t)\cos(\phi_s(t))}{2\pi p(t)c}} \qquad (5.15)$$

The synchrotron frequency[41] of the bunches is determined by the cavity phase and voltage. The simulations (Figure 5.8) are based on an ideal cavity and thus a constant synchrotron phase. Therefore, the simulated synchrotron frequency is determined by the ration of the cavity voltage to the particle energy over the ramp.

The synchrotron frequency was measured with an oscilloscope taking the summed signal of the 4 pick-up electrodes of a beam position monitor (BPM) and using the trigger signal of the injection kicker as starting point for the oscilloscopes time-base sweep. A Python program also included in ACCPY[1] controlled the timing, fast Fourier transformation (FFT) settings (center and span of frequency) and data acquisition of the oscilloscope over the VXI11 interface using the Python module vxi11[42]. The center frequency was chosen as a whole multiple of the revolution harmonic frequency and found to give the best signal when looking at the 13th revolution harmonic. The frequency span must be chosen in the order of more than twice the suspected synchrotron frequency.
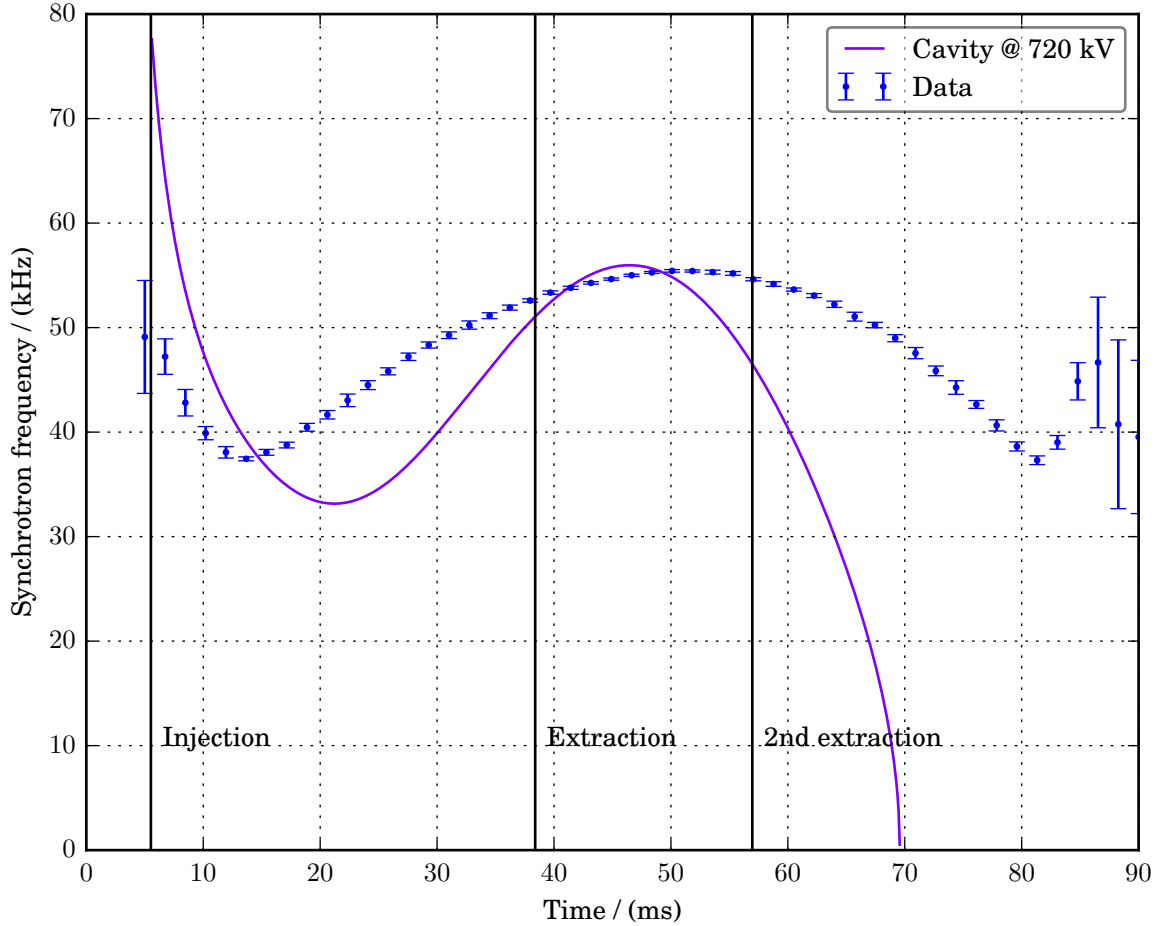
Figure 5.8.: The measured and simulated synchrotron frequency over the booster ramp with markers at the injection, extraction and peak energy of the booster ramp.[1,2]

Bunch length

$$\sigma_\tau(t) = \frac{\sigma_\delta(t)|\eta(t)|}{\omega_s} \tag{5.16}$$

The bunch length is determined by the energy spread σ_δ, the slip factor $\eta(t)$ and the synchrotron frequency ω_s [11]. At extraction the bunch length also is independent of the injected value. The dynamic bunch length at extraction is in the order of 56 ps and the bunch length calculated from the measured synchrotron frequency and the simulated energy spread and slip factor of 54 ps (Figure 5.9). With a superconducting cavity a voltage of 20 MV could be achieved with the corresponding bunch length at extraction reduced to approximately 11 ps as it is proportional to $\sqrt{V_{HF}}$

Figure 5.9.: The bunch lengths calculated from the simulated dynamic (for different initial $\sigma_{\delta,0}$) and equilibrium energy spreads for the simulated and measured ("Data") synchrotron frequency over the booster ramp. [1,2]

6. Optimization of the transverse emittance

The injection efficiency into the storage ring is equivalent to the ratio of the number of electrons extracted from the booster to the increase of the number of electrons in the storage ring. For high injection efficiencies into the storage r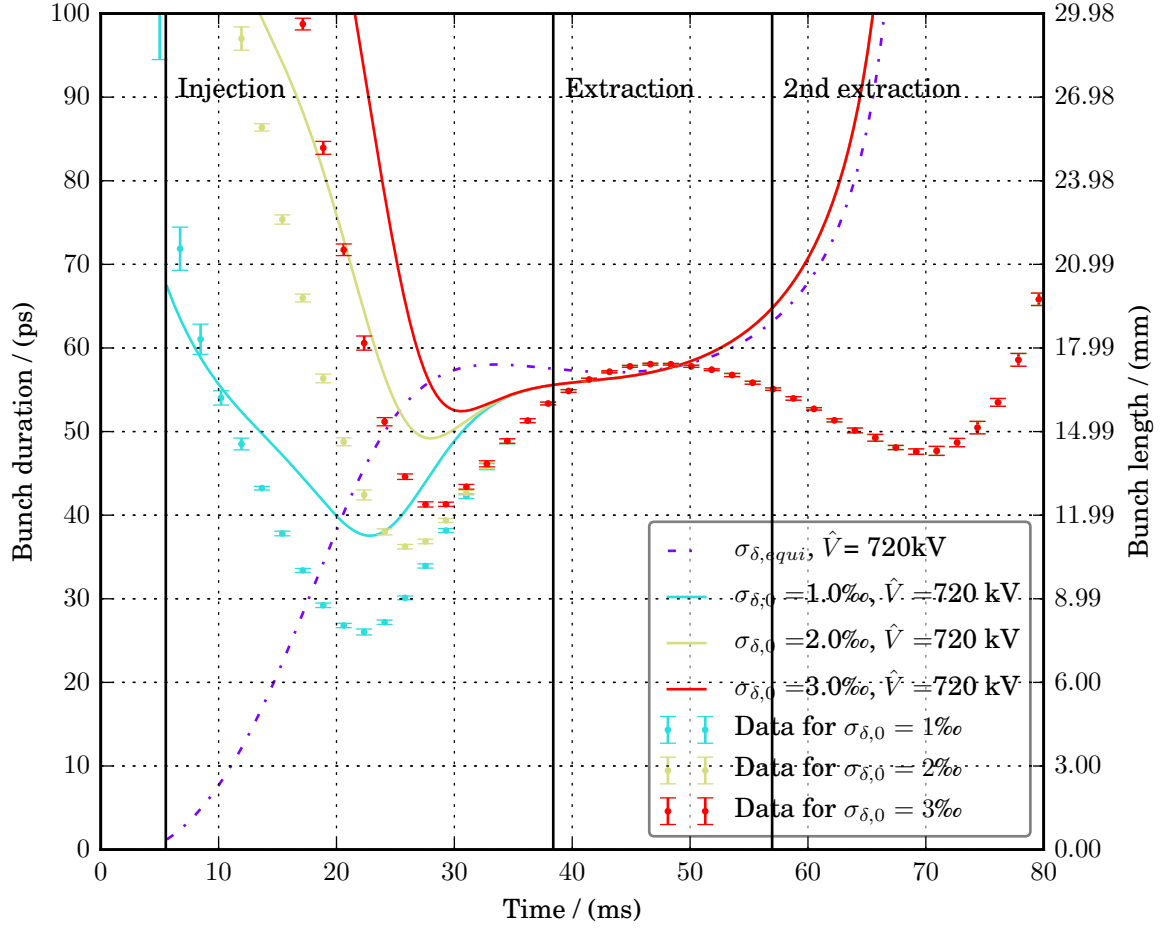ing the injected beam must fit the acceptance of the storage ring. Furthermore, the beam parameters of the injected beam should be well matched against those of the storage ring beam at the injection point. Due to the smaller circumference of the booster in relation to the storage ring the transverse and longitudinal equilibrium emittances of the booster at extraction energy are greater than those of the storage ring.

One focus of this work lies on the possibilities of optimizing the transverse emittance for improving injection into the storage ring. The radial off-axis injection into the storage ring requires a large radial acceptance of the storage ring. As the quantum excitation of the beam only increases the radial emittance the beam in the booster has a ratio of radial to axial emittance of about 4 to 1 ((Figure 4.11)). The comparatively large radial emittance of the injected beam increases the required radial acceptance of the storage ring even more.

In the momentary situation the axial acceptance of the storage ring is larger than the required while the radial acceptance is at its limit. With a partial or total exchange of the transverse emittance before injection into the storage ring one could minimize the radial emittance and take advantage of this circumstance. Some of the possible methods to achieve such an emittance exchange are presented here.

6.1. Overview of some possible methods to optimize transverse emittance

The possibility of minimizing the transverse emittance by optimizing the booster synchrotron optics is already at its limit. Further improvements are not possible without hitting the limit of dynamic aperture or an exchange of hardware. Limits of further booster optics optimization by rewiring and then optimizing the quadrupoles with a bigger parameter space can be found in [43], showing a maximum gain in the transverse emittance on the order of 10%. Hereby, confirming the found optimized booster optics from April 2007.

Liouville's theorem states that the total emittance is a conserved quantity. This is valid for conservative systems which the booster synchrotron is not. The radial emittance ϵ_x after ramping to 1.72 GeV is about 4 times bigger than the axial emittance ϵ_y due to quantum excitation. The total emittance cannot be reduced but an exchange of the radial and axial emittance promises a gain of factor 4 in the radial plane which is critical for the injection into the storage ring. Here an overview of some possibilities to achieve such an exchange of transverse emittances before injection into the storage ring is presented.

1. Emittance exchange in the transfer line with skew quadrupoles
   $\Rightarrow$ With a set of 5 or more skew quadrupoles a beam rotating transfer matrix can be achieved (Section 6.2). The transverse emittances are perfectly exchanged. But the dispersion is

also exchanged giving axial dispersion after the emittance exchange section in case of non-zero radial dispersion at the beginning. In the BESSY II transfer line the axial dispersion can only be controlled by the quadrupoles and the radial dispersion cannot easily be tuned to zero before an emittance exchange section making it impossible to inject into the storage ring at the desired Twiss parameters without axial dispersion [44].

2. Emittance sharing in the booster by operating it on a tune difference resonance at non-zero coupling

    ⇒ As result of construction and alignment errors of the magnets the transverse oscillations are usually coupled to a certain extent. This extent is described by the coupling coefficient κ. Quadrupole errors represent the linear contribution to the coupling [11]:

    $$\kappa = \pm \left| \frac{1}{2\pi} \int_s^{s+L} k_{skew} \sqrt{\beta_x \beta_y} \exp(i\Psi) ds \right| \tag{6.1}$$

    $$\text{with} \quad \Psi(s) = \psi_x(s) \pm \psi_y(s) - (Q_x \pm Q_y + q)\frac{2\pi s}{L} \tag{6.2}$$

    with the betatron phases $\psi_u(s)$ and integer q. If the booster is operated at a transverse tune sum resonance $|Q_x + Q_y - q| \leq \kappa$ both transverse emittances grow unlimited. At the transverse tunes difference resonance: $Q_x - Q_y - q = \Delta \approx 0$ the emittance is constantly exchanged between both planes with the frequency [11]:

    $$\Omega = \sqrt{\kappa^2 + \frac{\Delta^2}{2}}. \tag{6.3}$$

    Therefore, both planes experience equal emittance excitation and damping over the ramp resulting in a shared emittance between the transverse planes at extraction as they still obey Liouvilles theorem so that $\epsilon_x + \epsilon_y = \epsilon_{x,0}$ with $\epsilon_{x,0}$ being the uncoupled radial emittance.

3. Crossing of the boosters tune difference resonance

    ⇒ If the tune difference resonance is crossed in times short against the damping times and directly before extraction the emittances are exchanged without relevant sharing, as that takes place on the time scale of the damping times. For this method the initial tune difference must already be near the difference resonance in order to open the possibility of fast tune difference resonance crossing. For an efficient exchange in the order of 90 % the resonance must be crossed in about $2\,\text{ms}$ [45].

4. Operating the booster on the tune difference resonance

    ⇒ Instead of crossing the tune difference resonance it is also possible to operate the booster directly at this resonance while actively ensuring zero coupling and then introduce coupling with a pulsed skew quadrupole directly before extraction. The skew quadrupole must be strong and pulse within $2\,\mu$s the strong coupling while still directly at the difference resonance almost perfectly exchanges the transverse emittances [45]. The closer the booster is operated to the coupling resonance the weaker the pulsed quadrupole magnet to introduce the coupling may be. But this very fast pulsed quadrupole pulse corresponding to some 6 turns requires a very special magnet with a strong field. Further difficulties include the exact tuning of the optics which must be tuned very close to the

tune difference resonance. But the greatest difficulty lies in ensuring zero coupling over the ramp[45].

5. Booster with storage ring circumference

⇒ A straight forward method but very expensive way of achieving lower emittance from a booster is to rebuild it with a much larger circumference. A big booster with 240 m circumference can easily be designed by extending the present lattice by a factor of 2.5 and tuning the quadrupole strengths to reach 2.5 times the original tunes so as to ensure the same combination of Twiss parameters at extraction. Hereby, compensating the changed edge focussing due to the larger bending radii. Such a optics and the results of the ramp simulation in analogy to that of the present booster presented in the previous chapter can be found in Appendix B.5. Advantages are the substantially reduced emittances in all planes, the lower required flux density in the bending magnets and the smaller radiation losses. Also the dynamic emittances at extraction would then depend on the injected values introducing the possibility of even smaller emittance at extraction.

Method	Costs	Work time	ϵ_x	Score
Transfer line ϵ exchange	3	4	6	42
Booster ϵ sharing	5	5	3	30
Booster ϵ exchange by fast crossing of the coupling resonance	4	4	5.4	43.2
Booster ϵ exchange by fast excitation of the difference coupling resonance	2	2	5.9	23.6
Big booster	1	1	20	40

Table 6.1.: An approximate score for the costs and work time from 1 (very high) to 5 (none), decrease factors of the radial emittances assuming originally $\epsilon_x \sim 60\,\pi\text{nm} \cdot \text{rad}$, $\epsilon_y \sim 10\,\pi\text{nm} \cdot \text{rad}$) in each plane and the corresponding score calculated by: $(\text{Costs}+\text{Work time}) \cdot \prod \epsilon_u$ reflecting the bang for buck in transverse planes are illustrated

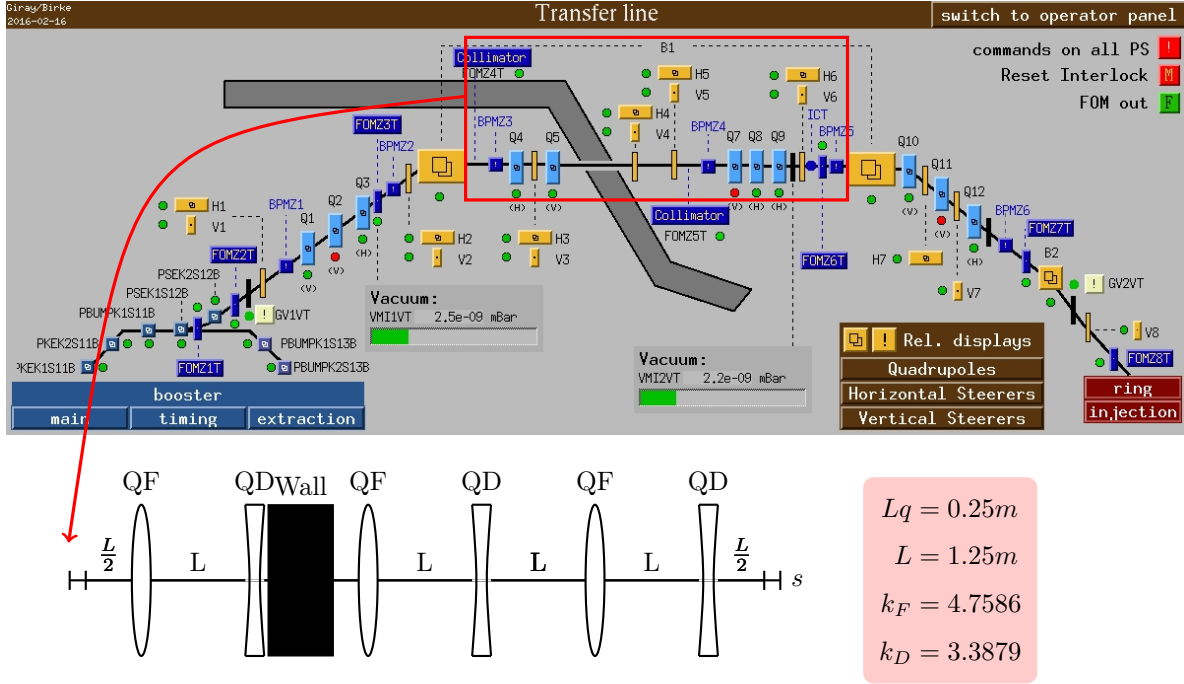## 6.2. Emittance exchange in the transfer line

Figure 6.1.: Highlight of a possible transfer line section for a transverse emittance exchange with a sequence of skew quadrupoles as illustrated below. [7]

In the transfer line a transverse emittance exchange can be realised with a set of skew quadrupoles. There is sufficient space available between the bending magnets. The fixed radiation wall has to be taken into account restricting the positioning possibilities of the quadrupoles. For a full emittance exchange it seems that at least 5 quadrupoles are required. The greater the distance between the quadrupoles is chosen the smaller the required gradients become. The long straight section of the transfer line (marked red in Figure 6.1) provides enough space to evenly distribute 6 quadrupoles without colliding with the wall. The proposed emittance exchange sequence of six skew quadrupoles (Figure 6.1) requires only 9 of the 9.43 m available space giving some flexibility for the positioning around the wall.

Using the derived transport matrix (Equation 2.250) that when rotated by $\pi/2$ give the beam rotation matrix (Equation 2.246) the proposed emittance exchange section can be found by numerically optimizing a system of non-skew quadrupoles and drifts to have the proposed transport matrix. In case of six quadrupoles and symmetric spacing the so called "Brown rotator" [9] with the additional condition of only two quadrupole strengths can be used to reduce the parameter space.

In total an overdetermined set of non linear equations is retrieved by multiplying out the general transfer matrices of the proposed sequence. The aim is to find the optimum where this matrix converges to the desired transport matrix (Equation 2.250). This is a global optimum in a large parameters space over a very large set of nonlinear equations. Finding this optimum proved to be a problem, as most optimization tools require just as many variables as equations. This problem could be bypassed at cost of numerical precision by summing up equations. However, the least squares method implemented in SciPy does not have this restriction and proved to be extremely fast at converging to plausible solutions and even faster when given the Jacobian of the equations. To find the best solution a randomized set of many possible start vectors (drift lengths and quadrupole

strengths) in a given range is passed to a multi-threaded brute force method that gives each start vector to the least squares optimization algorithm and checks if the returned minimum meets the set conditions and if so stops all threads and returns the solution.

For six quadrupoles a perfect exchange section is easily found. The resulting development of some beam parameters over the exchange section is presented below and shows the exchange of the transverse emittances (Figures 6.2, 6.3),
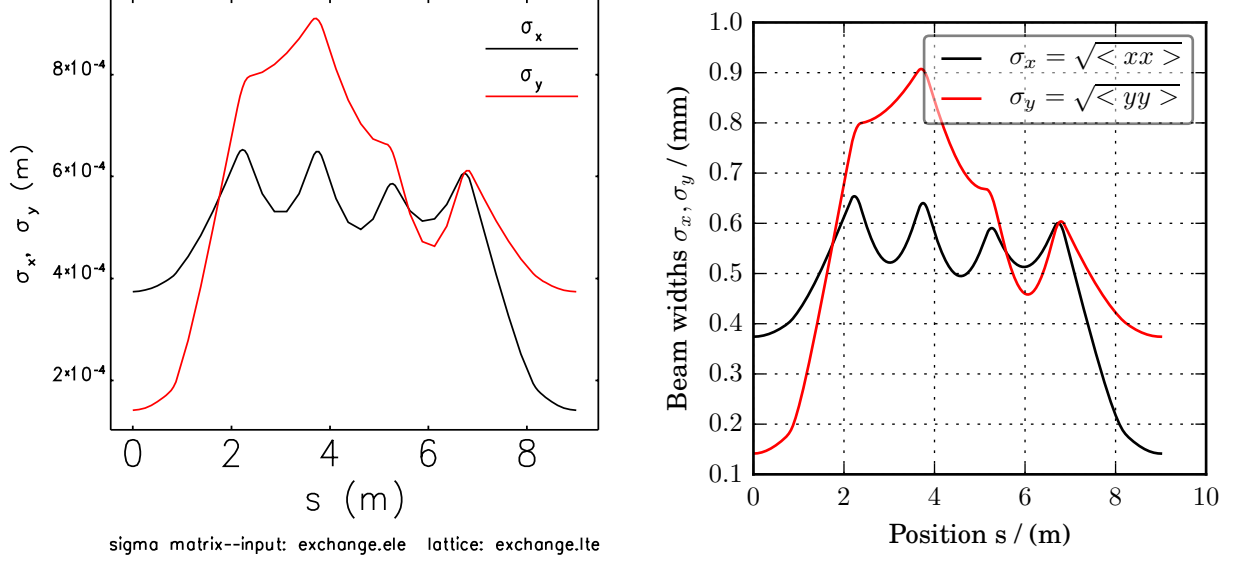
Figure 6.2.: Plot of the beam widths over the proposed emittance exchange section calculated with elegant (left) and ACCPY (right) show the exchange. [1,2,46]
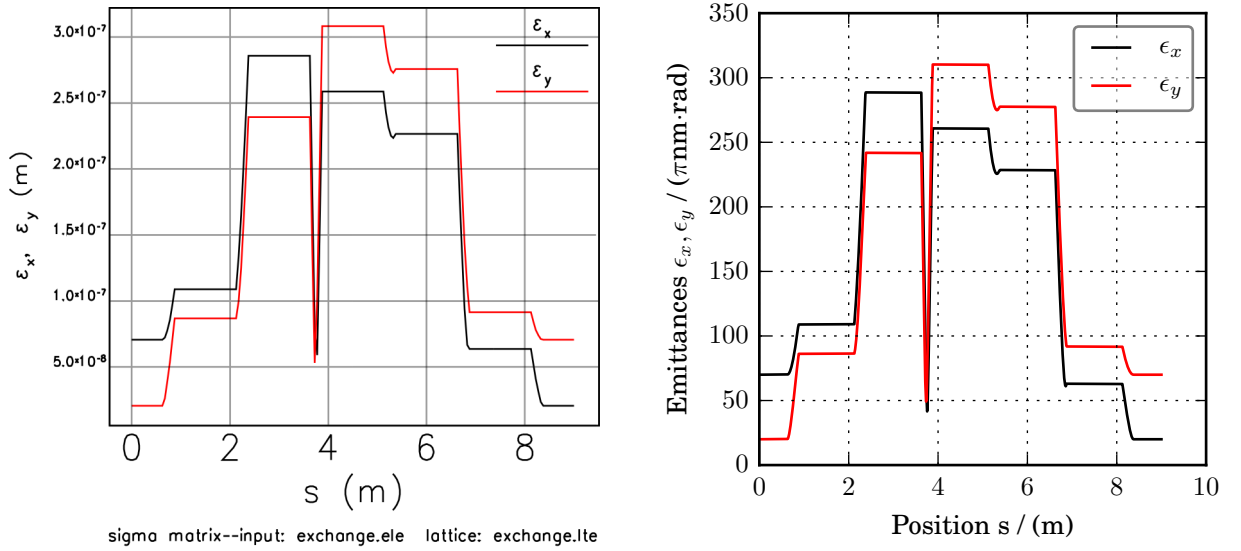
Figure 6.3.: Plot of the transverse emittances over the proposed emittance exchange section calculated with tracking in elegant (left) and from the beam matrix neglecting the coupling and thus non-zero coupling elements in ACCPY (right). These plots only show that the transverse emittances at the beginning and end of the exchange section are exchanged. The development in between is meaningless. [1,2,46]

One problem of making such an emittance exchange for the BESSY II transfer line is the rotation of the non-zero radial dispersion from the beginning of the emittance exchange section into the axial

plane at the end(Figure 6.4). The resulting axial dispersion cannot be sufficiently controlled with the available quadrupoles and makes an efficient injection into the storage ring impossible. The other problem with this long exchange region is the fact that there are too few quadrupole magnets left in order to match the transverse Twiss parameters to their values at the injection point in the storage ring[44]. Below the beta and dispersion functions over the BESSY II transfer line for the proposed emittance exchange section are illustrated. As said the shown curves over the emittance exchange section itself can be ignored as these neglect the coupling elements of the beam matrix.
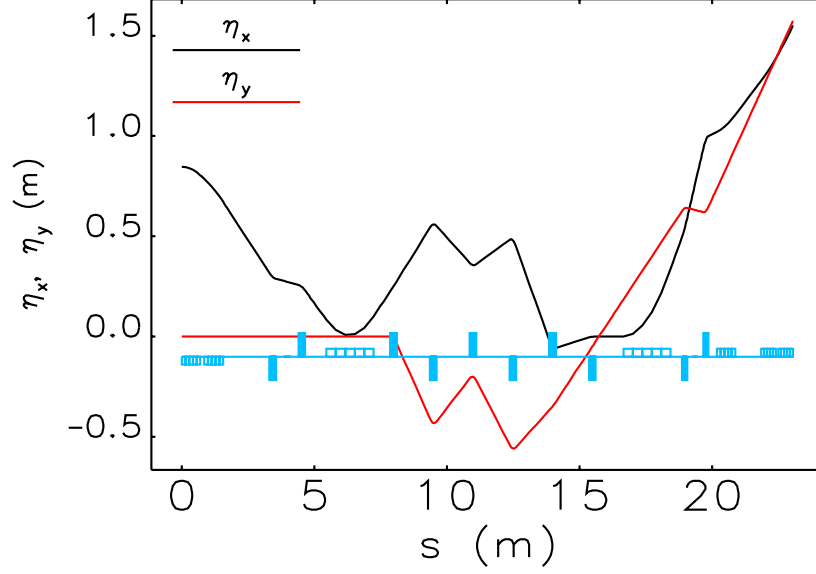

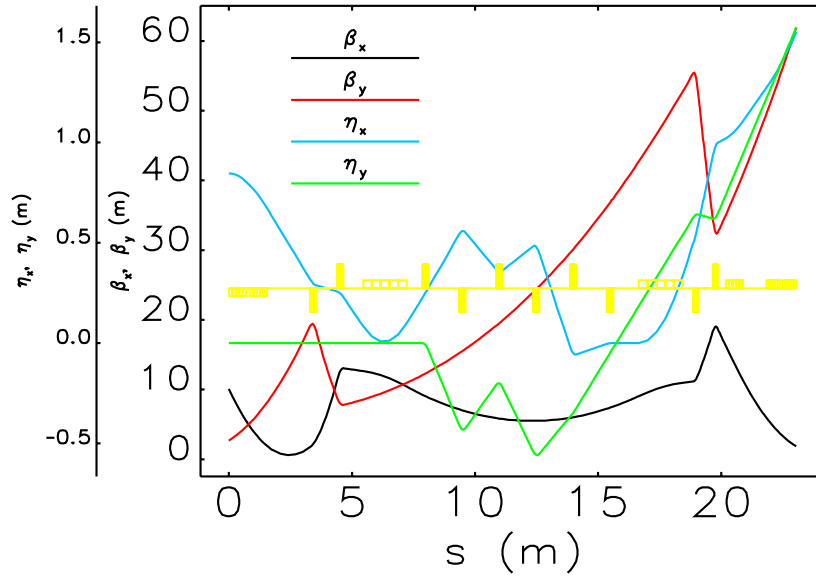Figure 6.4.: Radial and axial dispersion over the transfer line with the rotator quadrupole arrangement[46]

Figure 6.5.: Twiss functions over the transfer line optics with the presented skew quadrupole arrangement[46]

7. Conclusion

This work presents measurements and simulations on the emittance delivered to the BESSY II storage ring by the injector system. The results give evidence for and against the proposed linear optics of the injection and transfer lines. Furthermore, possibilities of transverse emittance optimization by exchange or sharing processes between the large radial and small axial emittance of the booster due to zero quantum excitation in the axial plane are presented. An example configuration of skew quadrupoles providing the possibility of a perfect emittance exchange in the transfer line is derived and corresponding simulation results are given.

The measurement of the beam emittance with quadrupole scans in the dispersion free first section of the injection line and the low dispersion region of the transfer line is described and results are given. The large uncertainties of the measured beam parameters when using this technique are very disappointing. With non-zero dispersion at the upstream quadrupole the errors are bigger than the fits already suggest. Still, the measured emittances in the dispersion free regions are in good agreement with previous results from others and give enough confidence to use these for the calibration of the dynamically measured emittance over the booster ramp. Also, the measured radial emittance with dispersion can be brought in agreement with the suspected values by small correction of the upstream derived dispersion taken from the linear optics simulation of the transfer line. The dynamic emittance during the energy ramp in the synchrotron is measured with a synchrotron radiation imaging system. The exact parameters of the optical system are unknown and derived by calibrating the measured axial emittance at extraction time to match that measured in the transfer line. The then measured emittance over the booster ramp is qualitatively in fair agreement with the simulated dynamic emittance using the measured emittance after the linac as initial condition.

The results of quadrupole scan measurements of this work indicate that the so far assumed transfer line optics is wrong. This is confirmed by the measurement of the dispersive trajectory. At this point the relation between quadrupole currents and gradients in the transfer line were reexamined based on old DANFYSIK magnet Field measurement reports. The results are new conversion factors which lead to a quite different optics. While the results of the measurement of the dispersive trajectories spoke for this optics, the quadrupole scan measurements exclude this optics as the betatron functions are too far off and the predicted dispersion function is incompatible to the measured beam widths.

In conclusion a fully understood transfer line optics is required in order to match parameters of the injected beam to those in the storage ring at the injection point. Then a moderate reduction of the transverse emittance can be achieved by emittance sharing in the booster. Alternatively, a fast ($\sim 2\,\mathrm{ms}$) crossing of the difference coupling resonance or an even faster ($\sim 2\,\mu\mathrm{s}$) excitation of the difference coupling resonance in the booster just before extraction of the beam can be used to realize a more complete transverse emittance exchange. A perfect emittance exchange could also be achieved in the transfer line with a set of 6 skew quadrupoles but only at the cost of introducing uncontrollable axial dispersion making this option uninteresting for the actual BESSY II transfer line.

A. Derivation of some formulas

A.1. Twisted ellipse and Twiss-Parameters

Ellipse with center in origin of Θ-twisted coordinate System $\tilde{x} - \tilde{x}'$:

$$\begin{pmatrix} \tilde{x} \\ \tilde{x}' \end{pmatrix} = \begin{pmatrix} a\cos\varphi \\ b\sin\varphi \end{pmatrix} \tag{A.1}$$

Matrix for rotating $\tilde{x} - \tilde{x}'$ by Θ:

$$R_\Theta = \begin{pmatrix} \cos\Theta & \sin\Theta \\ -\sin\Theta & \cos\Theta \end{pmatrix} \tag{A.2}$$

Gives twisted Ellipse in normal coordinate system :

$$\begin{pmatrix} x \\ x' \end{pmatrix} = R_\Theta \begin{pmatrix} \tilde{x} \\ \tilde{x}' \end{pmatrix} = \begin{pmatrix} a\cos\varphi\cos\Theta + b\sin\varphi\sin\Theta \\ -a\cos\varphi\sin\Theta + b\sin\varphi\cos\Theta \end{pmatrix} \tag{A.3}$$

The twiss-parameters α, β, γ can be identified from an equation

$$\epsilon = ab = f(x, x', a, b, \Theta) \tag{A.4}$$

which can be found by using a set of equivalent transformations:

$$\cos\varphi = \frac{x - b\sin\varphi\sin\Theta}{a\cos\Theta} \tag{A.5}$$

$$\sin\varphi = \frac{x - a\cos\varphi\cos\Theta}{b\sin\Theta} \tag{A.6}$$

$$\cos\varphi = -\frac{x' - b\sin\varphi\cos\Theta}{a\sin\Theta} \tag{A.7}$$

$$\sin\varphi = \frac{x' + a\cos\varphi\sin\Theta}{b\cos\Theta} \tag{A.8}$$

(A.5)-(A.7) leads to:

$$\begin{aligned}
0 &= \frac{x - b\sin\varphi\sin\Theta}{a\cos\Theta} + \frac{x' - b\sin\varphi\cos\Theta}{a\sin\Theta} \\
0 &= x\sin\Theta - b\sin\varphi\sin^2\Theta + x'\cos\Theta - b\sin\varphi\cos^2\Theta \\
0 &= x\sin\Theta + x'\cos\Theta - b\sin\varphi(\sin^2\Theta + \cos^2\Theta) \\
0 &= x\sin\Theta + x'\cos\Theta - b\sin\varphi
\end{aligned}$$

and so:

$$ab\sin\varphi = a(x\sin\Theta + x'\cos\Theta) \tag{A.9}$$

A. Derivation of some formulas

(A.6)-(A.8) leads to:

$$
\begin{aligned}
0 &= \frac{x - a\cos\varphi\cos\Theta}{b\sin\Theta} - \frac{x' + a\cos\varphi\sin\Theta}{b\cos\Theta} \\
0 &= x\cos\Theta - a\cos\varphi\cos^2\Theta - (x'\sin\Theta + a\cos\varphi\sin^2\Theta) \\
0 &= x\cos\Theta - x'\sin\Theta - a\cos\varphi(\cos^2\Theta + \sin^2\Theta) \\
0 &= x\cos\Theta - x'\sin\Theta - a\cos\varphi
\end{aligned}
$$

and so:

$$
ab\cos\varphi = b(x\cos\Theta - x'\sin\Theta) \tag{A.10}
$$

$(\text{A.9}^2)+(\text{A.10}^2)$ leads to:

$$
\begin{aligned}
a^2 b^2 &= a^2(x\sin\Theta + x'\cos\Theta)^2 + b^2(x\cos\Theta - x'\sin\Theta)^2 \\
a^2 b^2 &= a^2(x^2\sin^2\Theta + 2xx'\sin\Theta\cos\Theta\, x'^2\cos^2\Theta) + \\
&\quad + b^2(x^2\cos^2\Theta - 2xx'\cos\Theta\sin\Theta\, x'^2\sin^2\Theta) \\
ab &= \frac{a}{b}(x^2\sin^2\Theta + 2xx'\sin\Theta\cos\Theta\, x'^2\cos^2\Theta) + \\
&\quad + \frac{b}{a}(x^2\cos^2\Theta - 2xx'\cos\Theta\sin\Theta\, x'^2\sin^2\Theta)
\end{aligned}
$$

$$
\begin{aligned}
\epsilon &= x^2\left[\frac{a}{b}\sin^2\Theta + \frac{b}{a}\cos^2\Theta\right] \\
&\quad + 2xx'\left[\left(\frac{a}{b} - \frac{b}{a}\right)\sin\Theta\cos\Theta\right] + \\
&\quad + x'^2\left[\frac{a}{b}\cos^2\Theta + \frac{b}{a}\sin^2\Theta\right] \tag{A.11} \\
\epsilon &= x^2[\gamma] + 2xx'[\alpha] + x'^2[\beta] \tag{A.12}
\end{aligned}
$$

Resulting in:

$$
\beta = \left(\frac{a}{b} - \frac{b}{a}\right)(1 - \sin^2\Theta) + \frac{b}{a} \tag{A.13}
$$

$$
\gamma = \left(\frac{a}{b} - \frac{b}{a}\right)\sin^2\Theta + \frac{b}{a} \tag{A.14}
$$

$$
\alpha = \left(\frac{a}{b} - \frac{b}{a}\right)\sin\Theta\sqrt{1 - \sin^2\Theta} \tag{A.15}
$$

Test if $\gamma = \frac{1+\alpha^2}{\beta}$ is fulfilled:

$$
1 + \alpha^2 = \gamma\beta \tag{A.16}
$$

$$
\begin{aligned}
1 + \cancel{\left(\frac{a}{b} - \frac{b}{a}\right)^2 \sin^2\Theta(1 - \sin^2\Theta)} &= \cancel{\left(\frac{a}{b} - \frac{b}{a}\right)^2 \sin^2\Theta(1 - \sin^2\Theta)} + \\
&\quad + \frac{b}{a}\left(\frac{a}{b} - \frac{b}{a}\right)\sin^2\Theta + \\
&\quad + \frac{b}{a}\left(\frac{a}{b} - \frac{b}{a}\right)(1 - \sin^2\Theta) + \frac{b^2}{a^2} \\
1 &= \left(1 - \frac{b^2}{a^2}\right) + \frac{b^2}{a^2} = 1 \tag{A.17}
\end{aligned}
$$

Retrieving ellipse-parameters $a, b > 0$ from given twiss-parameters:

$$
\begin{aligned}
\beta + \gamma &= \frac{a}{b} + \frac{b}{a} \geq 2 = const. \\
\epsilon \cdot (\beta + \gamma) &= a^2 + b^2 \\
0 &= a^4 - \epsilon \cdot (\beta + \gamma)a^2 + \epsilon^2 \\
a, b &= \sqrt{\frac{\epsilon}{2}(\beta + \gamma \pm \sqrt{(\beta + \gamma)^2 - 4})}
\end{aligned}
$$

(A.18)

(A.19)

Finally one gets the angle of rotation Θ from (A.13):

$$
for \quad \alpha \quad > \quad 0 : \quad \Theta = \arccos\left(+\sqrt{\frac{\beta - (\beta - \frac{b}{a})\,\epsilon}{a^2 - b^2}} \right)
$$

(A.20)

$$
for \quad \alpha \quad < \quad 0 : \quad \Theta = \arccos\left(-\sqrt{\frac{\beta - (\beta - \frac{b}{a})\,\epsilon}{a^2 - b^2}} \right)
$$

(A.21)

A.2. Relativistic kinematics

The well known mass–energy equivalence formulated by Albert Einstein gives:

$$
E = mc^2 = m_0\gamma c^2 = E_0\gamma
$$

(A.22)

with the Lorentz factor

$$
\gamma = \frac{E}{E_0} = \frac{E_{kin}}{E_0} + 1 = \frac{1}{\sqrt{1 - \frac{v^2}{c^2}}} = \frac{1}{\sqrt{1 - \beta^2}}.
$$

(A.23)

Now the relativistic momentum can be derived to:

$$
p = mv = m_0\gamma v
$$

(A.24)

$$
\rightarrow \frac{p^2}{c^2} = \frac{m_0^2 v^2}{c^2\left(1 - \frac{v^2}{c^2}\right)}.
$$

(A.25)

With some rearrangement we can find

$$
\frac{v^2}{c^2} = \frac{p^2}{m_0^2 c^2 + p^2}.
$$

(A.26)

By inserting equation A.26 into A.23 and that into $(A.22)^2$ we get a velocity independant expression for the relativistic energy:

$$
\boxed{E^2 = m_0^2 c^4 + p^2 c^2.}
$$

(A.27)

We can also rearrange the lorentz factor equation A.23 for the velocity:

$$
\gamma^2 = \frac{1}{1 - \frac{v^2}{c^2}}
$$

(A.28)

$$
\rightarrow v^2 = c^2\left(1 - \frac{1}{\gamma^2}\right) = c^2\left(1 - \frac{E_0^2}{E^2}\right)
$$

(A.29)

and from equation A.26 we can derive lorentzbeta as

$$\beta = \frac{v}{c} = \frac{p}{\sqrt{m_0^2 c^2 + p^2}} = \frac{pc}{\sqrt{m_0^2 c^4 + p^2 c^2}} = \frac{pc}{E}. \tag{A.30}$$

Finally we can show that for relativistic speeds the following holds:

$$\frac{\Delta v}{v} \approx \frac{1}{\gamma^2} \frac{\Delta p}{p} = \frac{1}{\gamma^2} \delta. \tag{A.31}$$

With equation A.29 and $\gamma = (\delta + 1)\gamma_0$ we can write:

$$\frac{\Delta v}{v} = \frac{v - v_0}{v_0} = \frac{v}{v_0} - 1 = \sqrt{\frac{1 - \frac{1}{\gamma^2}}{1 - \frac{1}{\gamma_0^2}}} - 1 \tag{A.32}$$

$$= \sqrt{\frac{1 - \frac{1}{\gamma_0^2 (\delta+1)^2}}{1 - \frac{1}{\gamma_0^2}}} - 1 \tag{A.33}$$

$$= \sqrt{\frac{\gamma_0^2 - \frac{1}{(\delta+1)^2}}{\gamma_0^2 - 1}} - 1 \tag{A.34}$$

The series expansion of the square root in equation A.34 around $\delta \approx 0$ gives:

$$\sqrt{\frac{\gamma_0^2 - \frac{1}{(\delta+1)^2}}{\gamma_0^2 - 1}} \approx 1 + \frac{\delta}{\gamma^2 - 1} + \dots \tag{A.35}$$

Inserting the linear (in δ) series approximation in equation A.34 we get:

$$\frac{\Delta v}{v} = \frac{\delta}{\gamma^2 - 1} \tag{A.36}$$

For relativistic particles we can further neglect subtracting 1 from γ^2 in the denominator and get our wanted equation:

$$\boxed{\frac{\Delta v}{v} \approx \frac{1}{\gamma^2} \delta.} \tag{A.37}$$

A.3. Quantum excitation

$$P_\gamma = \frac{q^2 c}{6\pi\epsilon_0} \frac{\gamma^4}{R^2} = \frac{cC_\gamma}{2\pi} \frac{E^4}{R^2} \tag{A.38}$$

$$\langle dp_\gamma \rangle = \langle \hbar\omega \rangle = \frac{8}{15\sqrt{3}} \hbar\omega_c \tag{A.39}$$

$$\langle dp_\gamma^2 \rangle = \langle (\hbar\omega)^2 \rangle = \frac{11}{27} (\hbar\omega_c)^2 \tag{A.40}$$

$$\dot{N}_\gamma = \frac{P_\gamma}{\langle dp_\gamma \rangle} = \frac{15\sqrt{3}}{8\hbar\omega_c} P_\gamma \tag{A.41}$$

$$\dot{N}_\gamma \langle dp_\gamma^2 \rangle = \frac{55\hbar\omega_c}{24\sqrt{3}} P_\gamma = \frac{55\hbar\omega_c}{24\sqrt{3}} \frac{cC_\gamma}{2\pi} \frac{E^4}{R^2} \tag{A.42}$$

$$(1) = \tag{A.43}$$

$$= \boxed{\frac{55\hbar^2 c^3}{24\sqrt{3}} \alpha \frac{\gamma^7}{R^3} \quad \text{with} \quad \alpha = \frac{e^2}{4\pi\epsilon_0\hbar}} \tag{A.44}$$

$$(2) = \frac{55\hbar\omega_c}{24\sqrt{3}} 2C_\alpha \frac{E^4}{R^2} \tag{A.45}$$

$$= \frac{55\hbar c}{32\sqrt{3}E_0} \frac{2C_\alpha E^4}{R^2} \tag{A.46}$$

$$= \frac{55\hbar c}{32\sqrt{3}E_0} \frac{2C_\alpha E^4}{R^2} \tag{A.47}$$

$$= \boxed{\frac{4C_q C_\alpha}{R^3} \gamma^2 E^5 \quad \text{with} \quad C_q = \frac{55\hbar c}{32\sqrt{3}E_0}} \tag{A.48}$$

$$\langle \Delta E^2 \rangle = \frac{1}{2C} \oint \dot{N}_\gamma \langle dp_\gamma^2 \rangle \, ds \tag{A.49}$$

$$= \frac{1}{2C} \oint \frac{P_\gamma}{\langle dp_\gamma \rangle} \langle dp_\gamma^2 \rangle \, ds \tag{A.50}$$

$$q_x(t)\epsilon_x(t) = \frac{2C_q C_a}{R^2} \gamma(t)^2 E(t)^3 \frac{\mathcal{I}_{5x}}{\mathcal{I}_2} \tag{A.51}$$

$$q_y(t)\epsilon_s(t) = \left(\frac{\sigma_e}{E}\right)^2 = \frac{2C_q C_a}{R^2} \gamma(t)^2 E(t)^3 \frac{\mathcal{I}_3}{\mathcal{I}_2} \tag{A.52}$$

B. Additional simulations

Simulating the linear beam optics of an accelerator is often required. Before using one of the many available simulation programs an own approach should be made. Matlab - being an easy to use and powerful numerical computing environment was initially used. Especially as all computational physics lessons at the Humboldt University where on Matlab. Due to licence and compatibility problems as well as missing toolboxes for Matlab on the BESSY II control system it soon became clear that Python is the better way to go. Python gives greater flexibility and comparable performance at the cost of a little more syntax complexity. Therefore written code for simulations and measurements was soon transferred from Matlab to Python as ACCPY. For comparison and credibility the results of two common simulation programs: MAD-X (Methodical Accelerator Design) from CERN and Elegant (ELEctron Generation ANd Tracking) from the Argonne National Laboratory are presented here.
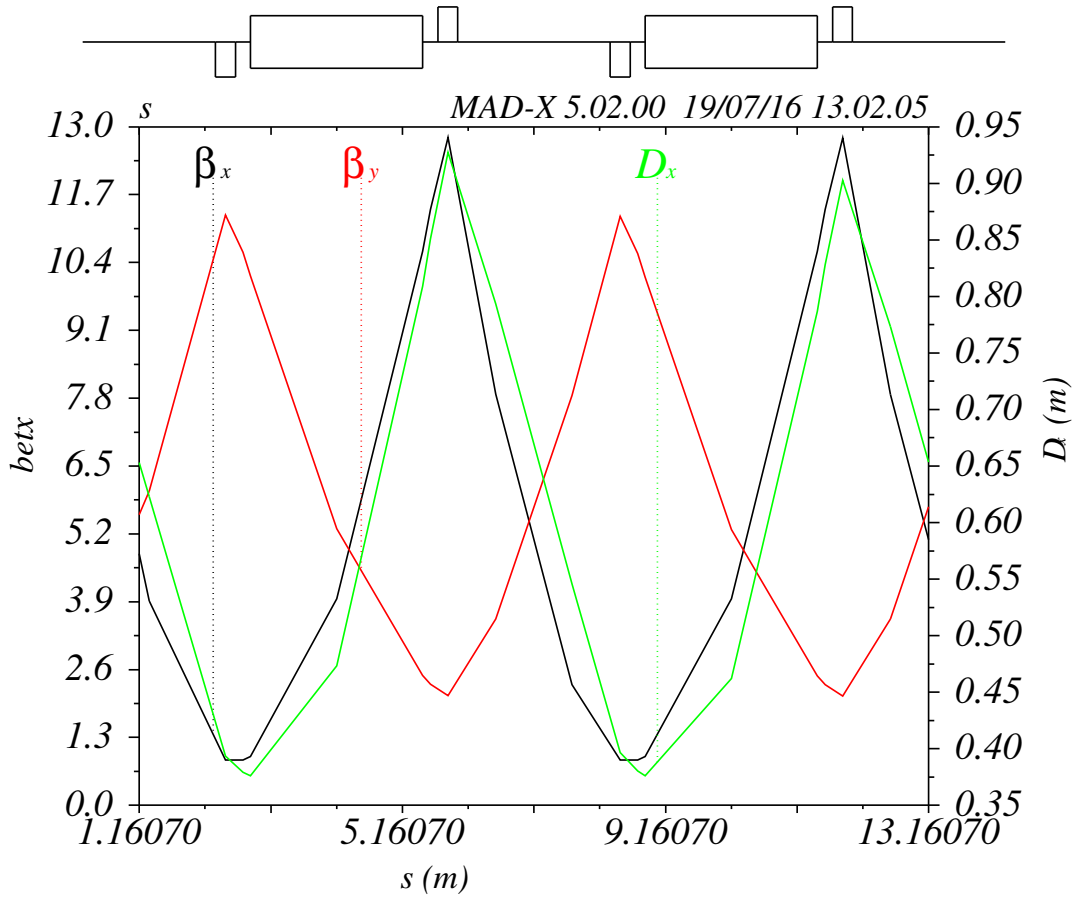
B.1. MAD-X

Figure B.1.: Calculated beta- and dispersion functions over the booster unit cell [47]

```
1  !!=============================================================
2      TITLE, s='MAD-X vs BESSY II booster';
3  !! Author Felix Kramer
4  !!=============================================================
5  !! options
6      option, -echo,-warn,-info;
7      assign, ECHO=echo.dat;
8
9  !! ring parameters
10     circumference = 96;
11     ncell   = 8;
12
13 !! cavity
14     CAV: RFCAVITY, L  = 0.3,
15                   VOLT = 0.75,
16                   HARMON = 160,
17                   LAG = pi+0.08;
18
19 !! drifts
20     D1:drift, L = 1.160;
21     D2:drift, L = 0.23;
22     D3:drift, L = 1.1607;
23     D4:drift, L = 2.0214;
24
25 !! dipoles
26     lbend   = 2.6193;
27     bendangle = pi/ncell;
28     bendradius = ncell*lbend/pi;
29     edgeangle = lbend/(2*bendradius);
30     BSB:sbend,   L = lbend,
31                   ANGLE = bendangle;
32     EDGE:dipedge,  h = 1/bendradius,
33                   E1 = edgeangle,
34                   hgap=0.015,
35                   fint=1/2;
36     B:line = (EDGE,BSB,EDGE);
37
38 !! quadrupoles
39     lquad   = .3;
40     kqf     = +2.1082;
41     kqd     = -1.4658;
42     QF:quadrupole, L = lquad, K1 = kqf;
43     QD:quadrupole, L = lquad, K1 = kqd;
44
45 !! unit cell and ring
46     UC :LINE = (D3,D3,QD,D2,B,D2,QF,D1,D1,QD,D2,B,D2,QF);
47     CC :LINE = (CAV,D4,QD,D2,B,D2,QF,D1,D1,QD,D2,B,D2,QF);
48     RING :LINE = (CC,UC,UC,UC,UC,UC,UC,UC);
49
50 !! beam properties
51     beam,  particle  = electron,
52            energy  = 1.72,
53            sige  = 5.7e-4, // energy spread
54            sigt  = 6.5e-11, // bunch length
55            radiate  = true;
56
57 !! activate the sequence with defined beam
58     use, sequence = ring;
59
60 !! output specifications
61     twiss, chrom,centre,rmatrix ,file=twiss.out;
62     PLOT,  HAXIS = S, HMIN = 1.1607, HMAX = 13.1607,
63            VAXIS1 = BETX, BETY,
64            VAXIS2 = DX,
65            COLOUR = 100;
66     EMIT, DELTAP=0; //.7e-4;
```

Listing B.1: MAD-X input file

B.2. Elegant
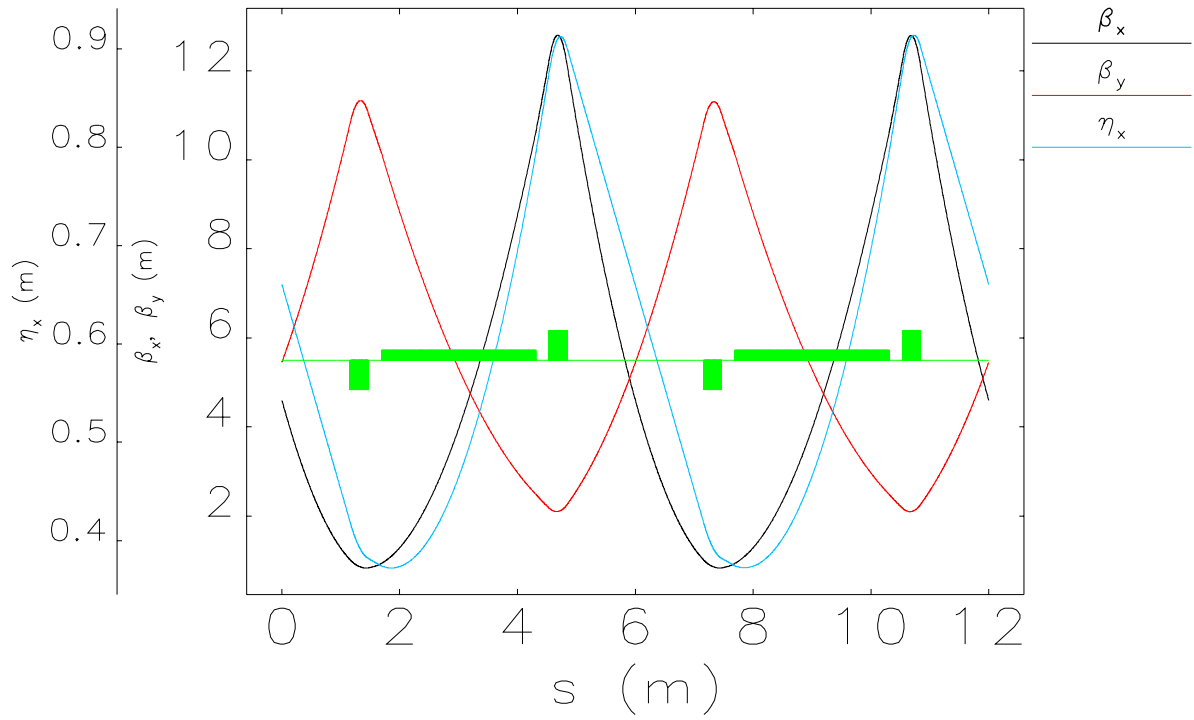
Figure B.2.: Calculated beta- and dispersion functions over the booster unit cell[46]

The plot was created with sddsplot:

sddsplot -graphic=line,vary booster.twi -col=s,beta? -yScalesGroup=id=beta -legend
-limit=xmin=0,xmax=12 -col=s,etax -yScalesGroup=id=eta -legend -limit=xmin=0,xmax=12
-col=s,Profile -limit=xmin=0,xmax=12 booster.mag -overlay=xmode=norm,yoffset=-.1,yfactor=0.1

The parameters are taken with sddsprintout:

sddsprintout -par=betaxMax,betayMax,etaxMax,nux,nuy,dnux/dp,dnuy/dp,ex0,taux,tauy,taudelta,
Sdelta0,alphac,U0,endsline booster.twi

```
1  !!=======================================================================
2  !! ELEGANT  BESSY II Booster --lattice--
3  !! Author Felix Kramer
4  !!=======================================================================
5  D1:drif, L=1.160
6  D2:drif, L=0.23
7  D3:drif, L=1.1607
8
9  QF:quad, L=0.3, K1=+2.1082
10 QD:quad, L=0.3, K1=-1.4658
11
12 B: csbend, L=2.6193, ANGLE=0.39269908169872414, E1=0.196349540849, E2
      =0.196349540849, HGAP=0.018, Fint=0.7
13
14 UC  :LINE = (D3,QD,D2,B,D2,QF,D1,D1,QD,D2,B,D2,QF,D3)
15 RING :LINE = (UC,UC,UC,UC,UC,UC,UC,UC)
```

Listing B.2: elegant lattice file

```
1  !!=======================================================================
2  !! ELEGANT  BESSY II Booster --run options--
3  !! Author Felix Kramer
4  !!=======================================================================
5  &run_setup
6     lattice = "b2booster.lte"
7     use_beamline = "ring",
8     p_central_mev = 1720,
9     output = %s.out,
10    magnets = "%s.mag",
11    element_divisions = 1000,
12    sigma = "%s.sig"
13 &end
14
15 ! request output of Twiss parameters
16 &twiss_output
17    filename = "%s.twi",
18    radiation_integrals = 1
19 &end
```

Listing B.3: elegant run file

B.3. Comparison

Physical quantity @Energy	Unit	ACCPY 1.72 GeV	MAD-X 1.72 GeV	Elegant 1.72 GeV	Measurement 1.72 GeV
$\beta_{x,max}$	m	12.799	12.8015	12.7859	/
$\beta_{y,max}$	m	11.3283	11.3157	11.3277	/
$D_{x,max}$	m	0.9138	0.9272	0.9137	/
Q_x		5.9045	5.9044	5.9045	5.89
Q_y		3.3772	3.3801	3.3772	3.39
$\xi_{x,nat}$		-9.6469	-9.6067	-8.8847	-9
$\xi_{y,nat}$		-4.5411	-4.7539	-4.8511	-5
ξ_x		/	/	/	-0.8
ξ_y		/	/	/	-4
ϵ_x	nm rad	73.186	67.779	66.734	/
τ_x	ms	5.1335	5.1999	4.6838	/
τ_y	ms	4.7449	4.7449	4.7449	/
τ_s	ms	2.2859	2.2730	2.3881	/
δ_E	‰	0.56	0.57	0.57	/
σ_τ	ps	58.9	65	/	/
α_p		0.0330	0.0330	0.0330	/
γ_{tr}		5.5009	5.5009	/	/
$E_{radiation}$	keV	116.078	116.078	116.078	/
λ_c	nm	0.73198	/	/	/

Table B.1.: Comparison of ACCPY, MAD-X and Elegant results for the BESSY II booster with main parameters at extraction (t=38192μs , E=1.72 GeV).[1,46,47]

The results are in good agreement with one another. The damping times are given in correspondence to the betatron and synchrotron oscillations and have to be multiplied by 2 in order to get the

emittance damping times.

B.4. BESSY II Booster parameters

Quantity	Symbol	Value	Unit
Circumference	C	96	m
Number of cells	N	16	
Repetition rate	f_{rep}	10	Hz
RF-frequency	f_{RF}	499.65	MHz
Harmonic number	h	160	
Revolutiontime	T_{rev}	320.22	ns
Momentum compaction factor	α_γ	0.033	
Maximum energy	E_{max}	1.9	GeV
Extraction energy	E_{ext}	1.72	GeV
Injection energy	E_{inj}	50	MeV
Maximum field	B_{max}	0.95	T
Extraction field	B_{ext}	0.86	T
Injection field	B_{inj}	0.025	T
Maximum time	t_{max}	47 634	μs
Extraction time	t_{ext}	38 192	μs
Injection time	t_{inj}	5 229	μs
Radial tune	Q_x	5.90	
Axial tune	Q_y	3.38	
Nat. chromaticities	ξ_x, ξ_y	-9.6/-4.5	
Damping times	τ_x, τ_y, τ_s	5.1/4.7/2.3	ms
Energyspread @E_{ext}	δ	0.56	‰

Table B.2.: General parameters for the BESSY II booster.[1]

Magnets	Amount	Length	Field@E_max	Gap	Radius
Dipoles	16	2619.3 mm	.95 T	36	6670 mm
Quadrupoles	32	300 mm	14 T/m	35	∞
Sextupoles	16	162 mm	70 T/m^2	35	∞

Table B.3.: Parameters of the BESSY II booster magnets.[24]

B.5. BESSY II 240 m circumference booster ramp
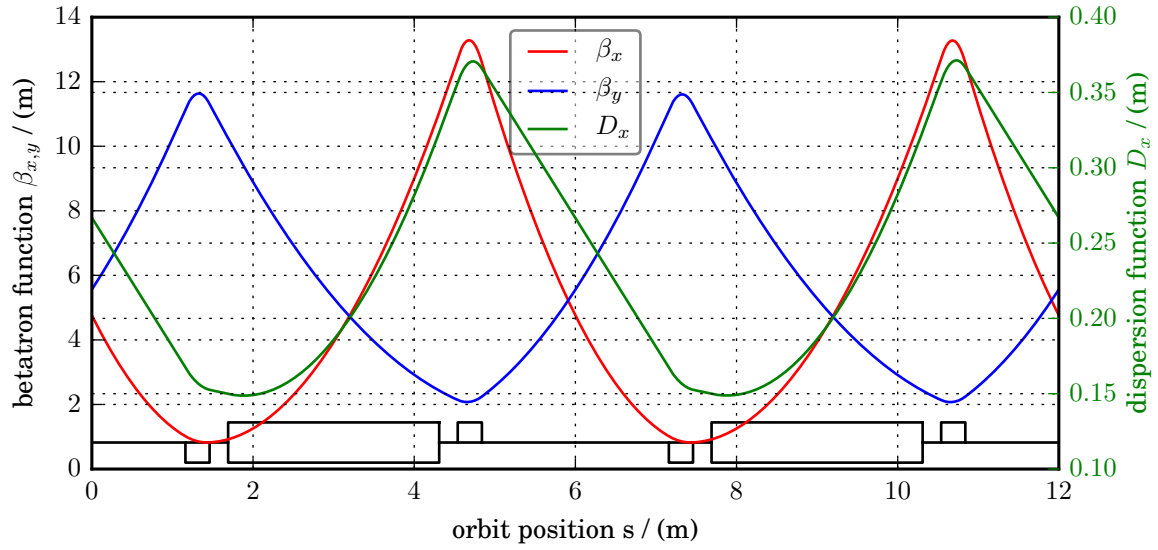
Radial parameters

$\beta_{x,max} = 13.2833\ m$
$\beta_{x,min} = 0.821252\ m$
$\alpha_{x,max} = 4.25682$
$\alpha_{x,min} = -3.81353$
$\gamma_{x,max} = 1.51809$
$\gamma_{x,min} = 0.0752827$
$D_{x,max} = 0.371294\ m$
$D_{x,min} = 0.148708\ m$
$D'_{x,max} = 0.14545$
$D'_{x,min} = -0.0858882$
$Q_x = 14.7612$
$\xi_{x,nat} = -24.8687$
$J_x = 0.987843$
$\epsilon_x = 4.41236e - 09\ \pi m \cdot rad$
$\tau_x = 3.002079e - 02\ s$

Axial parameters

$\beta_{y,max} = 11.6333\ m$
$\beta_{y,min} = 2.07224\ m$
$\alpha_{y,max} = 2.37846$
$\alpha_{y,min} = -2.89416$
$\gamma_{x,max} = 0.841084$
$\gamma_{x,min} = 0.0859601$
$Q_y = 8.44451$
$\xi_{y,nat} = -12.8135$
$J_y = 1$
$\epsilon_y = 7.24583e - 14\ \pi m \cdot rad$
$\tau_y = 2.965583e - 02 s$

Longitudinal parameters

$E = 1.72e + 09\ eV$
$\gamma_{lorentz} = 3366.96$
$\alpha_p = 0.00530701$
$\eta_{slip} = 0.00530692$
$\gamma_{tr} = 13.727$
$Q_s = 0.0171651$
$J_s = 2.01216$
$\sigma_\delta = 3.598182e - 02\ \%$
$\sigma_\tau = 1.41739e - 11\ s$
$\sigma_s = 0.00424924\ m$
$\tau_s = 1.473833e - 02\ s$
$E_{loss} = 46431.1\ eV$
$P_{rad} = 232.155\ W$
$E_{crit} = 677.524\ eV$
$\lambda_{crit} = 1.82996e - 09\ m$

Figure B.3.: Overview of Twiss functions of over 2.5 times bigger booster ($C_{bigbooster} = C_{sr} = 240\,\mathrm{m}$) with optics adjusted to have 2.5 times bigger tune so that in theory it should be able to replace existing booster without difficulty. [1,26]
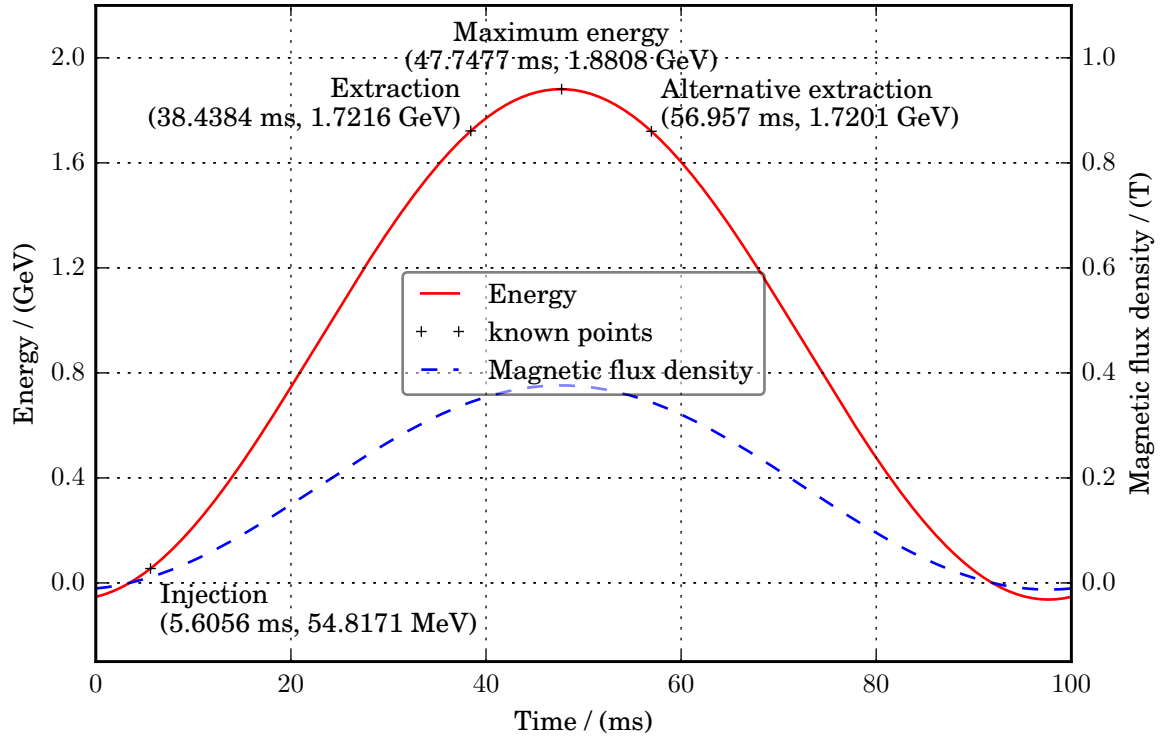
Figure B.4.: Particle energy and magnetic flux density in dipoles in the big booster [1,2]
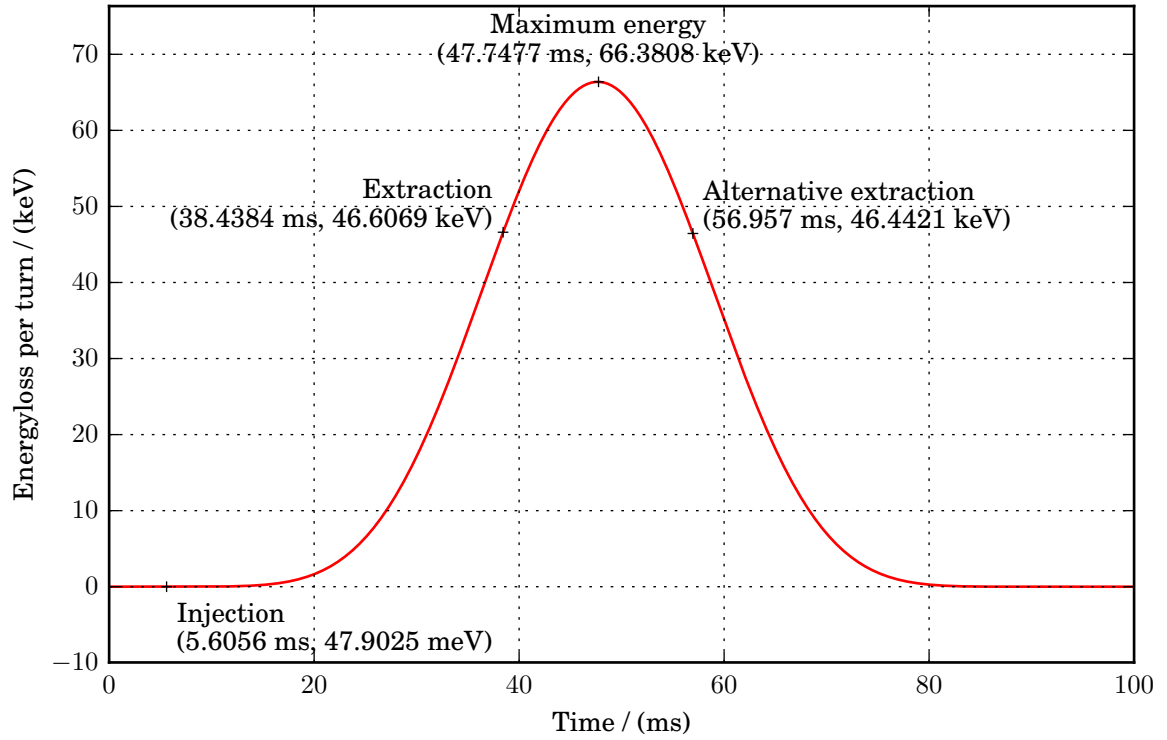
Figure B.5.: Energy loss per turn due to synchrotron radiation in the big booster [1,2]
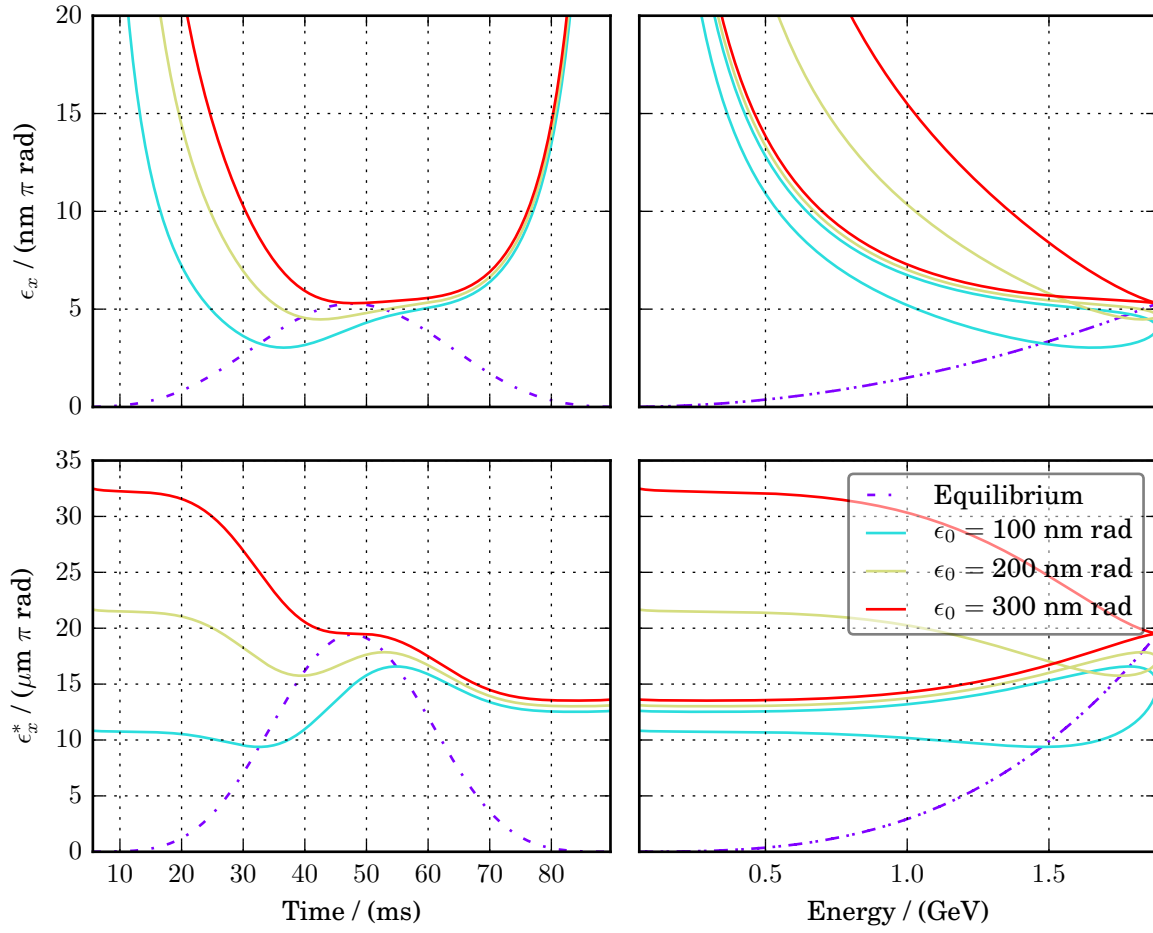
Figure B.6.: Development of the dynamic (for different initial ϵ_x) and equilibrium radial emittance over time (left side) and energy (right side) and the corresponding normalized emittances (below) for the big booster. [1,2]
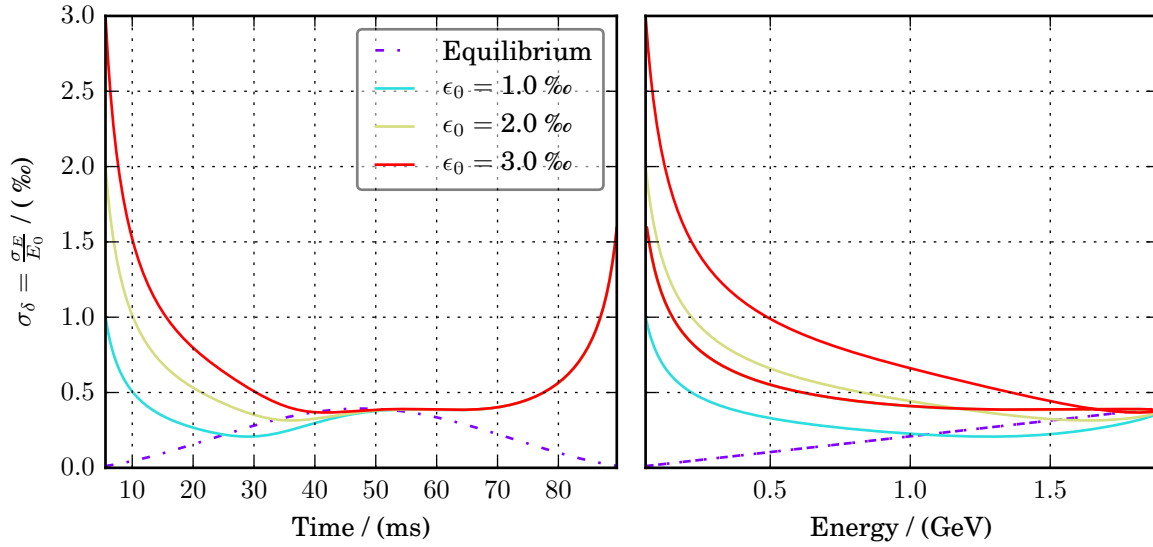

Figure B.7.: Development of the dynamic (for different initial $\sigma_{\delta,0}$) and equilibrium energy spread over time (left side) and energy (right side) for the big booster. [1,2]
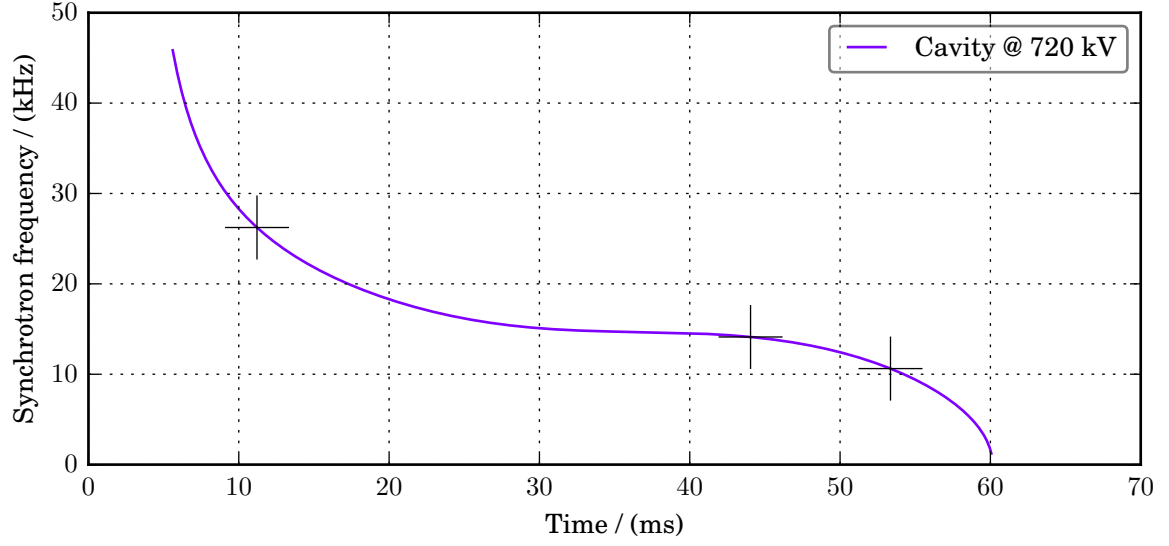
Figure B.8.: The simulated synchrotron frequency over the big booster ramp with markers at the injection, extraction and peak energy of the booster ramp.[1,2]
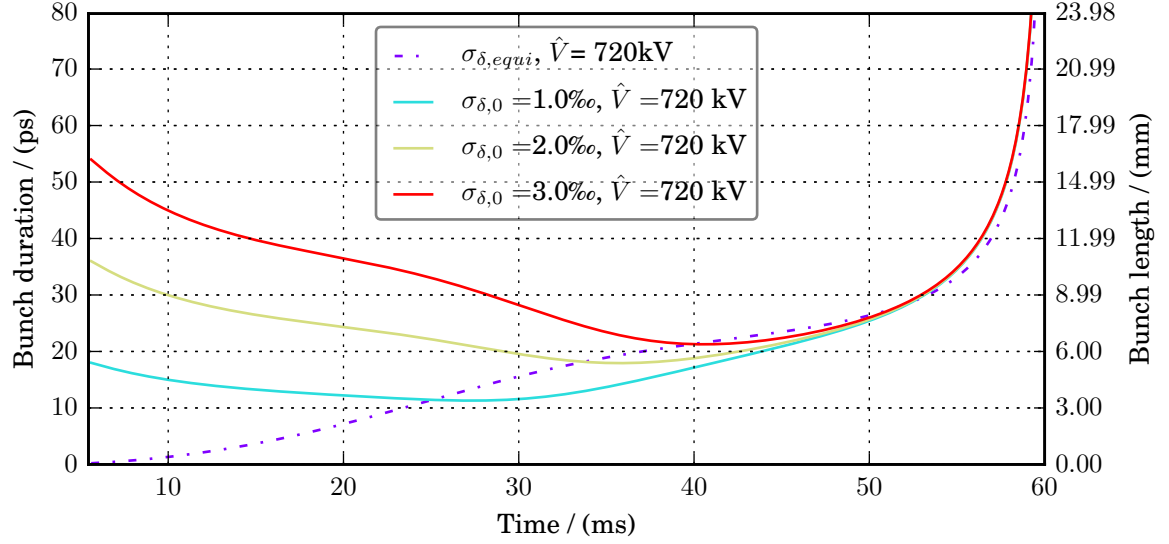
Figure B.9.: The bunch lengths calculated from the simulated dynamic (for different initial $\sigma_{\delta,0}$) and equilibrium energy spreads for the simulated synchrotron frequency over the big booster ramp.[1,2]

C. Code

The code written for the simulations and measurements of this work is mostly part of ACCPY and available at https://github.com/kramerfelix/accpy. As the code in total exceeds 11 thousand lines it is not printed here. All code is available by contactig the author (felix.kramer@physik.hu-berlin.de).

Bibliography

[1] F. Kramer, "ACCPY: Python module with GUI providing simmulation, measurement and optimization capabilities for accelerators," 2016. [Online]. Available: https://github.com/kramerfelix/accpy

[2] J. D. Hunter, "Matplotlib: A 2D graphics environment," *Computing In Science & Engineering*, vol. 9, no. 3, pp. 90–95, 2007.

[3] E. Jones, T. Oliphant, P. Peterson *et al.*, "SciPy: Open source scientific tools for Python," 2001–, [Online; accessed 2016-08-30]. [Online]. Available: http://www.scipy.org/

[4] S. v. d. Walt, S. C. Colbert, and G. Varoquaux, "The numpy array: A structure for efficient numerical computation," *Computing in Science and Engg.*, vol. 13, no. 2, pp. 22–30, Mar. 2011. [Online]. Available: http://dx.doi.org/10.1109/MCSE.2011.37

[5] M. Newville, T. Stensitzki, D. B. Allen, and A. Ingargiola, "LMFIT: Non-Linear Least-Square Minimization and Curve-Fitting for Python," 2014. [Online]. Available: http://dx.doi.org/10.5281/zenodo.11813

[6] Andrew Collette, "HDF5 for Python," 2008. [Online]. Available: http://h5py.alfven.org

[7] T. Tantau, "TikZ and PGF - Manual for Version 3.0.0," 2013. [Online]. Available: http://sourceforge.net/projects/pgf

[8] W. Kühnel, *Differentialgeometrie - Kurven - Flächen - Mannigfaltikeiten*, 6th ed. Berlin, Boston: Springer Spektrum, 2013.

[9] F. Hinterberger, *Physik der Teilchenbeschleuniger: und Ionenoptik*, 2nd ed. Berlin, Heidelberg: Springer, 1997.

[10] K. Wille, *Physik der Teilchenbeschleuniger und Synchrotronstrahlungsquellen*, 2nd ed. Stuttgart: Teubner, 1996.

[11] A. Chao, *Handbook of Accelerator Physics and Engineering*, 3rd ed. Singapore: World Scientific, 2009.

[12] J. D. Jackson, *Klassische Elektrodynamik*, 5th ed. Berlin, Boston: DE GRUYTER, 2006.

[13] R. H. Helm, P. Morton, M. J. Lee, and M. Sands, "EVALUATION OF SYNCHROTRON RADIATION INTEGRALS," *IEEE Trans. Nucl. Sci.*, vol. 20, no. SLAC-PUB-1193, pp. 900–901, 1973.

[14] G. Hemmie and M. Leneke, "REDUCTION OF THE HORIZONTAL ANTIDAMPING IN THE DESY ELECTRON SYNCHROTRON," in *Proc. of Particle Accelerator Conference (PAC'81), Washington, D.C., USA, March 11-13, 1981*, ser. Particle Accelerator Conference, no. 9. Geneva, Switzerland: JACoW, 1981, paper DESY-M-81-14, pp. 2546–2548. [Online]. Available: http://accelconf.web.cern.ch/accelconf/p81/PDF/PAC1981_2546.PDF

[15] A. Wolski, *Beam Dynamics in High Energy Particle Accelerators*, 1st ed.   Singapore: World Scientific, 2014.

[16] H. Wiedemann, *Particle Accelerator Physics*, 3rd ed.   Berlin, Heidelberg: Springer, 2007.

[17] M. Minty, "DIAGNOSTICS I-III," *CERN Accelerator School*, September 2004.

[18] Ruprecht, Martin, "CALCULATION OF COUPLED BUNCH EFFECTS IN THE SYSNCHROTRON LIGHT SOURCE BESSY VSR," Doctoral Thesis, Humboldt-Universität zu Berlin, 2016.

[19] Astrid Brandt, Thomas Gutberlet, Nils Leidel, Florian Staier, and Antje Vollmer, "EXPERIMENTAL FACILITIES AT BESSY II AND BER II," Helmholtz-Zentrum Berlin fur Materialien und Energie GmbH (HZB).

[20] V. Duerr *et al.*, "COMMISSIONING OF THE 50 MeV PREINJECTOR LINAC FOR THE BESSY II FACILITY," in *Proc. of International Particle Accelerator Conference (IPAC'11), San Sebastian, Spain, September 4-9, 2011*, ser. International Particle Accelerator Conference, no. 2. Geneva, Switzerland: JACoW, 2011, paper THPC108, pp. 3140–3142. [Online]. Available: http://accelconf.web.cern.ch/AccelConf/IPAC2011/papers/thpc108.pdf

[21] T. Atkinson *et al.*, "STATUS AND PROSPECTS OF THE BESSY II INJECTOR SYSTEM," in *Proc. of International Particle Accelerator Conference (IPAC'16), Busan, Korea, May 8-13, 2016*, ser. International Particle Accelerator Conference, no. 7.   Geneva, Switzerland: JACoW, June 2016, paper WEPOW007, pp. 2826–2828, doi:10.18429/JACoW-IPAC2016-WEPOW007. [Online]. Available: http://jacow.org/ipac2016/papers/wepow007.pdf

[22] A. Setty, J-L. Pastre, D. Jousse, and E. Weihreter, "BEAM DYNAMICS OF THE 50 MeV PREINJECTOR FOR THE BERLIN SYNCHROTRON BESSY II," in *Proc. of International Particle Accelerator Conference (IPAC'10), Kyoto, Japan, May 23-28, 2010*, ser. International Particle Accelerator Conference, no. 1.   Geneva, Switzerland: JACoW, 2010, paper WEPEA009, pp. 2490–2492. [Online]. Available: http://accelconf.web.cern.ch/accelconf/IPAC10/papers/wepea009.pdf

[23] M. Abo-Bakr, W. Anders, V. Dürr, D. Krämer, B. Kuske, P. Kuske, M. Martin, R. Müller, T. Schneegans, G. Wüstefeld, E. Weihreter, , R. Bakker, T. Birke, K. Bürkmann, W. Gericke, M. v. Hartrott, K. Ott, and J. Rahn, "COMMISSIONING OF THE BESSY II BOOSTER SYNCHROTRON," in *Proc. of European Particle Accelerator Conference (EPAC'98), Stockholm, Sweden, June 22-26, 1998*, ser. European Particle Accelerator Conference, no. 6. Geneva, Switzerland: JACoW, 1998, paper WEP30G, pp. 436–438. [Online]. Available: http://accelconf.web.cern.ch/AccelConf/e98/PAPERS/WEP30G.PDF

[24] D. Krämer, B. Kuske, D.Schirmer, G. Wüstefeld, J. Bahrdt, M. Martin, K. Bürkmann, L. Schulz, W. Anders, R. v. Hahn, P. Kuske, R. Müller, J. Rahn, E. Weihreter, M. v. Hartrott, and H. Prange, "THE BESSY II PARAMETER LIST," BESSY II, 1995.

[25] K. Bürkmann, G. Schindhelm, and T. Schneegans, "PERFORMANCE OF THE WHITE CIRCUITS OF THE BESSY II BOOSTER SYNCHROTRON," in *Proc. of European Particle Accelerator Conference (EPAC'98), Stockholm, Sweden, June 22-26, 1998*, ser. European Particle Accelerator Conference, no. 6.   Geneva, Switzerland: JACoW, 1998, paper TUP11C,

pp. 2062–2064. [Online]. Available:
http://accelconf.web.cern.ch/AccelConf/e98/PAPERS/TUP11C.pdf

[26] F. Kramer, "DYNAMISCHE MESSUNG DES ARBEITSPUNKTES SOWIE DER
CHROMATIZITÄT WÄHREND DES BESCHLEUNIGUNGSPROZESSES AM
BOOSTER-SYNCHROTRON VOM BESSY II," Bachelor's Thesis, Humboldt-Universität zu
Berlin, 2013.

[27] T. Kamps, P. Kuske, and D. Lipka, "BEAM MEASUREMENTS AND MANIPULATION OF
THE ELECTRON BEAM IN THE BESSY-II TRANSFER LINE FOR TOPPING UP
STUDIES," in *Proc. of European Particle Accelerator Conference (EPAC'06), Edinburgh,
Scotland, June 26-30, 2006*, ser. European Particle Accelerator Conference, no. 10,
Helmholtz-Zentrum Berlin fur Materialien und Energie GmbH (HZB). Geneva, Switzerland:
JACoW, 2006, paper TUPCH009, pp. 1010–1012. [Online]. Available:
https://accelconf.web.cern.ch/AccelConf/e06/PAPERS/TUPCH009.PDF

[28] M. Aiba, M. Böge, J. Chrin, N. Milas, T. Schilcher, and A. Streun, "COMPARISON OF
LINEAR OPTICS MEASUREMENT AND CORRECTION METHODS AT THE SWISS
LIGHT SOURCE," *Physical Review Special Topics-Accelerators and Beams*, vol. 16, no. 1, p.
012802, 2013.

[29] "MAGNET FIELD MEASUREMENT REPORT (order no. 6266)," DANFYSIK.

[30] Daniel F. Förster, Bernd Lindenau, Marko Leyendecker, Franz Janssen, Carsten Winkler, Frank
O. Schumann, Jürgen Kirschner, Karsten Holldack, and Alexander Föhlisch, "PHASE-LOCKED
MHz PULSE SELECTOR FOR X-RAY SOURCES," *Optics letters*, vol. 40, no. 10, pp.
2265–2268, 2015.

[31] K. Holldack, T. Kachel, S. Kahn, R. Mitzner, and T. Quast, "CHARACTERIZATION OF
LASER-ELECTRON INTERACTION AT THE BESSY II FEMTOSLICING SOURCE,"
Physical Review Special Topics-Accelerators and Beams, vol. 8, no. 4, p. 040704, 2005.

[32] K. Holldack, R. Ovsyannikov, P. Kuske, R. Müller, A. Schälicke, M. Scheer, M. Gorgoi, D.
Kühn, T. Leitner, S. Svensson, N. Martensson, and A. Föhlisch, "SINGLE BUNCH X-RAY
PULSES ON DEMAND FROM A MULTI-BUNCH SYNCHROTRON RADIATION
SOURCE," *Nature communications*, vol. 5, 2014.

[33] P. Goslawski, P. Kuske, R. Müller, M. Ries, M. Ruprecht, A. Schälicke, G. Wüstefeld, W.
Anders, A. Burrill, J. Knobloch, A. Neumann, A. Velez, V. Dürr, D. Pflückhahn, O. Schüler, A.
Föhlisch, K. Holldack, K. Ott, A. Jankowiak, J. Knobloch, and N. Neumann, "TECHNICAL
DESIGN STUDY - BESSY VSR," Helmholtz-Zentrum Berlin fur Materialien und Energie
GmbH (HZB), 2015.

[34] P. Goslawski, M. Ries, M. Ruprecht, and G. Wüstefeld, "THE LOW-α LATTICE AND BUNCH
LENGTH LIMITS AT BESSY-VSR," in *Proc. of European Particle Accelerator Conference
(EPAC'98), Dresden, Germany, June 15-20, 2014*, ser. International Particle Accelerator
Conference, no. 5. Geneva, Switzerland: JACoW, 2014, paper MOPRO058, pp. 216–218.
[Online]. Available: http://accelconf.web.cern.ch/accelconf/IPAC2014/papers/mopro058.pdf

[35] "Datasheet: TM-9701," PULNIX.

[36] "DEVICE PERFORMANCE SPECIFICATION - KODAK KAI-0373 IMAGE SENSOR,"
     KODAK.

[37] P. Strehl, *Beam Instrumentation and Diagnostics*, 3rd ed.   Berlin, Heidelberg: Springer, 2006.

[38] S. Wesch, "Elog entry 16.01.2013: Erste Emittanzmessung meinerseits vor und hinter dem ersten
     'double bend' in der LINAC injection line LI," Helmholtz-Zentrum Berlin fur Materialien und
     Energie GmbH (HZB), 2013.

[39] I. The MathWorks, "MATLAB 8.4.0.150421 (R2014b) ©2015 The MathWorks, Inc. MATLAB
     and Simulink are registered trademarks of The MathWorks, Inc. See
     www.mathworks.com/trademarks for a list of additional trademarks. Other product or brand
     names may be trademarks or registered trademarks of their respective holders." 2014.

[40] D. Krämer, "Elog entry 16.01.2013: Erste Emittanzmessung meinerseits vor und hinter dem
     ersten 'double bend' in der LINAC injection line LI," BESSY II, 2000.

[41] J. B. Murphy, "SYNCHROTRON LIGHT SOURCE DATA BOOK," NSLS, 1989.

[42] Alex Forencich, "Python VXI-11," 2013. [Online]. Available:
     https://github.com/python-ivi/python-vxi11

[43] Volz, Paul, "LINEAR OPTICS SURVEY OF THE BESSY II BOOSTER SYNCHROTRON
     TOWARDS A LOW-α LATTICE," Bachelor's Thesis, Humboldt-Universität zu Berlin, 2016.

[44] P. Kuske, "Private communication," Helmholtz-Zentrum Berlin fur Materialien und Energie
     GmbH (HZB), 2016.

[45] P. Kuske and F. Kramer, "TRANSVERSE EMITTANCE EXCHANGE FOR IMPROVED
     INJECTION EFFICIENCY," in *Proc. of International Particle Accelerator Conference
     (IPAC'16), Busan, Korea, May 8-13, 2016*, ser. International Particle Accelerator Conference,
     no. 7.   Geneva, Switzerland: JACoW, June 2016, paper WEOAA01, pp. 2028–2031,
     doi:10.18429/JACoW-IPAC2016-WEOAA01. [Online]. Available:
     http://jacow.org/ipac2016/papers/weoaa01.pdf

[46] M. Borland, "elegant: A Flexible SDDS-Compliant Code for Accelerator Simulation," september
     2013.

[47] Hans Grote, Frank Schmidt, and Laurent Deniau, "MAD-X 5.02.00 (64 bit, Linux) - Methodical
     Accelerator Design program, CERN," http://cern.ch/madx/, Code Modification Date:
     2014.03.05.